8-2016

Optical dosimetry tools and Monte Carlo based methods for applications in image guided optical therapy in the brain

Akshay N Prabhu Verleker
Purdue University

PURDUE UNIVERSITY
GRADUATE SCHOOL
Thesis/Dissertation Acceptance

This is to certify that the thesis/dissertation prepared

By Akshay N Prabhu Verleker

Entitled
OPTICAL DOSIMETRY TOOLS AND MONTE CARLO BASED METHODS FOR APPLICATIONS IN IMAGE GUIDED OPTICAL THERAPY IN THE BRAIN

For the degree of Doctor of Philosophy

Is approved by the final examining committee:

Dr. Keith Stantz   Dr. David Hofeldt
Chair

Dr. Shuang Liu

Dr. Ulrike Dydak

Dr. James Schweitzer

To the best of my knowledge and as understood by the student in the Thesis/Dissertation
Agreement, Publication Delay, and Certification Disclaimer (Graduate School Form 32),
this thesis/dissertation adheres to the provisions of Purdue University's "Policy of
Integrity in Research" and the use of copyright material.

Approved by Major Professor(s): Dr. Keith Stantz

Approved by: Dr. Shuang Liu   6/21/2016
        Head of the Departmental Graduate Program   Date

OPTICAL DOSIMETRY TOOLS AND MONTE CARLO BASED METHODS FOR APPLICATIONS

IN IMAGE GUIDED OPTICAL THERAPY IN THE BRAIN

A Dissertation

Submitted to the Faculty

of

Purdue University

by

Akshay N Prabhu Verleker

In Partial Fulfillment of the

Requirements for the Degree

of

Doctor of Philosophy

August 2016

Purdue University

West Lafayette, Indiana

Dedicated to my grandfather whose "Science Bug" bit me early in life.

ACKNOWLEDGEMENTS

It would not have been possible to come this far without the love and support (emotional and technical) from my parents Dr. Narayan and Dr. Shitala Prabhu Verleker, my wife and better-half Shweta, my sister Sayali and brother Ashwin.

TABLE OF CONTENTS

LIST OF TABLES

LIST OF FIGURES

LIST OF ABBREVIATIONS

NIR   Near Infra-red

MCX   Monte Carlo Extreme (GPU based Monte Carlo by Fang group)

MC   Monte Carlo

GPU   Graphical Processor Unit

FWHM   Full Width at Half Maximum

FWTM   Full Width at Tenth Maximum

OPO   Optical Parametric Oscillator

ROI   Region of Interest

TiO_2 Titanium Dioxide

RMS   Root Mean Square

CT   Computed Tomography

MRI   Magnetic Resonance Imaging

OPO   Optical Parametric Oscillator

ABSTRACT

Prabhu Verleker, Akshay N. Ph.D., Purdue University, August 2016. A Therapeutic Protocol for Treatment of Brain Metastasis through Optically Stimulated Drug Release. Major Professor: Keith Stantz.

Purpose: The long-term goal of this research is to determine the feasibility of using near infra-red light to stimulate drug release in metastatic lesions within the brain. In this work, we focused on developing the tools needed to quantify and verify photon fluence distribution in biological tissue. To accomplish this task, an optical dosimetry probe and Monte Carlo based simulation code were fabricated, calibrated and developed to predict light transport in heterogeneous tissue phantoms of the skull and brain. Empirical model (EM) of photon transport using CT images as input were devised to provide *real-time* calculations capable of being translated to preclinical and clinical applications.

Methods and Materials: A GPU based 3D Monte Carlo code was customized to simulate the photon transport within head phantoms consisting of skull bone, white and gray matter with differing laser beam properties, including flat, Gaussian, and super-Gaussian profiles that are converging, parallel, or diverging. From these simulations, the local photon fluence and tissue dosimetric distribution was simulated and validated

through the implementation of a novel titanium-based optical dosimetry probe with an isotropic acceptance and 1.5mm diameter. Empirical models (EM) of photon transport were devised and calibrated to MC simulated data to provide 3D fluence and optical dosimetric maps in *real-time* developed around on a voxel-based convolution technique Optical transmission studies were performed using human skull bone samples to determine the optical transmission characteristics of heterogeneous bone structures and the effectiveness of the Monte Carlo in simulating this heterogeneity. These tools provide the capability to develop and optimize treatment plans for optimal release of pharmaceuticals to metastatic breast cancer in the brain.

Results: At the time of these experiments, the voxel-based CUDA MC code implemented and further developed in this study had not been validated by measurement. A novel optical dosimetry probe was fabricated and calibrated to measure the absolute photon fluence (mW/mm^2) in phantoms resembling white matter, gray matter and skull bone and compared to 3D Monte Carlo simulated data. The TiO_2-based dosimetry probe was shown to have superior linearity and isotropicity of response to previous Nylon based probes, and was better suited to validate the Monte Carlo using localized 3D measurement (< 25% systematic error for white matter, gray matter and skull bone phantoms along illumination beam axis up to a depth of 2cm in homogeneous tissue and 3.8cm in heterogeneous head phantom). Next, the transport parameters of the empirical algorithm was calibrated using the 3D Monte Carlo and EMs and validated by

optical dosimetry probe measurements (with error of 10.1% for White Matter, 45.1% for Gray Matter and 22.1% for Skull Bone phantoms) along illumination beam axis.

Conclusions: The design and validation of the Monte Carlo, the optical dosimetry probe and the Empirical algorithm increases the clinical feasibility of optical therapeutic planning to narrow down the complex possibilities of illumination conditions, further compounded by the heterogeneous structure of the brain, such as varying skull thicknesses and densities. Our ultimate goal is to design a fast Monte Carlo based optical therapeutic protocol to treat brain metastasis. The voxelated nature of the MC and EM provides the necessary 3D photon distribution to within 25% error to guide future clinical studies involving optically triggered drug release.

1   INTRODUCTION

1.1   Overview

The purpose of our research involves the development of optical dosimetry and simulation tools to quantify and optimize the delivery of light to brain tissues. We start by introducing the concept of optically stimulated drug release for treatment of cancerous lesions in the brain. This mode of therapy requires an efficient optical planning system to determine the best modes of illumination to target tissues in the brain. Such a planning system applies the physics of optical transport to determine the photon distribution in complex heterogeneous media characterized by clinical imaging methods, such as CT and MRI. Critical is the need to validate these methods in tissue phantoms and to determine their accuracy and precision. To realize these ideas into planning systems, which require multiple sources and optimization algorithms, require fast execution times not afforded by MC codes. An Empirical algorithm can achieve these fast simulation speeds. Ultimately, these simulation tools are validated in tissue phantoms using a novel optical dosimetry probe with a Titanium Dioxide with a linear and isotropic response.

1.2   Application in Optically Stimulated Drug Release

To date, brain cancer remains a sanctuary for metastasis. Treatment of Central Nervous System (CNS) metastasis poses a critical clinical challenge due to limitations in drug uptake in the brain (across the blood brain barrier and blood-cerebrospinal fluid barrier) and adverse neurotoxic effects of mainstay therapies, such as whole brain radiation therapy (WBRT) and stereotactic radiosurgery [1-8]. Recently, receptor targeted therapy aided by improved imaging and localized radiotherapy has shown promise in treating cancer within the brain. This is particularly true for HER2+ breast cancer metastasis, which have poor median survival rates of 2 to 16 months [1-7]. Therefore, Dr. Susan Clare, a Surgeon at Northwestern University Robert H Lurie Medical Research Center, devised a method where a patient's macrophages and monocytes are loaded with a drug payload, in this case a lapatinib laden nanoparticle, to actively delivery and target the metastatic cancer cells. The 'Trojan Horse' concept has shown significant promise in targeted drug delivery to the brain, with metastatic cells retaining their sensitivity to the drug even after its administration [8, 9]. The use of macrophages as drug carriers has been proved to be a potentially effective tool because macrophages have been seen to comprise up to 70% of volume in cancerous tumors, such as breast cancer [10-13]. The quantification of macrophages in different tumor types can be done using mouse monoclonal antibody EBM/11 [14, 15], and is an important process in determining the therapeutic accuracy of this potential treatment.

This idea was demonstrated by replacing labeling the payload with fluorescent molecules and showing uptake and fluorescence in brain metastasis of mice, which was published in Cancer Nanotechnology [8, 9]. The long-term goal of this study is to deliver lapatinib-gold nanocomplex laden macrophages to brain metastasis and design a therapeutic protocol to optically stimulate drug release in target tissues in the brain. With the rate and quantity of drug release being directly dependent on the optical power delivered, an optical simulation protocol using Monte Carlo simulations can be designed to effectively predict the photon distribution and subsequent drug activation in the brain tissue.
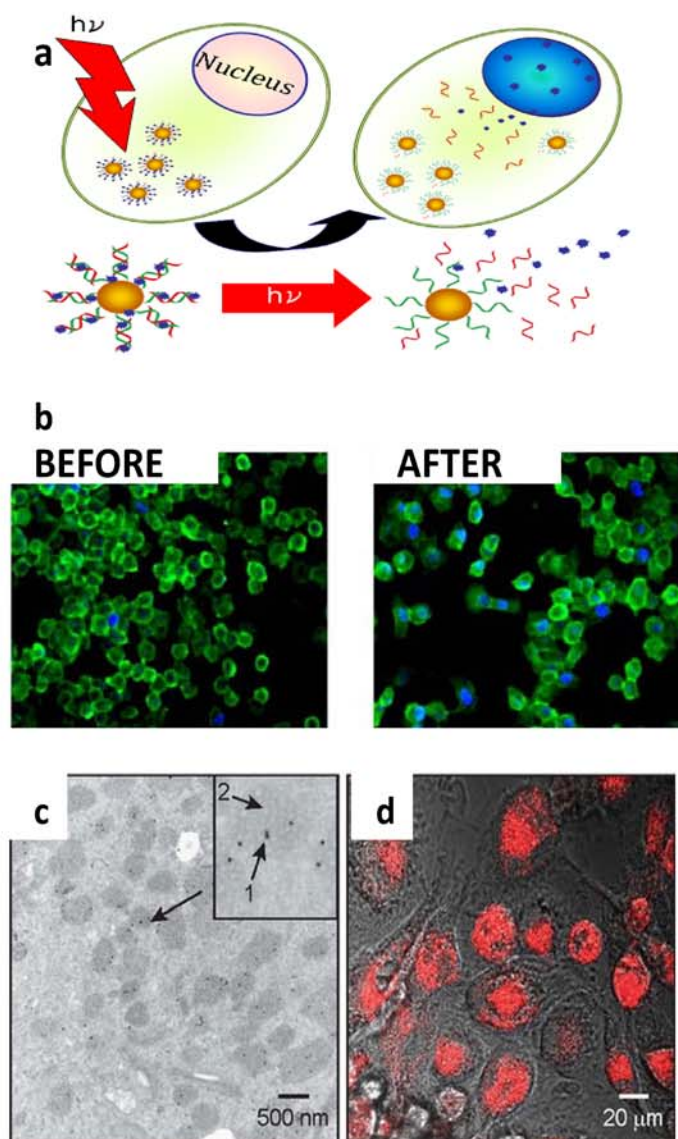
Figure 1.1 (a) Light-induced release of DAPI (4',6-diamidino-2-phenylindole) within H1299 lung cancer cells. (b) Left: H1299 lung cancer cells containing DAPI prior to illumination and on the right: after NIR exposure. (Input fluence: 1 W/cm^2, NIR wavelength: 800 nm, 5 minute exposure duration). No major cytotoxity was observed in assay studies post illumination. (c) Macrophages incubated with gold-silica-nanoshells-red fluorescent microspheres complexes [8, 9]. Intra-cellular accumulation f these fluorescent molecules is seen in the transmission electron micrograph within the cytoplasm vacuoles (see arrow 2). (c) Images using fluorescence microscopy indicate microsphere accumulation through red fluorescence (580/605 nm) [8, 9].

1.3 Applications Requiring Quantification of NIR Light Delivery

While the primary purpose of this research was to enable the quantification of photon

propagation in heterogeneous brain tissues, it can be easily applied to NIR based

imaging techniques such as Photoacoustic Tomography (PCT), Near Infra-Red

Spectroscopy (NIRS) and in optical stimulation of neurons in the brain. The use of the

Monte Carlo and the optical dosimetry probe in absolute quantification of photon

fluence in tissues can provide the necessary corrections and validation to quantify

molecular concentrations in vivo and to deliver the necessary photon dose to trigger

therapeutic effects.

Photoacoustic effect involves the absorption of light energy by a molecule, which leads

to a thermal heating and volumetric expansion. The generated acoustic wave usually in

the ultrasound frequency range is proportional to the optical energy absorbed or dose,

and thus a molecule's concentration such as hemoglobin and injectable dyes. This has

led to both clinical and pre-clinical applications such as breast cancer imaging, small

animal studies, hemoglobin concentration, oxygen saturation, blood perfusion imaging

etc. [16-20]. The application of optical Monte Carlo based methods in Photoacoustic

imaging has shown promising results in improving the estimation of photon propagation

in complex tissues being imaged [21-26].

Another imaging modality which widely used the penetrating ability of NIR light in

tissues, particularly in the brain, is NIR Spectroscopy. The NIR Spectroscopy uses a

source and a detector placed on the surface of the brain. The light gets transmitted

through the skull and after undergoing multiple absorption, scattering and refraction

events, gets measured by another detector placed on the skull surface near the source.

The changes in blood oxygenation in the brain leads to changes in light absorption and

can be monitored through the signal detected at various stages of brain activation,

initially reported by Jobsis in 1977 [27]. It uses a modified Beer-Lambert's law for high

scattering brain tissues [28, 29]. This technique was initially used to map brain function

of cortical tissues in animal and human subjects [30, 31], and later in brain functions of

intact skulls in human adults [32-36]. Various applications include monitoring

intracellular physiological processes in the brain cells and in measuring Cerebral Blood

Flow (CBF) and Cerebral Blood Volume (CBV) [37-40]. Hence the use of Monte Carlo

estimation methods for complex 3D photon propagation along with the optical

dosimetry methods can improve the accuracy of the fNRIS measurements by providing

absolute quantification of photon fluence.

NIR neural stimulation is another method which requires knowledge of the optical dose

in the brain. The use of pulsed infra-red lasers has been shown to trigger the excitation

of neurons at a certain optical threshold [41]. This effect has been observed to be

wavelength dependent and is seen by measuring the compound action potential (CAP)

linked to Ca^{+2} ions in neural mitochondria [41]. Various studies in tissues samples and

in-vivo have been carried out to monitor this effect and measure the electrical activity

of the brain [42-49]. The use of Monte Carlo methods with wavelength dependent

absorption simulation techniques can provide the necessary information to correlate the electrical activity in brain tissue, such as the cochlea and neuro-prosthesis.

1.4   Light Transport Theory

The radiative transport equation describes the propagation of light through media and is considered to be more accurate as it takes into account the absorption and scattering of light in heterogeneous media [50, 51].

$$s.\nabla L(r, s) = -(\mu_a + \mu_s)L(r, s) + \mu_s \int_{4\pi} p(s, s')L(r, s')d\omega', \quad (1.1)$$

where L(r,s) is the radiance (units: $W.m^{-2}.sr^{-1}$) at position **r**, in the direction **s** (unit vector) in a medium with an absorption coefficient of μ_a and scattering coefficient of μ_s. Radiance itself is defined as the radiant flux (Watts/sec) emitted, transmitted or received by a surface per unit solid angle, per unit projected area [50, 51]. The total attenuation coefficient (μ_t) is the sum of the absorption (μ_a) and scattering (μ_s) coefficients (units: m^{-1}). Equation 1.6 describes the change in radiance due to absorption and scattering out of or into a volume. The differential solid angle $d\omega'$ is in the direction of s' and p(s,s') refers to the phase function, which is the probability of a photon travelling in direction s' being scattered into direction s. or characterized by the parameter g (anisotropy factor), the cosine average of the phase function:

$$g = \int_{4\pi} p(s, s')(s.s')d\omega'. \quad (1.2)$$

The value of the parameter g describes the scattering, for example forward scatter means g=1, isotropic scatter by g=0 and backscatter by g=-1.

The radiative transport theory assumes a homogeneous distribution of the scattering

and absorbing particles in the medium. This assumption and the quantification of the

scattering and absorption coefficients can help predict the fluence distribution and the

absorbed energy in the medium. There are several approximations to solving the

transport equation depending on the type of irradiance (e.g. diffuse or collimated) and

optical boundary conditions [50, 51]. For depths far from the light source, there are two

solutions which account for un-scattered transmission and an asymptotic fluence-rate:

the Beer Lambert's law and the Diffusion approximation. The Beer Lambert's law

describes the transmission of light through a non-scattering medium:

$$T = e^{-\mu_t}, \quad (1.3)$$

where t is the thickness or path-length, T is the fraction of the intensity transmitted

through the medium and μ_t is the total attenuation coefficient.

A further modification of the Beer's Law is made to account for two scattered

components [51]:

$$L(r, s) = L_c(r, s) + L_d(r, s), \quad (1.4)$$

where L_c is the light that did not interaction with tissue while L_d is the part that

underwent scattering. Thus using this diffuse theory approximation in the RTE equation,

the fluence can be simplified to [51]:

$$\varphi(r) = \int_{4\pi} L_d(r, s) d\omega. \quad (1.5)$$

The diffuse approximation is affected by the ratio of scattering-to-absorption

coefficients, the tissue distance from the light source, the boundaries and the

anisotropy factor [52]. A phase function compatible with the diffusion equation is the

Henyey-Greenstein function (p_{HG}) [53, 54]:

$$p_{HG}(s, s') = (\frac{1}{4\pi}) \sum_{n=0}^{\infty}(2n + 1)g^n P_n(s, s'), \quad (1.6)$$

where P_n are the Legendre polynomials. The phase function given by the delta-

Eddington approximation, combines both the diffusion and forward scatter terms, and is

given by [55]:

$$p(s, s') = f\delta(s - s') + (1 - f)p_1(s, s'), \quad (1.7)$$

where f is the forward scatter amount and p_1 are the first two terms of the Legendre

polynomial. The delta-Eddington phase function makes use of the Henyey-Greenstein

phase function and is found to be ideal for light propagation in tissues. This is done by

the following substitutions [53, 55]:

$$\frac{g_{HG}}{1+g_{HG}} = g \quad (1.8)$$

$$\mu_s(1 - g_{HG}^2) = \mu_s^1 \quad (1.9)$$

Thus, the total fluence rate in a material of finite depth is [56]

$$\varphi(z) = a_1 \exp(kz) + a_2 \exp(-kz) + a_3\exp(-\mu_t z), \quad (1.10)$$

where z is the depth and k is approximately equal to μ_{eff}. This condition is valid only if

the absorption coefficient is significantly lower than the scattering coefficient. As per

the diffusion theory, the transmittance T and reflectance R are given by [57 - 60]:

$$T = \frac{\mu_s g e^{-\mu_t t}}{\mu_a + (1-g)\mu_s} - (a_1 k e^{kt} - a_2 k e^{kt} - a_3 \mu_t e^{-\mu_t t}) \quad (1.11)$$

and

$$R = -\frac{\mu_s g}{\mu_a + (1-g)\mu_s} + h/2(a_1 k - a_2 k - a_3 k). \quad (1.12)$$

The optical properties (scattering coefficient (μ_s), absorption coefficient (μ_a), anisotropy factor (g)) can be calculated using the total reflectance and transmission. The reduced scattering coefficient (μ_s') is related to the scattering coefficient (μ_s) as follows [61, 62]:

$$\mu_s^1 = (1 - g)\mu_s \quad (1.13)$$

For complex heterogeneous tissues, the relation between reflectance, transmission and the three optical parameters become complicated. A unique computation method used to simulate the random walk of photons across complex heterogeneous media is the Monte Carlo based on μ_s, μ_a, g, n, and p(s,s')

1.5   A GPU based 3D Monte Carlo for photon transport

The Monte Carlo model uses a random number generator to simulate the transport of photons in optical media [57-60] based on the absorption coefficient (μ_a), scattering coefficient (μ_s), anisotropy factor (g) and the index of refraction (n). A 3D voxel based Monte Carlo allows simulation of complex geometrical boundaries, with each voxel having unique optical properties (μ_a, μ_s, g, n) [59] A packet of photons is assigned an initial weight and direction, and propagate from one voxel to another, while depositing

energy in each voxel based on its absorption coefficient. The photons also scatter within voxels after travelling a pre-determined distance based on the scattering coefficient of the medium. The new direction of the scattered photon is determined by the anisotropy factor (g) which is the cosine of the phase function [57]. Finally, when the weight of the photon reaches a pre-determined threshold, it is extinguished. The weights deposited by all the photons in each voxel are accumulated to determine the energy deposited, while the total number of photons passing through the voxel is its fluence rate (photons/mm^2.s) [61].

Traditional CPU based Monte Carlo models [57, 59] suffer from slow computation speeds, which makes them non-viable for application in clinical settings, especially in highly scattering tissues, such as white matter. The GPU based 3D Monte Carlo code used in these studies was shown to be 300X faster compared to our previous CPU based models [61]. The CUDA acceleration provided by this model helps to achieve complete brain simulation of a high fluence broad beam source within hours, as compared to days of simulation time using CPU based models [61 - 63]. This model also provides a voxel based 3D distribution of photon fluence and energy deposited, and can be coregistered with different medical imaging modalities (e.g. CT, MR, Ultrasound, etc.), thus improving its clinical viability for diagnosis and therapy [62, 63].

1.6   An Empirical Photon Propagation Algorithm

While Monte Carlo is the gold standard for photon propagation, it has long execution

times even with the acceleration provided by the GPU based models. For high scattering

tissues, such as white matter and skull bone, the simulation time for a broad beam

simulation is on the order of several hours (based on beam diameter) in order to

achieve statistically significant results at depths of more than 2cm [63, 64]. Thus for

applications involving optical illumination planning for therapy, where multiple

simulations are required for optimizing light delivery to tissues at 5-8cm in depth with

complex geometry and heterogeneity, a fast alternate approach is required, particularly

for protocols requiring multiple beams [63]. We therefore designed an algorithm based

on an empirical model (EM) that simulates photon propagation in heterogeneous

voxelated optical media [63, 64].

The EM algorithm implements a convolution technique where the photon fluence within

a voxel is the sum of the weighted fluence in neighboring voxels. It simulates photon

scatter by assigning weights for forward, diagonal, side and back scatter directions [64].

The fluence within a voxel is assumed to be made of directional components in the x, y,

and z directions to emulate the Henyey-Greenstein function. The fluence entering a

voxel is redistributed into these directional components such that the sum of the

weights is conserved prior to absorption. The scatter weights are determined by

comparing the photon fluence distribution with the Monte Carlo under similar

illumination and boundary conditions, before being applied to complex heterogeneous media [64].

The Empirical algorithm provides a fast approach to simulate complete 3D simulations at a fraction of the time (seconds) compared to the Monte Carlo (hours) in complex 3D media (e.g. brain) [63, 64]. This allows us to evaluate multiple illumination conditions for an optical therapeutic protocol for optimized light delivery to tissues within clinically relevant time frames. The 3D voxel based empirical approach also allows for easy integration of the simulated photon energy dose maps with existing imaging modalities, e.g., CT, MR, Ultrasound, Photoacoustic Computed Tomography, which improves therapeutic planning accuracy [63]. Thus the empirical approach can be used a preliminary tool to narrow down the possible illumination conditions, while the Monte Carlo can be used to finalize and quantify the estimated fluence for optical therapy. This makes the use of optical simulation techniques more attractive in clinical settings by reducing the simulation times involved, and is a core purpose of our research.

1.7   A Titanium Dioxide based Optical Dosimetry Probe

Optical dosimetry involves measuring the localized photon fluence in media such as tissues or tissue phantoms. An optical dosimetry probe is a device which consists of a bulb of highly scattering material attached to the exposed tip of an optical fiber, with the other end of the fiber is connected to a photodiode circuit which is in turn connected to an oscilloscope. The light is conducted by the optical fiber to the PIN

photodiode where it is converted into an electrical signal. The dosimetry probe is preferred over calorimeters due to the smaller size, higher sensitivity, and isotropic response of the probe in an aqueous (or liquid) media. In this study, we fabricated an optical dosimetry probe with better isotropicity and locality compared to previous designs of Nylon based probes. The dosimetry probe was used to validate the fluence generated by the Monte Carlo simulation in homogeneous and heterogeneous brain-tissue phantoms. The optical sensitivity of the probe enabled us to validate extremely low fluence in tissue phantoms, unlike the calorimeter.

2   SPECIFIC AIMS

In Chapter 1, quantifying the photon fluence within a heterogeneous tissue is important for applications including controlled drug release, neuro-stimulation and therapy, and molecular imaging. In each of these applications, quantification of the photon fluence and optical dosimetry is critical. Thus, the focus of this research is on the development of image-based simulation tools to predict 3D photon distributions within optically heterogeneous media and in the advancement of instrumentation to validate these techniques. To accomplish these tasks, we propose to:

SA1: *Develop, build and test an optical dosimetry probe and advance 3D Monte Carlo photon transport code capable of measuring and simulating the local photon fluence and dose in optical tissue phantoms;*

SA2: *Simulate and validate the absolute photon fluence in homogeneous and heterogeneous brain tissue phantoms resembling white matter, gray matter, skull bone and tumor;*

SA3: *Devise an empirical model and algorithms capable of simulating for photon propagation in complex heterogeneous tissues in real-time; and*

SA4: *Investigate the feasibility of using the above tools and methods to optimize optical therapeutic protocols n human skull bones using image-guided techniques.*

2.1   Specific Aim1: Develop, build and test an optical dosimetry probe and advance 3D Monte Carlo photon transport code capable of measuring and simulating the local photon fluence and dose in optical tissue phantoms

The rate and quantity of drug release depends on the optical fluence or laser energy delivered to the tissues. To measure the photon fluence being delivered, we have designed and calibrated an optical dosimetry probe to measure the localized ($1mm^3$) photon fluence in tissues with complex optical heterogeneities at depths in brain tissue phantoms consistent with preclinical and clinical applications. Next, CUDA based 3D Monte Carlo code was further developed to predictor of light fluence/energy distribution in tissues. This software has been developed as an open source project by the Dr. Fang's group at Harvard. We have further modified this software package to model and simulate 3D photon beams with Gaussian and super-Gaussian distributions consistent with the laser beam in our laboratory, along with modifications to increase the computation speed.

2.2   Specific Aim2: Simulate and validate the absolute photon fluence in homogenous

and heterogeneous brain tissue phantoms resembling white matter, gray matter,

skull bone and tumor.

In order to be used as a therapy planning tool, the 3D Monte Carlo needs to be validated

in optical phantoms resembling white matter, gray matter and skull bone. The CUDA

based MC code was used to generate 3D photon fluence and energy absorption (or

dosimetry) maps generated and validated by optical dosimetry probe measurements in

homogeneous and heterogeneous brain tissue phantoms. Since the quantity and energy

threshold of drug released depends on the optical energy coupled to the tissues, the

cross validation of the dosimetry and simulation tools is a major step in ensuring

planning accuracy in clinical setting.

2.3   Specific Aim3: Devise an empirical model and algorithms capable of simulating for

photon propagation in complex heterogeneous tissues in real-time

Empirical models of photon transport provide an *estimate* of the local photon fluence in

heterogeneous tissues with fast execution times for the optimization of clinical

applications not afforded by Monte Carlo methods. The GPU based Monte Carlo

requires many hours of execution time to simulate photon distribution within a human

brain, which can be a disadvantage when optimizing a treatment plan iterating over

multiple illumination conditions. A weights-based empirical model approach to photon

propagation is investigated. It simulates photon scatter by using weights for directional

scatter of photons between neighboring voxels, and absorption using the Beer-

Lambert's law. These weights are determined using the Monte Carlo. The objective is to achieve execution times on the order of seconds. Thus the empirical approach provides an alternative means of evaluating multiple illumination conditions to reduce treatment planning time before using the Monte Carlo for final validation of photon fluence and provide real-time imaging corrections.

2.4   Specific Aim4: Investigate the feasibility of using the above tools and methods to optimize optical therapeutic protocols in human skull bones using image-guided techniques

While dosimetry and simulation studies using optical phantoms helps us measure of the photon distribution in brain tissues under ideal conditions, it does not take into account the heterogeneous composition of the skull bone and the bone-tissue interface, which affects the optical transmission and distribution of photon fluence within the soft tissues.   Computed Tomographic images will be acquired to map the density and composition of the bone along with the boundary conditions and to correlate and predict the transmission of NIR light through the skull. Experiments will be performed on human skull bone samples by mapping out the photon fluence transmitted through the bone using the dosimetry probe and comparing it to the Monte Carlo simulated photon distribution. Previous studies have indicated a wide variance in the optical properties of the human skull bone, which can be accounted for by the Monte Carlo code and optical dosimetry probe measurements developed in this research. Thus, the best set of properties for the skull bone for each individual patient can be planned.

3   SPECIFIC AIM1: OPTICAL SIMULATION AND DOSIMETRY TOOLS

3.1   Introduction

In order to estimate the amount of drug released in tissues, we need to be able to

derive the number of photons travelling in each voxel (also known as the "fluence",

photons/mm^2) and the photon energy absorbed per unit volume (mJ/mm^3). The photon

fluence maps can be converted into their corresponding drug release maps by using a

threshold determined by in vitro studies. We modified a GPU based 3D Monte Carlo

(MC) to determine the photon fluence in tissues using different illumination beam

profiles. The validation of the MC software in tissue phantoms requires localized

measurements of photon fluence in tissue phantoms implementing an optical dosimetry

probe with isotropic acceptance. In this chapter, we describe the design, fabrication and

calibration of the probe and the validation of the Monte Carlo through its use.

3.1.1   Monte Carlo Algorithm

The Monte Carlo method generates a random number between 0 and 1 with a normal

distribution [57] to determine the step size and photon scatter direction based on the

optical properties of the medium [57, 59, 61, 64, 65].
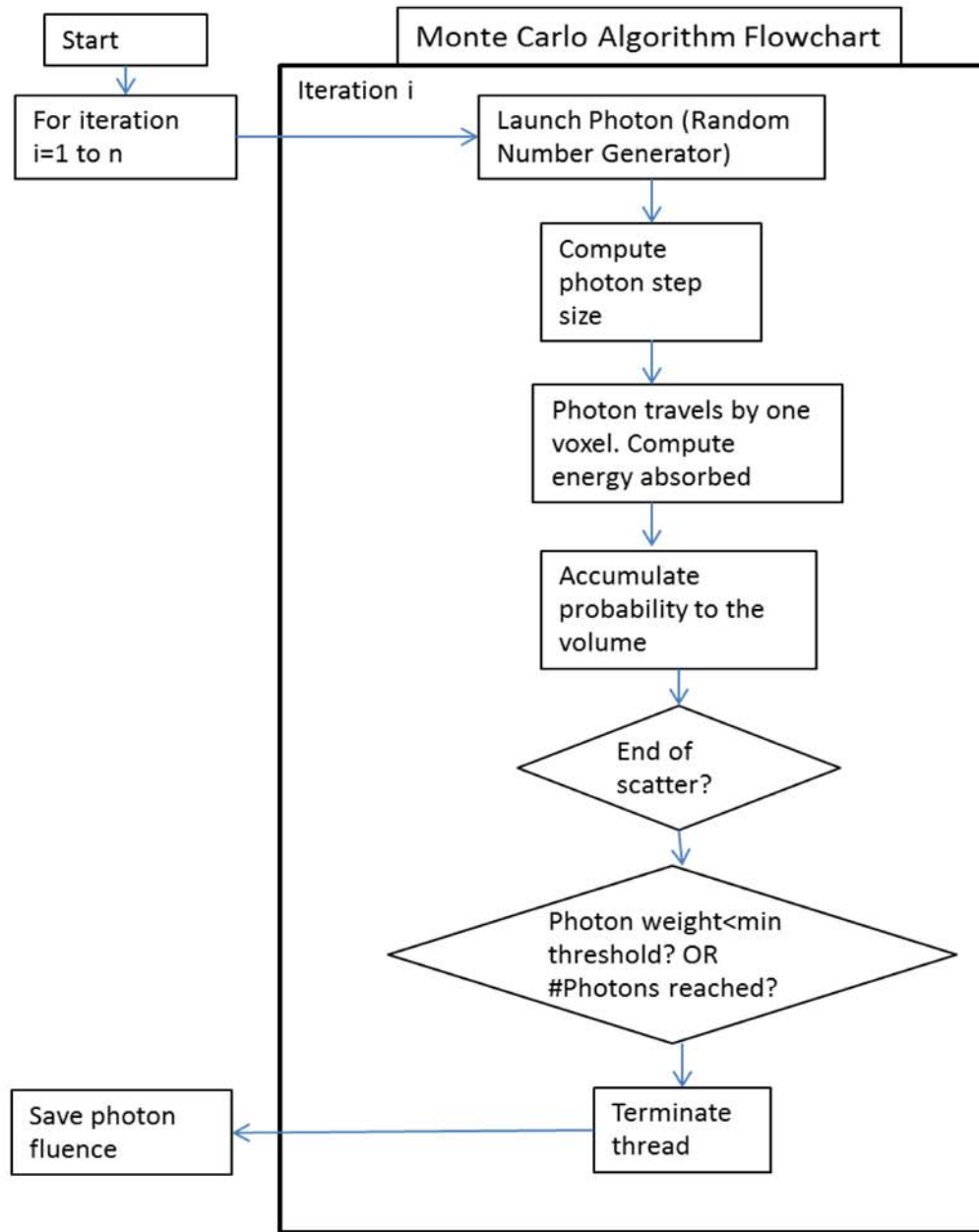
Figure 3.1 Flowchart of the Monte Carlo algorithm for photon propagation [61]

The fluence $F(\bar{r}, t)$ ($mm^{-2}s^{-1}$ or $J.mm^{-2}s^{-1}$) in a voxel depends on the raw probability of photon accumulation in a voxel while preserving energy conservation [58]:

$$F(\bar{r}, t) = \frac{P(\bar{r},t)E_a/E_t}{\sum_i \sum_j P(\bar{r_i},t_j)\mu_a(\bar{r_i})\Delta V \Delta t} \quad (3.1)$$

where the raw probability is $P(\bar{r}, t)$ at a position defined by **r** and at time t. E_a/E_t is the

ratio of energy absorbed to the total energy in the time interval ("time gate") of Δt and

μ_a is the absorption coefficient (mm^{-1}) [61]. The random number ε generated between 0

and 1 determines the step size or propagation distance of the photon packet between

interactions, S1, coefficient (μ_t) given by [57, 59]:

$$S1 = -\ln(\varepsilon)/\mu_t \quad (3.2)$$

which depends on the total attenuation:

$$\mu_t = \mu_a + \mu_s \quad (3.3)$$

In the above equation, μ_a is the absorption coefficient (mm^{-1}) and μ_s is the scattering

coefficient (mm^{-1}). The weight of the photon packet is absorbed within a voxel through

which it moves based on the pathlength [57, 59, 61]:

$$\Delta w = w\left(\frac{\mu_a}{\mu_t}\right) \quad (3.4)$$

Here the weight lost by the photon packet (with initial weight w) is Δw and the photon

exiting the voxel now has a weight of w - Δw.

The step size is calculated each time a photon enters a new voxel with different optical

properties. At each interaction site, the new scattering angle (deflection angle) is

computed using the cosine of the scattering angle θ [57] based on the Henyey-

Greenstein scattering function:

$$Cos(\theta) = \frac{1}{2g}\left(1 + g^2 - \left[\frac{1-g^2}{1-g+2g\varepsilon}\right]^2\right) \text{ if } g \neq 0 \quad (3.5)$$

$$Cos(\theta) = 2\varepsilon - 1 \text{ if } g = 0 \quad (3.6)$$

The anisotropy factor g is the cosine of the phase function with values lying in between -1 to 1 [57], where g=1 indicates forward scatter, g=-1 implies back scatter, and g=0 means isotropic scatter. The unit vector directions in the x, y and z axis are as follows [57]:

$$\mu_x' = \frac{Sin\theta(\mu_x\mu_z Cos\psi - \mu_y Sin\psi)}{\sqrt{1-\mu_z^2} + \mu_x Cos\theta} \qquad (3.7)$$

$$\mu_y' = \frac{Sin\theta(\mu_y\mu_z Cos\psi - \mu_x Sin\psi)}{\sqrt{1-\mu_z^2} + \mu_y Cos\theta} \qquad (3.8)$$

$$\mu_z' = \frac{-Sin\theta Cos\psi}{\sqrt{1-\mu_z^2} + \mu_z Cos\theta} \qquad (3.9)$$

Where μ_x, μ_y, μ_z are the initial (pre-scatter) directional vectors in the x, y, z directions, while μ_x', μ_y', μ_z' are the new or post-scatter directional vectors. Also the azimuthal angle ψ (range: 0 to 2π) determines the scattering direction and is given by [57]:

$$\psi = 2\pi\varepsilon \qquad (3.10)$$

The Monte Carlo code takes the anisotropy factor along with the values of the index of refraction, absorption and scattering coefficients as an input from the user to define the optical properties of the medium. The photon energy deposited (or dose) (E_{abs} in photons or Joules) in each voxel is given by the product of the photon fluence ($F(\bar{r}, t)$ in $mm^{-2}s$ or $J\ mm^{-2}s$), the absorption coefficient (μ_a in mm^{-1}), the photon pulse duration (or illumination time) (t_{int} in s) and the volume of the voxel (v_{vol} in mm^3):

$$E_{abs} = F(\bar{r}, t)\ \mu_a t_{int} v_{vol} \qquad (3.11)$$

3.1.2 Optical Dosimetry Probe
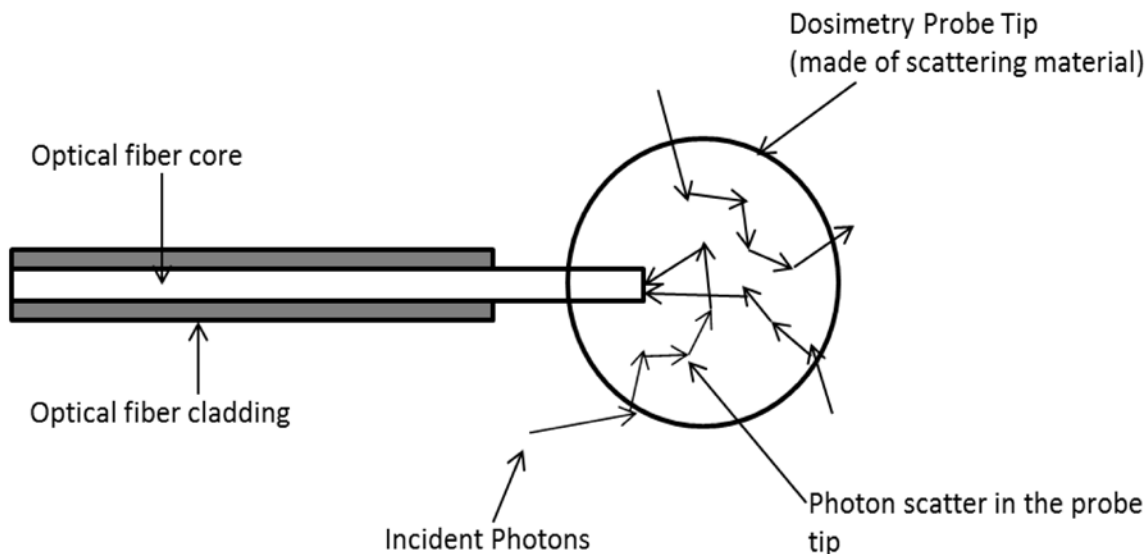
Figure 3.2 Optical dosimetry probe [68].

The optical dosimetry probe consists of an optical fiber, with its exposed end inside a spherical bulb made of a highly scattering material (e.g. Arnite, Nylon or Titanium Dioxide). The other end of the fiber was optically coupled to a PIN photodiode circuit [68, 69]. The light entering the spherical tip causes the light to scatter in all directions so the fraction entering the fiber from any direction is the same. Some of the photons enter the optical fiber tip while others escape back into the surrounding medium. The difference in the refractive index of the TiO_2-epoxy sphere and the surrounding medium determines the number of photons which escape back into the medium, which in turn determines the probe's response or sensitivity [68]. The photons entering the optical fiber are conducted to the PIN photodiode circuit which converts the incident photons into a corresponding voltage signal, which is shown to be proportional to the light

exposed to the TiO2-sphere [63, 68, 69]. This electrical voltage is then read using a

digital oscilloscope and integrated to obtain a quantifiable measure of the optical

fluence [63].

The radiant energy fluence rate at a position "r" is the integral of radiance $L(\mathbf{r}, \hat{s})$ (units

Wsr^{-1}m^2) over all directions (defined by solid angle "Ω") and is given by [68]:

$$\psi(\mathbf{r}) = \int_{4\pi} L(\mathbf{r}, \hat{s}) d\Omega \quad (3.12)$$

where the solid angle about the normal vector $\hat{s}$ is dΩ.

The optimal construction of the dosimetry probe is such that the optical fiber is inserted

a predefined distance within the TiO2 sphere. This prevents a part of the light fluence

within the probe tip from entering the fiber, thus creating a "blind spot" [68]. This

requires a correction factor to be applied to the 4π sr solid angle acceptance of an ideal

dosimetry probe (without a blind spot). The blind spot can be defined in terms of the

solid angle Ω_{blind}. This correction actor F_b in a probe with fiber diameter d and diameter

D of the TiO2 sphere (with "θ"as the arbitrary angles of incidence) is given by [68]:

$$F_b = \frac{\Omega_{sphere}}{\Omega_{sphere} - \Omega_{blind}} = \frac{4\pi}{4\pi - 2\pi \int_0^{\arcsin(\frac{d}{D})} \sin\theta d\theta} = \frac{2}{1 + \cos[\arcsin(\frac{d}{D})]} \quad (3.13)$$

Thus,

$$F_b \approx 1 + \frac{d^2}{4D^2} \quad (3.14)$$

The fluence passing through the fiber is measured by a flat PIN photodiode, whose

response S_{flat} is given by [68]:

$$S_{flat} = \int_{2\pi} L_0 \cos\theta \, d\Omega = 2\pi L_0 \int_0^{\frac{\pi}{2}} \cos\theta \sin\theta \, d\theta = \pi L_0 \quad (3.15)$$

Similarly, for a dosimetry probe, infinitely small, the response to diffuse isotropic

fluence is given as [68]:

$$S_{point} = \int_{2\pi} L_0 d\Omega = 4\pi L_0 \int_0^{\frac{\pi}{2}} \sin\theta \, d\theta = 4\pi L_0 \quad (3.16)$$

Thus in order to obtain the true fluence rate entering the probe, we multiply the

response of the PIN photodiode by a factor of 4, given by [68]:

$$\frac{S_{flat}}{S_{point}} = \frac{\pi L_0}{4\pi L_0} = \frac{1}{4} \quad (3.17)$$

Similar to the blind-spot factor, a correction factor accounting for the difference in the

refractive index of the probe tip and the medium must be applied. The ratio of the

response of the dosimetry probe in liquids (F_n) relative to air has been studied and

measured extensively [68] and depends on the difference in the index of refraction

between the medium and the probe tip. The greater the difference in the refractive

indices causes a higher fraction of photons to be refracted back into the probe, and

higher sensitivity, compared to lower differences, e.g. TiO2-epoxy to air versus water.

The refractive index of the probe (solid) is well above the refractive index of water, thus

measurements in liquids with higher refractive index gives higher probe sensitivity.

Another potential correction factor, Fi, accounts for inhomogeneity in the construction

of the spherical probe tip resulting in an anisotropic response [68]. This factor accounts

for the angular variance in the probe's response to different incidence angles in the

equatorial and azimuthal directions. Excluding the extreme blind spot at oblique angles

(i.e. from the same direction as where the fiber enters the spherical bulb), the angular

variance of a well-constructed probe is generally low [63, 70]. In this study, the angular

response of the dosimetry probes to diffuse incidence fluence was measured to

determine its isotropicity of response. Thus the reading in air must be corrected to

obtain the true fluence rate (ψ_m) using the following equation [68]:

$$\psi_m = \psi_{air} F_n F_b F_i \quad (3.18)$$

3.2   Materials and Methods

3.2.1   Monte Carlo Beam Optimization

The original code of the GPU based 3D Monte Carlo (MC) (by the Fang group [61]) has

several built-in features to simulate photon sources such as Gaussian, flat beams, pencil

beams, isotropic point sources, cone beams, etc. The "open source" availability of this

software and functionality of using random numbers to generate and define photon

sources allows users to modify the original source code to add additional photon beam

profiles as used in different optical setups. The CUDA based parallel threading

functionality also improves the speed of simulation of broad beam sources compared to

the time consuming nature of simulating multiple pencil beams by calling Monte Carlo

function separately for each pencil beam. Even though we had used the process of

generating broad beam profiles, by calling the Monte Carlo serially, in our past studies

[60]; in this study we have optimized the Monte Carlo to generate broad beams by using

the full functionality of the CUDA platform by generating individual pencil beams in parallel.

In this study, we modified the original code to simulate a broad beam super-Gaussian beam profile emanating from an optical fiberguide, coupled to the output of a Laser-OPO system (Nd: YAG class 4 laser and a MagicPRISM Optical Parametric Oscillator from Opotek Inc., Carlsbad, CA). This profile was measured with a calorimeter (gold standard) (Ophir-Spiricon 3A-P-V1) with aperture 12mm, and can be represented with the following equation:

$$\Phi_{superGaussian} = A * e^{0.5(\frac{r}{\sigma})^n} \quad (3.19)$$

where:

$$r = z \tan\theta \quad (3.20)$$

In the above equations, A is the maximum or peak incident energy fluence (J/mm^2), z is the perpendicular distance from the source to a point along the central axis of the beam, θ is the divergence angle of the laser beam, σ is the standard deviation of the super-Gaussian lateral beam profile, n is the order of the super-Gaussian distribution. The broad beam output of the fiberguide was approximated using multiple single sources with super-Gaussian outputs. In our experimental setup, a match in beam profile was obtained for σ=3.8 and n=2.9. The radius of the fiberguide source is 0.3cm. Besides the super-Gaussian beam from the fiberguide, a flat broad beam with radius equal to the output port of the integrating sphere (port radius 0.9cm) was used to characterize the

output of the integrating sphere. The beam characteristics were measured using a

calorimeter (gold standard) and were given as input to the MC code to emulate the

illumination conditions used in the optical dosimetry setup.

We also added additional functionalities to the Monte Carlo to emit broad beam profiles

such as converging and diverging beams as emitted when light beams pass through

convex and concave lenses. This is of particular importance to researchers who wish to

explore the effect of different beam profiles on photon energy distribution in tissues.

In order to implement the simulation of converging and diverging beams, we allow the

user to select the beam parameters such as the aperture size (radius) and focal distance,

e.g., the real or virtual focal length for converging or diverging beams, respectively.

In order to simulate converging and diverging beams, we need to define the angle of the

photon source vector for each individual pencil beam. We define the emission angle θ

for a beamlet as:

$$\theta = tan^{-1}\left(\frac{r}{f}\right) \quad (3.21)$$

where f is the focal depth and r is the radial distance from the center of the aperture of

the point source (or do you mean beamlet). The parameter r is selected randomly from

0 to R, where R is the radius of the source aperture. The angle of the photon beamlet

from this point within the aperture is $\left(\frac{\pi}{2} - \theta\right)$. For a converging beam the initial photon

vector is defined by –sin(θ) and –cos(θ) and for the diverging beam this vector is defined

by sin(θ) and cos(θ). The equatorial angle (Φ) is randomly chosen from 0 to 2π.. The

photon vector directions are then calculated using equations 3.6, 3.7 and 3.8.

3.2.2   Optical Dosimetry Probe Design and Calibration

Two models optical dosimetry probes constructed with Nylon and Titanium Dioxide

spherical tips were fabricated and compared, specifically their sensitivity and

isotropicity of response.

The Nylon spheres have been widely used for photodynamic therapy and were made of

Nylon[TM] due to their isotropic response [26]. These were used as the standard of

reference to compare the performance of Titanium based probes. TiO2 probes are

made from a mixture titanium dioxide (Du Pont Ti-Pure R-900) and a clear two-part

epoxy (Tra-Con BA-F114) in a ratio of 9.1 mg TiO2 to 1 ml of the epoxy [28, 29]. Titanium

dioxide was selected due to its particle size of around 410nm [28], which results in

optimal scattering at 820nm, the wavelength is approximately twice the particle size [28]

and in the center of the NIR spectrum (700-920nm). Since the wavelength used in our

studies is 800nm, the titanium probes have been designed to show a higher sensitivity

than the Nylon probes. The titanium based probe tips were fabricated using a specially

designed mold [70]. A fiber optic cable (BFL48-400, 4mm diameter, 0.48 numerical

aperture) was inserted within the cured spheres at a depth of approximately 1/3 of the

sphere's radius [72]. The Nylon based probes were approximately 3.175mm diameter

and were machined in a multistage process [70]. The other end of the fiber optic cable

was connected to PIN photodiode (ET-2030, Electro Optics Technology Inc.) though a

SMA-905 connector and the voltage output was read using a digital oscilloscope

(Tektronix TDS3052B).
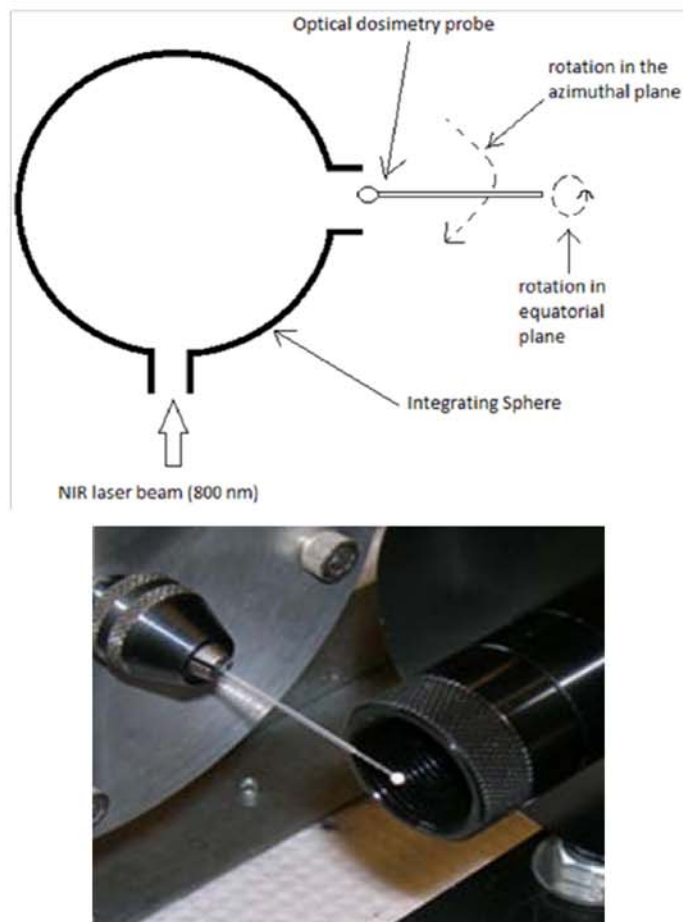
Figure 3.3 Setup for calibration of the Optical dosimetry probe: measuring isotropicity
(in equatorial and azimuthal planes) of the probe

First, the isotropic response of the probe was measured. The experimental setup shown

in Figure 3.3 was used to measure the probe's equatorial and azimuthal response. The

probe is mounted on and rotated by a rotary stepper motor, while keeping the same central location of the probe. At each equatorial and azimuthal angle, the probe is illuminated by a uniform broad beam of diffuse light formed by laser light (800 nm) emanating from an integrating sphere (Melles Griot two port integrating sphere)and its response, the output rms voltage, was measured at each angle. The isotropicity is measured by calculating the coefficient of variation, the ratio of standard deviation to mean of the rms value over all the angles. The range of angles was 0 to 360 degrees for equatorial measurements, and 0 to 150 degrees for azimuthal. The angular span for Azimuthal measurements was limited due to physical limitations of the setup which prevented larger angles due to presence of the integrating sphere. The individual rms voltage measured by the probe was normalized to the power measured using a calorimeter.
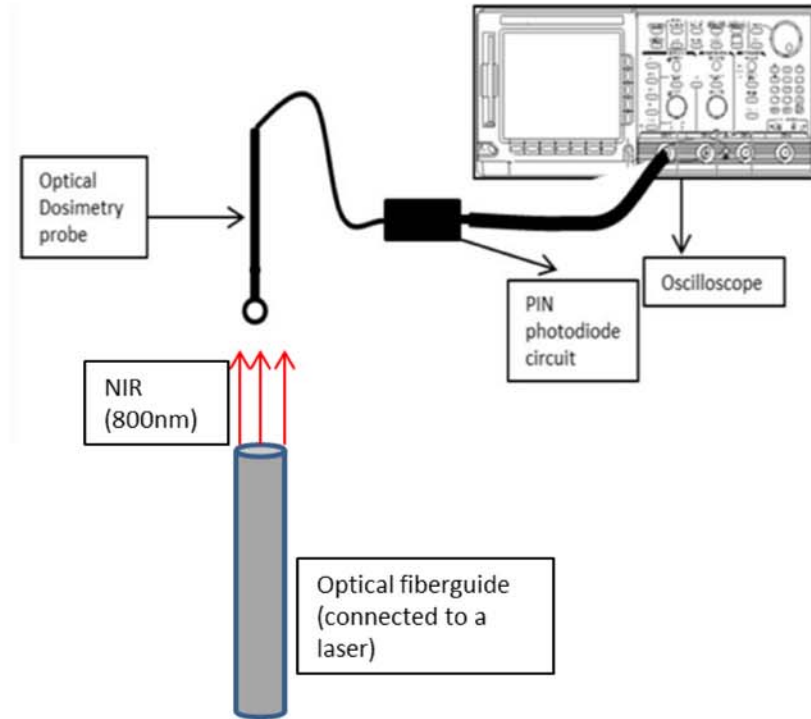
Figure 3.4 Setup for calibration of the Optical dosimetry probe: measuring the linearity of the probe to incident laser fluence.

Second, experiments were performed to measure the linearity and sensitivity of the probe (figure 3.4), and calibrate the dosimetry probe response to calorimeter (Ophir CE, [Nova 2 Ophir: 3A-P-SH-VI], aperture 12mm). The probe was illuminated with a pulsed laser beam (800 nm; 10 Hz repetition rate) with an output of 10.2 mW/cm^2 fluence rate and total output energy of 0.02 J/pulse. The probe and the calorimeter are translated along the beam axis (in air) and the photon fluence is measured at different positions. The integrated voltage normalized to the exposed area of the probe (ϕ_{probe}, mV/mm^2) was plotted as a function of calorimeter measurements ($\phi_{calorimeter}$, mW/mm^2) and fitted to a line.

$$\Phi_{probe} = \frac{\Phi_{calorimeter} + 1.7296}{590.46} \quad (3.22)$$

Note that the probe voltage signal was filtered using a bandpass Butterworth filter to remove high frequency noise in the probe response. The photon fluence is proportional to integral of the probe voltage output over the time of the laser pulsed. The probe's integral voltage as well as the calorimeter power was normalized to the exposed surface areas of these detectors, where the probe (spherical) surface area is 7.065mm^2 and the calorimeter (circle) surface area of 113.04mm^2.

The linear relationship in equation 3.19, used to quantify the photon dose in air, was modified to account for the optical fluence in liquid brain phantoms. The light entering the dosimetry probe depends on the ratio of the refractive index of the TiO2-expoxy sphere to the medium. The refractive index of probe tip lies between the refractive indices of titanium dioxide (approximately 2.73) [29] while that of the epoxy (around 1.53). Since the refractive index of air is smaller than that of water, the probe response in water is smaller as more light will escape the probe when placed in water. The reflectance factor is 0.41 for the probe-to-air interface (n_{probe}/n_{air} is 2.5), and 0.74 for the probe-to-water (n_{probe}/n_{water} is 1.88) [26]. The difference in the refractive index and reflectance between probe-air and probe-water interfaces (water and tissue have similar refractive index of 1.329) must be accounted for to quantify photon dose in water. In order to determine the calibration factor, we measured the probe response in air and water within a cuvette illuminated by a diffuse broad uniform beam emanating from an integrating sphere (same setup as figure 3). The probe was placed inside the cuvette, 0.2cm from the surface. First the probe response was measured in air (ϕ_{air}) and

then measured again by filling the cuvette with water (ϕ_{water}), without changing the

position of the probe with respect to the cuvette and the laser source. By accounting for

the water attenuation (μ_{water} of 0.02cm^{-1} and a path length of 0.2cm) and the difference

in the beam spread due to change in refractive index, the calibration factor (CF) was

determined experimentally to be 1.318, using the following equation:

$$CF = \frac{\Phi_{air} \left(e^{-\mu_{water}*l}\right) \left(\frac{fwhm_{air}}{fwhm_{water}}\right)}{\Phi_{water}} \quad (3.23)$$

The difference in the beam spread difference between the cuvette-air setup versus the

cuvette-water setup is accounted for by multiplying the fluence measured in air with the

ratio of the measured beam spreads: fwhm$_{air}$=40mm and fwhm$_{water}$=42mm, or a ratio of

0.9091.The experimentally derived calibration factor is then used for absolute photon

quantification by multiplying it to the probe response measured within tissues and

tissue-like media as follows (from equation 1 and 2):

$$\Phi_{absolute} = \frac{(CF*\Phi_{tissue})+1.7296}{590.46} \quad (3.24)$$

where $\phi_{absolute}$ is the absolute dose in mW/mm^2 and ϕ_{tissue} is the probe response

(mV/mm^2), which is proportional to fluence measured in the tissue over the surface

area of the probe.

3.3   Results

3.3.1   Monte Carlo Optimization

The Monte Carlo software was modified to simulate a super-Gaussian beam profile by

generated by laser light passing through an optical fiberguide. Figure 3.5 shows the

lateral fluence profiles generated by the MC and that measured by the calorimeter.

Modifications were also done to the original MCX software to simulate converging and

diverging beams, which are shown in figures 3.6 and 3.7. These were added for future

analysis of complex beam setups with lenses of specified focal length and numerical

aperture.
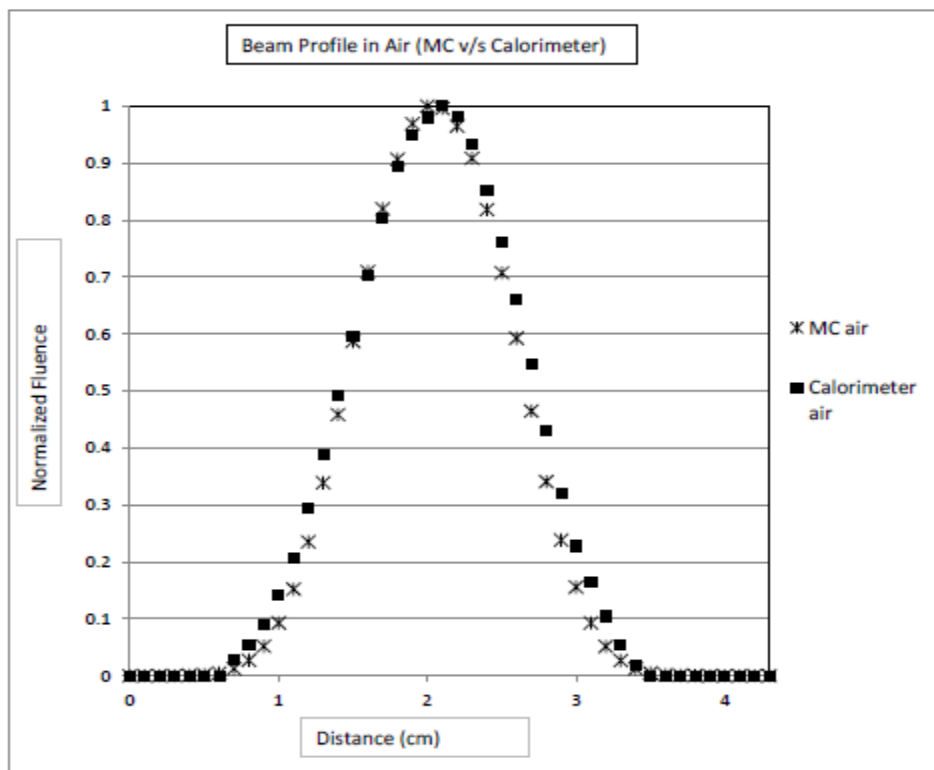
Figure 3.5 Super-Gaussian beam generated by the Monte Carlo, compared with the
optical fluence measured using a calorimeter [63].
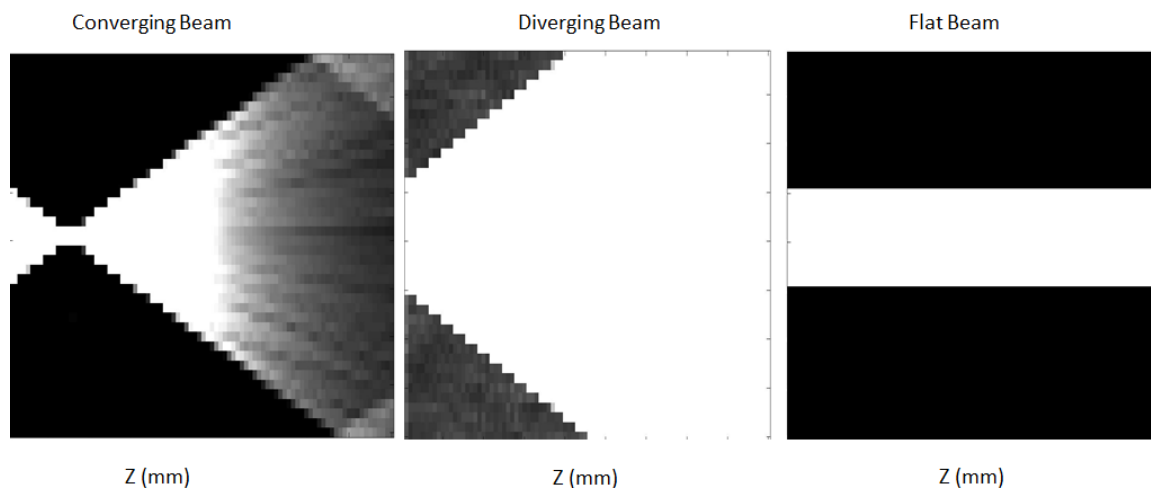
Figure 3.6 Images of converging, diverging and flat beams generated by the Monte Carlo.

Figure 3.7 shows an MC simulation of three convex lenses with different focal lengths and with an aperture of 5mm. The increase in focal distance leads to a widening of the focal spot in the z-direction as expected.

3.3.2   Optical Probe Calibration

The optical dosimetry probe was designed to quantify the localized fluence distribution in tissues with a high degree of accuracy. This design was compared with standard probes made from Nylon in order to analyze the advantages in linearity and anisotropy of the novel probe model. The probe response was then characterized to quantify the absolute photon fluence in tissues. This procedure involved the use of filtering to reduce the statistical noise in the probe voltage and the determination of probe characteristics in water (with tissue equivalent refractive index) versus those in air.
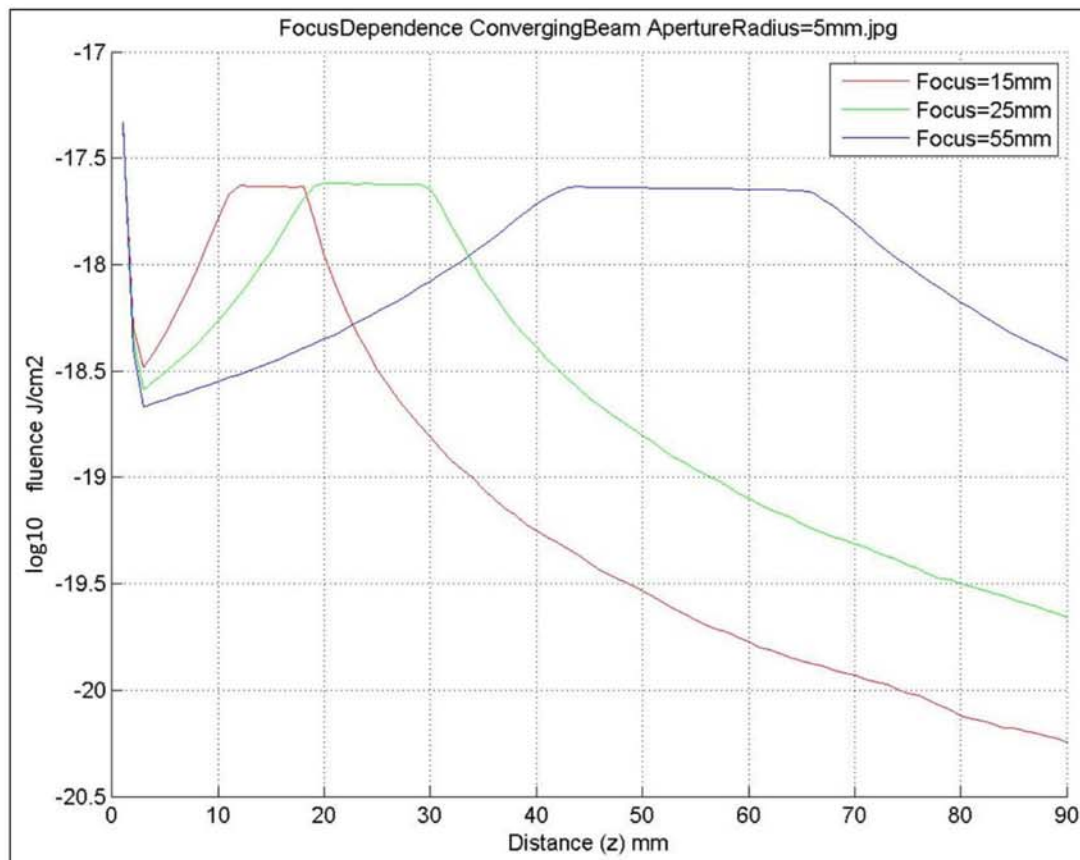
Figure 3.7 Simulation plots of converging beams along beam axis in water. Three converging beams were simulated with the same aperture size (radius 5mm) and with different focal depths (15mm, 25mm, 55mm). The larger focal depths show a broader distribution of photon fluence (along the beam axis) with increase in focal depth.

The isotropicity (coefficient of variation) of Nylon and Titanium based optical dosimetry probes are shown in figure 3.8. The titanium based probes showed a better isotropicity with an equatorial coefficient of variation 0.0386 versus 0.1929 for Nylon probes and an azimuthal coefficient of variation of 0.216 for titanium versus 0.441 for Nylon. A titanium based probe with a 1.5mm diameter was selected for further dosimetric studies and had an equatorial coefficient of variation of 0.0721 and an azimuthal coefficient of variation 0.2959.
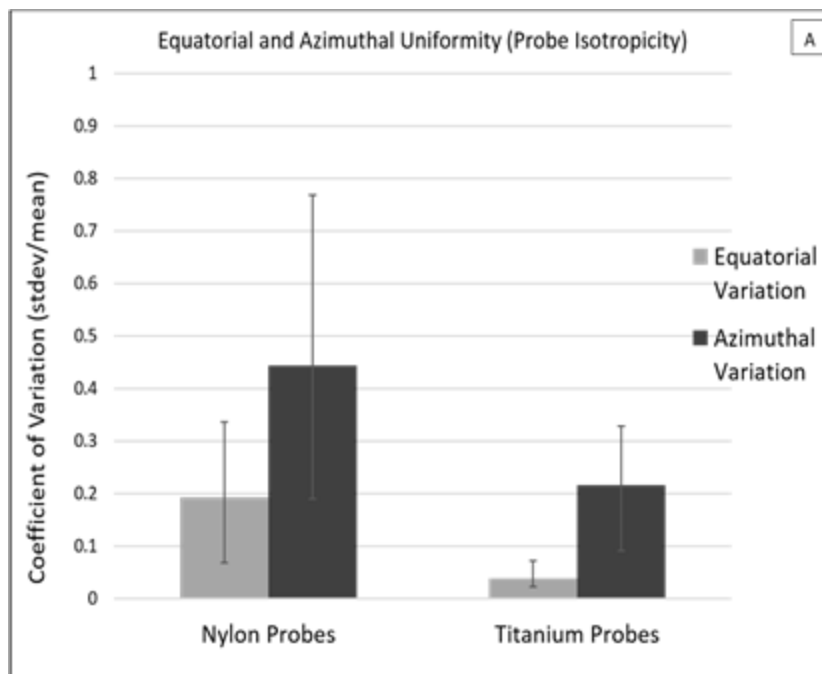
Figure 3.8 Probe Isotropicity of Titanium v/s Nylon probes. The coefficient of variation (standard deviation/average rms voltage) was calculated for probes made of Nylon and Titanium. The error bars show the minimum and maximum values of variation in individual probe response. The Titanium based probes showed a more isotropic response in the equatorial and azimuthal directions. A 1.5mm diameter Titanium probe was selected for further dosimetric studies.

Figure 3.9 shows the linearity of response of the 1.5mm Titanium based probe. The probe response is linear over a dynamic range of $0.01074mW/mm^2$ to $0.031316mW/mm^2$ as measured by the calorimeter. The standard error (Standard Deviation/ $\sqrt{n}$) and percentage error variation in probe response was quantified by measuring multiple probe response in air over distances 10.1 to 18.1cm from the fiberguide surface. The error in probe response is 1.695% (standard error = 0.226) and the % error in calorimeter readings was 1.1299% (standard error = 0.00495). On the other hand, the variation of the laser light emitted from the fiberguide over time was approximately 3%. Thus the error due to variation in pulsed optical power of the laser

was the major source of error in our measurements. These showed that Titanium

probes are better suited to optical dosimetry studies, as compared to Nylon probes, and

were used in brain phantom studies. While Nylon probes have been used before in

dosimetry studies, this is the first time that titanium probes were designed with a better

isotropic response.
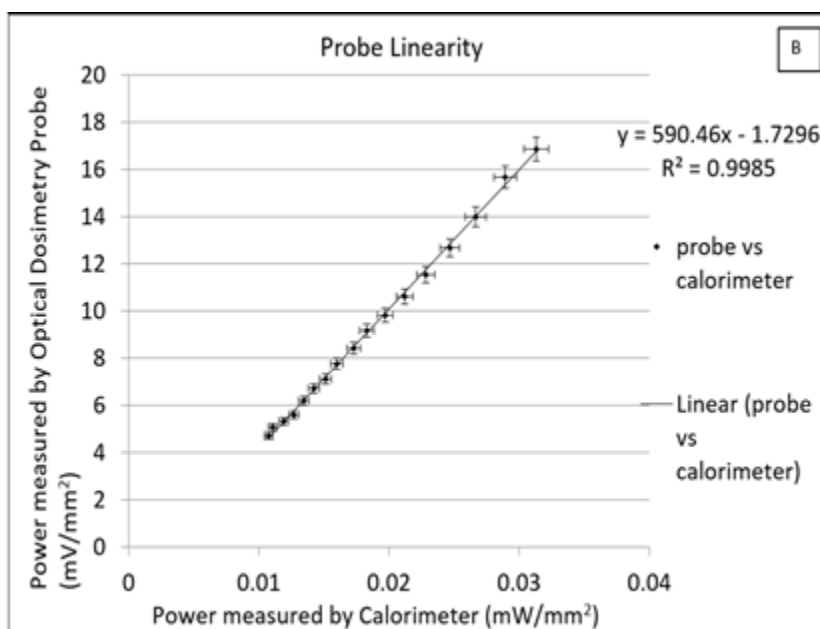
Figure 3.9 Probe linearity: graph of total voltage (area under pulse) (mV/mm^2) measured by a 1.5mm diameter Titanium probe versus the power measured by a calorimeter per unit surface area (mW/mm^2). The probe response is linear over a dynamic range of 1.2mW to 3.5mW as measured by the calorimeter. The error bars represent 3% variation in pulsed laser power fluctuation measured by the probe and calorimeter.

The filtering of the probe response reduces the noise in the probe voltage and provides

a clean signal. The Butterworth filter used can be tuned to optimize the signal to noise

ratio and removes the high frequency noise in the probe voltage, mainly attributed to

electronic noise externally induced in the PIN photodiode circuit. The use of the filtered

signal also reduces the noise dependency of the measured fluence as we saw that the

noise variations in the measured signal mainly affected the measured output in the low

fluence regions, where (S/N) ratio is low. The filtering step (final versus initial signal) is

shown in figure 3.10. It is clearly seen that the high frequency noise at the periphery of

the signal is reduced. This can be even reduced further by adjusting the filter

coefficients, based on the operator's discretion.

In order to quantify the measured probe voltage, there are several methods which can

be used. Some commonly measured parameters are the root mean square (RMS)

voltage, mean voltage and maximum voltage. In our studies we found that the RMS

voltage is a reliable parameter can be used to quantify the signal. However the RMS

voltage also depends on the signal noise and can be problematic if the noise level

changes with photon fluence measured. Thus in order to quantify the photon fluence,

we used the integral of the voltage (or area under the peak) of the measured signal. This

quantity can be made independent of the noise level by summing only those voltages

above a certain noise threshold level. In our studies, we found that a threshold of 5% of

the maximum value of the measured voltage was sufficiently above the average noise

variations at the signal periphery. Thus, while RMS value is a quick means to estimate

the measured fluence, the area under the peak can be a better measure of the absolute

photon fluence, provided all the necessary calibration factors are calculated.
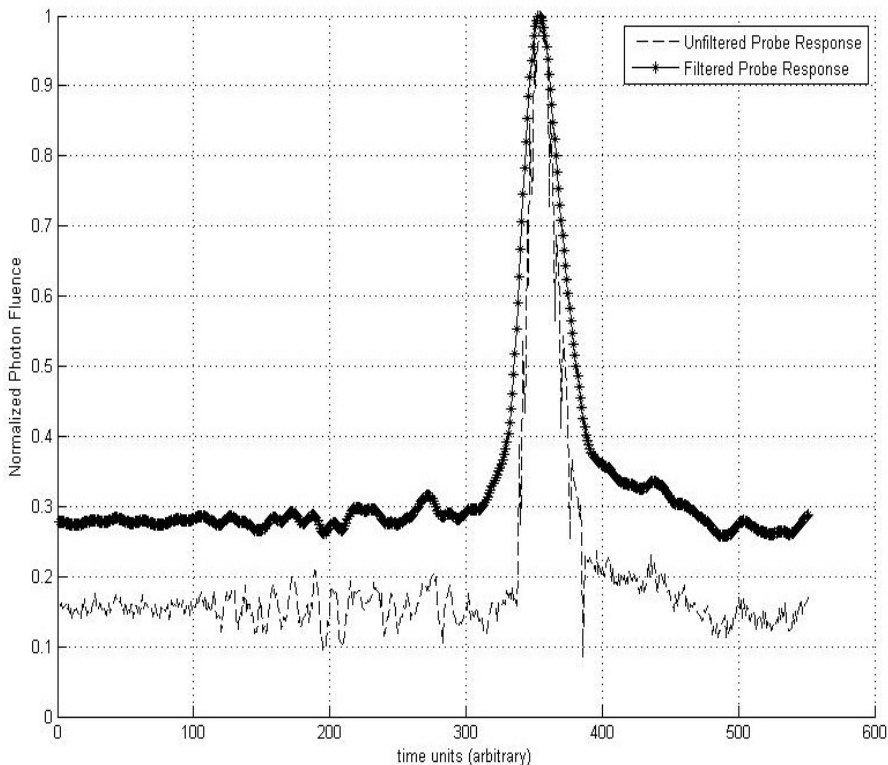
Figure 3.10 Filtering the response using a Butterworth band-pass filter. The signal to noise ratio is significantly improved by using the filter.

In order to calculate the absolute photon fluence in tissues and tissue-like media, the

probe voltage measured within the medium must be multiplied by the calibration factor

to account for the change in photon loss in the probe-medium interface with respect to

the probe-air interface, where the calibration was performed. Since the refractive index

of tissues is nearly same as that of water, the calibration factor obtained for water can

be used for biological media. The probe calibration factor was determined to be 1.32.

The technique presented (using equations 3.22, 3.23, 3.24) provides a simple method to

determine the calibration factor experimentally, and is a novel addition to our research.

It is important to note that while equation 3.23 remains same for any probe, the

equations 3.22 needs to experimentally determined, so as to derive equation 3.24 for

absolute photon dose quantification.

3.4   Discussion

The Monte Carlo code was optimized to emit a super-Gaussian beam profile. Its voxel

based design allows us to clearly define object boundaries and specific optical

properties of each voxel in the volume to be simulated, generating a photon fluence

(units: $J.mm^{-2}.s^{-1}$ or $photons.mm^{-2}.s^{-1}$) \ and an absorbed energy (units Joules) map. The

latter is calculated by multiplying the simulated fluence ($J.mm^{-2}.s^{-1}$) with the absorption

coefficient (units mm^{-1}) of the voxel, volume (units: mm^{3}) of the voxel and the length of

the time period (units: seconds). The 3D voxelated output of the Monte Carlo is can be

conveniently integrated and analyzed with 3D medical imaging modalities such CT, MR,

Ultrasound, etc. Thus absolute photon quantification using Monte Carlo has the

potential to be used for image guided therapy. The reduction in simulation times

(couple of hours) of the CUDA based Monte Carlo also improves its potential to be

applied in the clinic for calculating the photon dose in optical based therapies.

We designed an optical dosimetry probe with a linear and isotropic response, and with

superior sensitivity compared to Nylon probes. These dosimetry probes can now be

used for in vitro and in vivo studies for localized measurement of the absolute photon

fluence. The calibration of the dosimetry probes allows us to measure its linearity and

isotropicity and derive the calibration factors necessary to measure the absolute energy

fluence in mW/mm^2. The calibration factor (1.32) derived in this study accounts for the difference in the sensitivity of the probe in air and water. The other calibration factor is the isotropic sensitivity of the probe and depends on the probe orientation. This factor gives the % error in probe response based on the azimuthal and equatorial orientation of the probe. An average error over all the angles is sufficient to understand the variations in measurement based on probe orientation, with the goal of having each measurement independent of the probe's absolute position in the media. More studies using goniometric measurements may improve the accuracy of the measurements and are recommended before using the probe in a clinical setting. Our study has shown the advantages of using Titanium Dioxide probe over traditional probes made of Nylon for dosimetry studies for NIR wavelengths of around 800nm. More dosimetry probe materials can also be researched for better sensitivity at larger infra-red wavelengths if necessary.

4   SPECIFIC AIM2: VALIDATION OF MONTE CARLO IN TISSUE PHANTOMS

4.1   Introduction

In order to be used as a therapeutic tool, the Monte Carlo software needs to be validated. The Titanium Dioxide based optical dosimetry probe, described in the previous chapter, allows us to accurately measure photon fluence distribution with millimeter resolution, high sensitivity, and negligible orientation dependencies, , compared to previous Nylon-based dosimetry probes. In this chapter we describe the design of accurate tissue phantoms of white matter, gray matter, and skull bone used to validate the Monte Carlo generated photon fluence. In all these studies, the optical dosimetry probe serves as a gold standard photon energy fluence and its uncertainty..

4.1.1   Optical Phantom Characteristics

The design of optical phantoms requires an accurate and precise measure of the absorption coefficient ($\mu_a(\lambda)$), scattering coefficient ($\mu_s(\lambda)$) [or reduced scattering coefficient $\mu_s^1(\lambda) = (1\text{-}g)\,\mu_s(\lambda)$], anisotropy factor (g) and refractive index (n), at a wavelength/s of interest (λ) of the materials used to represent skull bone, white and gray matter. Since tissues are made of molecules which scatter and absorb photons, an optical tissue phantom is composed of a combination of scattering (e.g. Intralipid, Titanium dioxide, Aluminum Oxide, Polymer Microspheres, Quartz Glass Microspheres) and

absorbing materials (e.g. India Ink, Molecular dyes such as Indocyanine Green (ICG), Fluorophores), each in varying proportion based on their individual absorption and scattering properties [73-77]. These absorbers and scatterers are added to water or agar, which provides a stabilizing medium for uniform distribution of the absorber and scatterer molecules, and defines the refractive index of the resulting phantom. An optical phantom should be designed such that its optical properties closely match those of the corresponding tissue at the wavelength of interest. This however is a complex problem due to the apparent mismatch between "non-absorption" related properties ($\mu_s(\lambda)$, g, n) of absorbers and "non-scattering" related properties ($\mu_a(\lambda)$, g, n) of scatterers across different wavelengths (λ). One way to reduce this complexity is to select materials that have closely matching g and n values to tissue (water and agar), a pure scattering media with negligible absorption properties, and a pure absorber with negligible scattering properties, while allowing uniform mixing of absorber and scatterer molecules [73].

4.1.2 Spectro-photometer Calibration

In this study, intralipid was used as a scatter and India ink as an absorber in concentrations that resemble the optical properties of white matter, gray matter and skull bone. For each tissue type used in the brain phantom, the absorption coefficient of India ink and scattering coefficient of intralipid were determined using a spectro-photometer which served as the gold standard to measure absorption and scattering properties. While absorption properties of India ink (units: %Concentration^{-1}cm^{-1}) vary from batch to batch in commercially available samples, the variation in the scattering properties (units: %Concentration^{-1}cm^{-1}) of Intralipid are less across different samples. This is

mainly due to the fact that intralipid composition is controlled for medical use. Both these properties were validated using a spectro-photometer and calibration curves of $\mu_a(\lambda)$ and $\mu_s(\lambda)$.
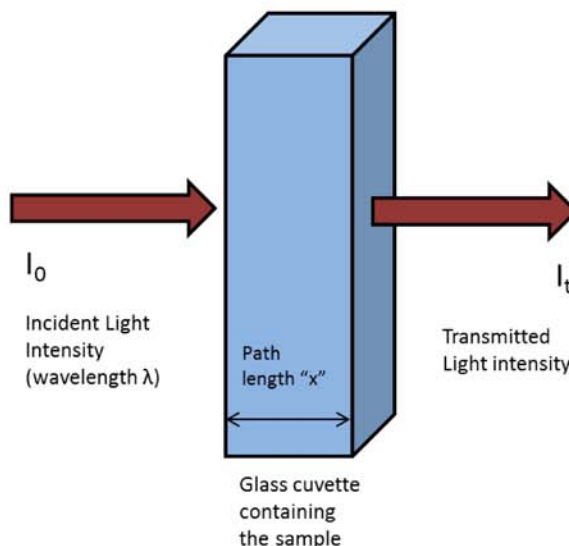
Figure 4.1 Measurement of light transmission in a Spectro-photometer. A fine pencil beam of a specific wavelength is transmitted across a sample contained in a glass cuvette with a fixed path length. The absorbance of the sample is calculated using Beer Lambert's law [78].

The spectro-photometer measures the transmission of light across samples for specific wavelengths of interest. It uses the Beer Lambert's law [78] to calculate the absorbance of the medium from the incident light intensity (I_i), transmitted light intensity (I_t) and optical path length (x). For a path length of 1 cm, the absorbance (A) (cm^{-1}) of a sample is given by [78]:

$$A = \log_{10}\left(\frac{I_i}{I_t}\right) \quad (4.1)$$

For a purely absorbing medium the absorbance measured by the spectrophotometer is related to the absorption coefficient of the medium by:

$$\mu_a(\lambda) = \frac{log_e(A)}{log_e(10)} \quad (4.2)$$

where "log_e" is the natural logarithm. Similarly the scattering coefficient of a medium with a low concentration of scatterers can also be derived from the absorbance measurement of the spectro-photometer:

$$\mu_s(\lambda) = \frac{log_e(A)}{log_e(10)} \quad (4.3)$$

Equation 4.3 is true only if the transmitted light intensity is collimated, does not undergo multiple scattering events and if the detector aperture is very small [76]. This places restrictions on the range of concentrations across which the scattering properties can be measured using the spectro-photometer. In this study we validated the scattering properties of the intralipid medium across extremely low concentrations using probe measurements as well as by comparing to past studies. Past studies by Van Staveren [76] have measured the optical properties of intralipid, which can be derived using the equations [76]:

$$\mu_s(\lambda) = 0.016\lambda^{-2.4} \quad (4.4)$$

and

$$g(\lambda) = 1.1 - 0.58\lambda \quad (4.5)$$

where λ is in micrometers (0.4< λ <1.1) and the scattering coefficient $\mu_s(\lambda)$ is in mL$^-$ ^{1}.L.mm^{-1}. This yields an anisotropy factor of g(λ) = 0.636 and a reduced scattering

coefficient of 9.95 (%Concentration)$^{-1}$.cm^{-1} at λ = 800 nm. In this study we have used the anisotropy factor derived from equation 4.5 and will compare the scattering properties of intralipid to those obtained through equation 4.4.

4.1.3 Probe and Monte Carlo based validation of intralipid

To further verify the optical properties of intralipid solutions, we did another study using the dosimetry probe to measure the extinction coefficient of intralipid solutions. The extinction coefficient derived by the probe measurements were then matched by the Monte Carlo. The corresponding scattering coefficients which showed the best match to data were selected as the true values for that concentration. This additional study cross validates the spectro-photometer studies [76] shown by equation 4.4. The reasoning behind this study was to be absolutely sure that the scattering coefficient per unit volume of the 20% intralipid samples used in our studies were of the same property as the 10% intralipid samples used by the Van Staveren study.

4.2   Materials and Methods

4.2.1   Characterization of Optical Phantoms

Optical brain phantoms were designed to emulate the absorption and reduced scattering coefficients of white matter, gray matter and skull bone at 800nm [79, 80]. Previous studies have shown that reliable optical phantoms can be built using India ink (absorber) and intralipid (scatterer) [74 – 77] , in addition to the optical absorption by water molecules (μ_a = 0.02cm^{-1}) [81].

The absorption coefficient of India ink (Higgins non water proof black ink) and the scattering coefficient of intralipid (Intralipid 20% from Fresenius Kabi), at 800nm wavelength, was determined and validated using a spectro-photometer (Shimadzu UVmini 1240 Spectrophotometer), which served as the gold standard to measure absorbance. The scattering properties of intralipid can be determined using the spectrophotometer for low concentrations and was found to have the average value of $9.524\ cm^{-1}\ \%Concentration^{-1}$, compared to $9.95\ cm^{-1}\ \%Concentration^{-1}$ as shown in past studies by Van Staveren [76]. Figures 4.2 and 4.3 show the calibration curves of the absorbance versus concentration of India ink and Intralipid, and the linear fit was used to design optical phantoms that resemble white matter, gray matter and skull bone, similar to Van der Zee [79] and Firbank [80]. In Tables 4.1 and 4.2, the measured ex vivo optical properties (absorption and scattering coefficients and anisotropy factor) of skull bone, gray and white matters and those used in our research studies are shown (the latter derived from figures 4.2 and 4.3).
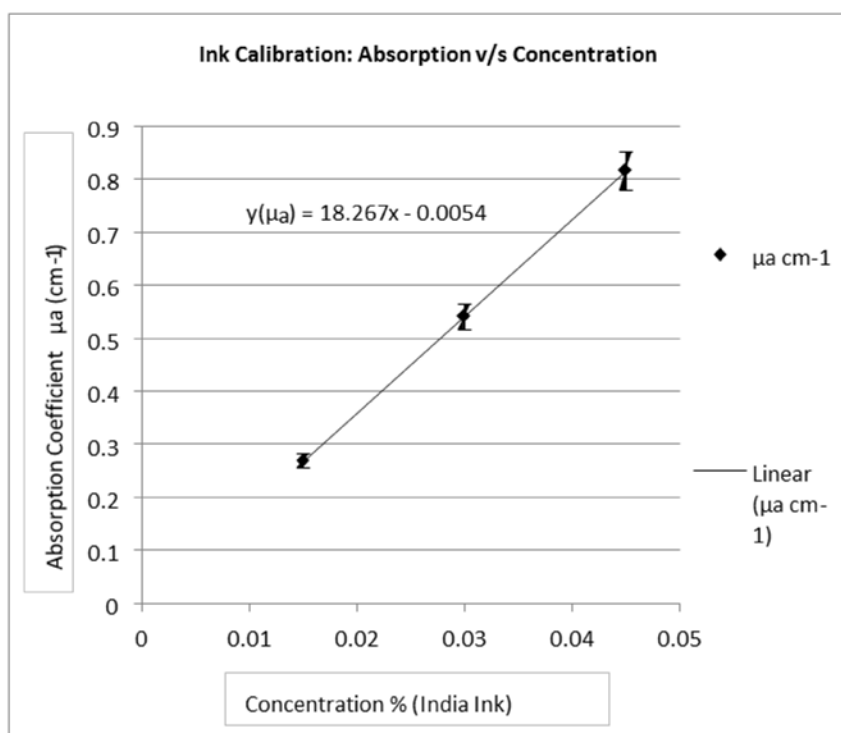
Figure 4.2 Calibration curve of spectrophotometer measured absorbance versus %Concentration of India ink. The error bars represent minimum and maximum absorbance.
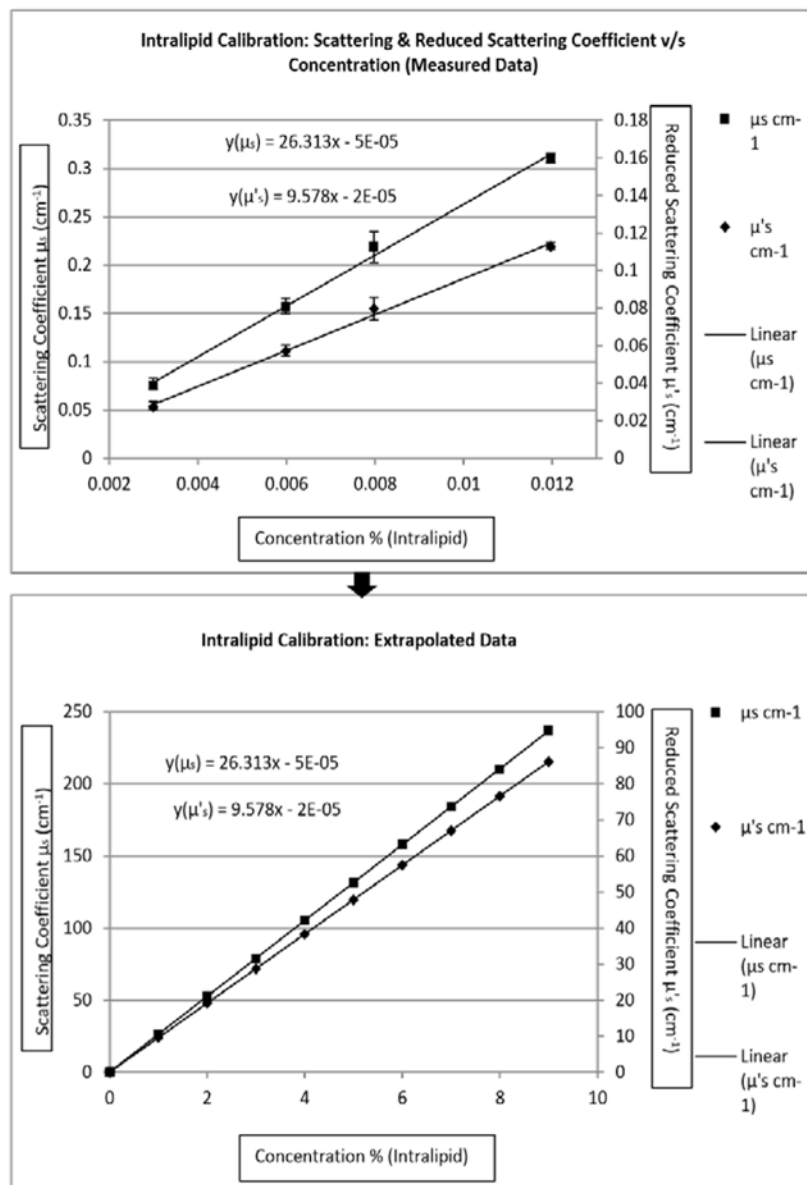
Figure 4.3 Intralipid Scattering: Upper figure represent measured values of scattering coefficients (µs and µs1) versus %Concentration of Intralipid using a spectrophotometer. The error bars represent minimum and maximum values. Lower figure shows extrapolated values from the linear relationship derived from the measured values.

Both homogeneous as well as heterogeneous phantoms were made using various concentrations of India ink and Intralipid. The phantom composition for homogeneous phantom was a solution of India ink and intralipid in water, while the heterogeneous

phantoms comprised of layers of 1% agar doped with India ink and intralipid to

represent skull bone and gray matter, and topped with a solution of white matter. The

agar phantom preparation involved boiling a solution of India ink (with predetermined

concentration) and 1% agar (Fisher Scientific Laboratory Grade Agar A3600-500) in a

microwave at 95 degree Celsius and adding intralipid to the solution after being stirred

and cooled to below 45 degrees Celsius. The scattering properties of agar and

absorption properties of India ink were also measured using a spectrophotometer for

each individual sample used in the study, while the scattering properties of intralipid

were derived from the linear relationship in figure 4.3.

Table 4.1 Optical Properties of Brain Tissues [79, 80]

Tissue Type	Absorption Coefficient (μ_a) (cm^{-1})	Scattering Coefficient (μ_s) (cm^{-1})	Anisotropy Factor (g)	Reduced Scattering Coefficient (μ'_s) (cm^{-1})
White Matter	0.05	550	0.85	82.5
Gray Matter	0.35	700	0.965	24.5
Skull Bone	0.24	184	0.9	18.4

Table 4.2 Phantom Composition [63]

Phantom Type	Tissue Type	Intra lipid %	Ink %	Absorption Coefficient (μ_a) (cm^{-1})	Scattering Coefficient (μ_s) (cm^{-1})	Anisotropy Factor (g)
Liquid Phantom	White Matter	7.5	0	0.002	197.352	0.636
Liquid Phantom	Gray Matter	2.36	0.023	0.3792	62.187	0.636
Liquid Phantom	Skull Bone	1.82	0.0156	0.26	47.922	0.636
Solid Phantom	Gray Matter	2.56	0.0195	0.35	67.308	0.636
Solid Phantom	Skull Bone	1.92	0.0134	0.25	50.549	0.636

4.2.2   Validation of 3D Monte Carlo in brain phantoms using Optical dosimetry

As described in the previous section, liquid optical phantoms, resembling white matter,

gray matter and skull bone, were designed using predetermined concentrations of India

ink and Intralipid. The setup for the light dosimetry in the phantoms is shown in figure

4.4. Two sources of NIR light (an integrating sphere and an optical fiberguide) were used

to illuminate the phantoms, both of which were connected to the laser source (same

specifications as used in the calibration process). The dosimetry probe was inserted into

the phantom and translated using a 3D translation micrometer stage and used to

measure the optical fluence distribution at various x, y and z locations within the

phantom. The x, y and z fluence distribution generated by the Monte Carlo was

compared to the probe measurements to the test the validity and accuracy of the

Monte Carlo code. The percentage match of the Monte Carlo was calculated relative to

the probe measurements to estimate the level of confidence of fluence estimation. The %

difference between the probe measured fluence and the Monte Carlo was calculated

both along and perpendicular to the beam axis.
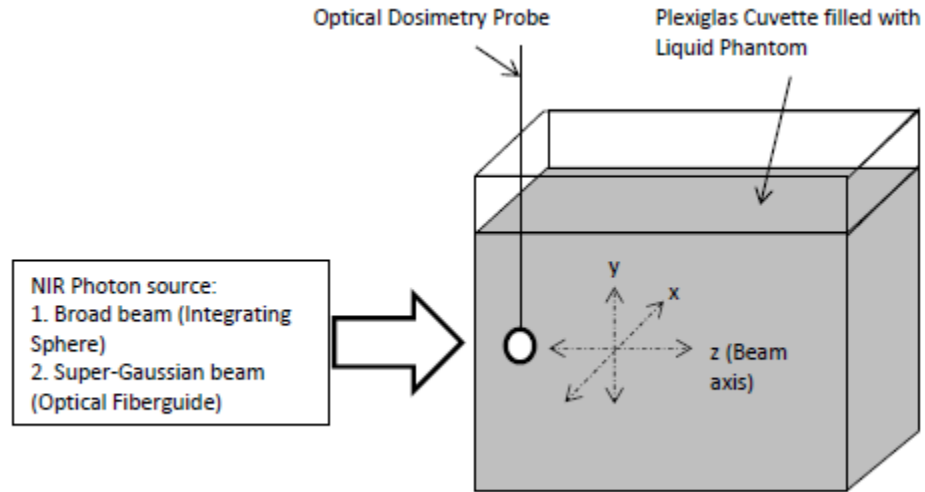
Figure 4.4 Setup for Optical dosimetry in a liquid phantom. The optical dosimetry probe is translated within a plexiglas cuvette filled with liquid phantom, and illuminated by an NIR source.

In order to quantify the photon fluence (Φ_{Joules}) in J/cm^2, we converted the output of the Monte Carlo fluence (Φ, photons/mm^2) as follows:

$$\Phi_{Joules} = \Phi \frac{hc}{\lambda} \quad (4.6)$$

where h is Planck's constant (6.626e-34 J.s), c and λ are the speed and wavelength of light in the medium. The energy deposited in the tissue is obtained by multiplying the photon fluence with the absorption coefficient μ_a and the volume of the voxel (v):

$$\Phi_{absorbed} = \Phi \frac{hc}{\lambda} \mu_a v \quad (4.7)$$

4.3   Results

4.3.1   Optical Dosimetry and Monte Carlo Validation in Homogeneous Phantoms

The optical fluence measured by the dosimetry probe in white and gray matter phantoms

was compared to the Monte Carlo generated fluence. The design of optical phantoms is

crucial for accurately determining the localized distribution of fluence with the probe

before validating it using Monte Carlo. Figures 4.5 and 4.6 show the comparison between

the probe measurements and the Monte Carlo in brain phantoms for two different

illumination profiles, the flat diffuse beam produced by the integrating sphere and the

super-Gaussian beam emanating from the optical fiberguide. Comparisons were made

along the central axis of the beam and in the direction perpendicular to the beam axis at

different depths, as shown in figure 4.7. These plots reveal the energy fluence measured

by the probe matched Monte Carlo simulations both along and perpendicular to the beam

direction.
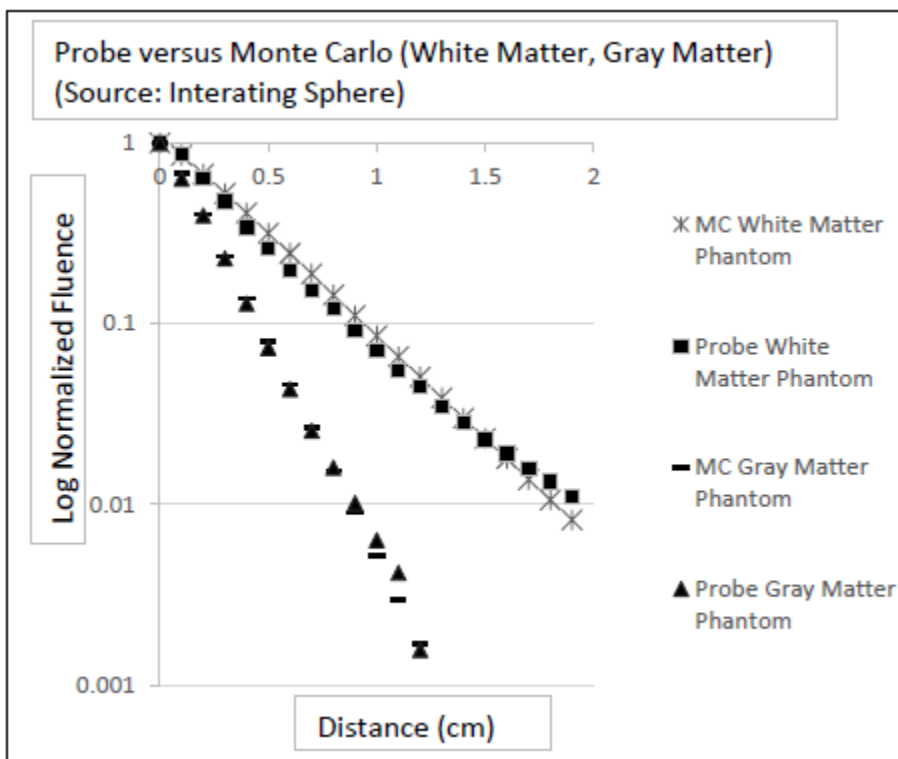
Figure 4.5 Optical dosimetry in white and gray matter phantoms. The photon source used is an integrating sphere connected to a pulsating laser source. The graphs show the exponential decrease of photon fluence along the beam axis in white and gray matter mimicking phantoms. The Monte Carlo generated fluence closely matches the fluence measured by the probe.
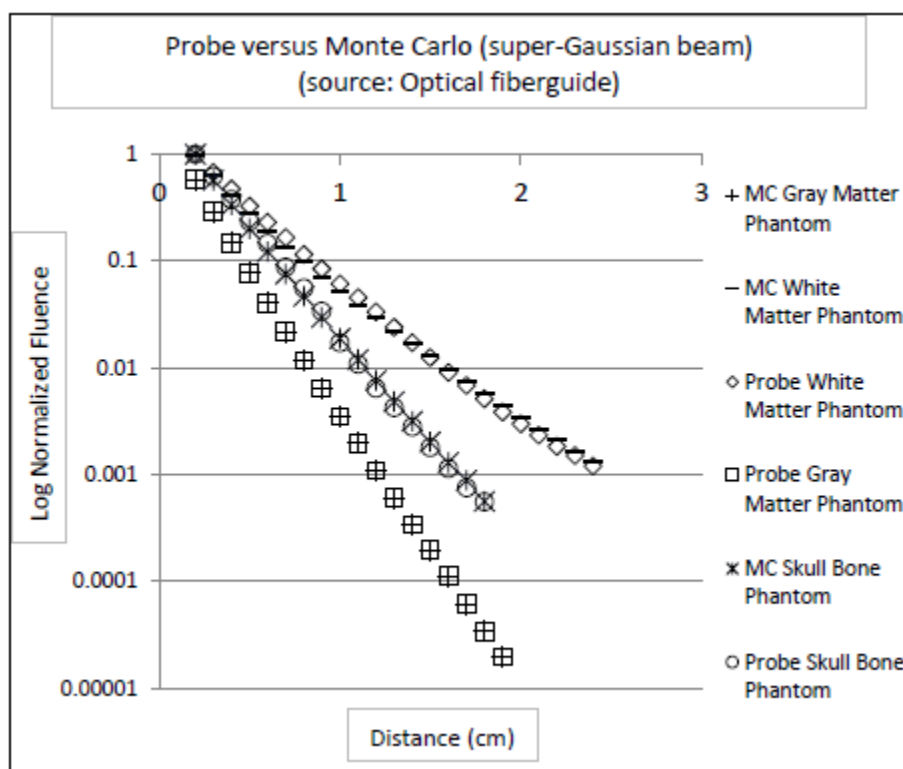
Figure 4.6 Optical dosimetry in white matter, gray matter and skull bone phantoms. The photon source used is an optical fiberguide (connected to a pulsating laser source) with a super-Gaussian beam distribution. The Monte Carlo generated fluence closely matches the fluence measured by the probe. This shows that the Monte Carlo beam modeling can be reliably used as a reliable estimator of photon energy distribution in tissue phantoms.
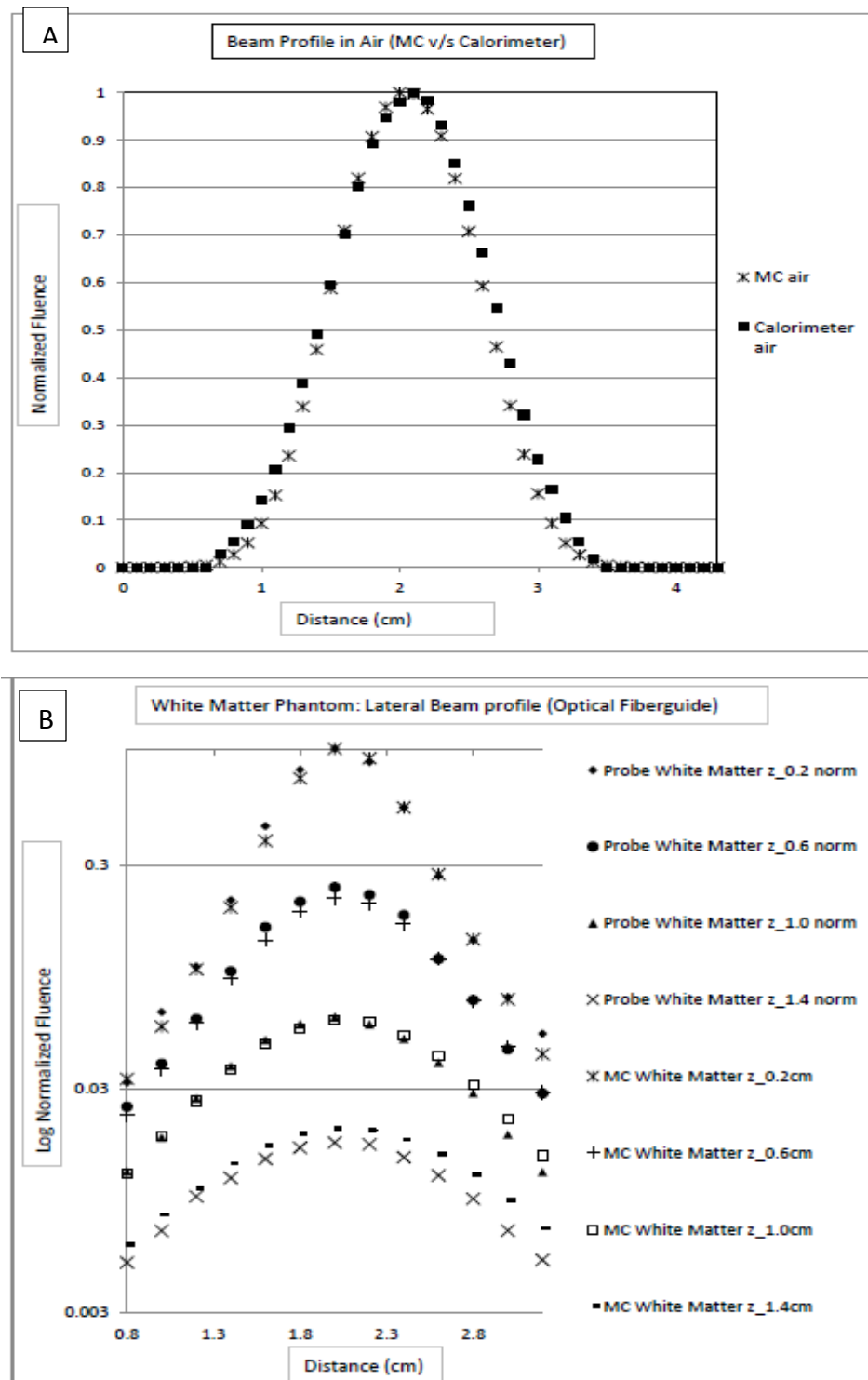
Figure 4.7 Lateral beam profile measurement using optical dosimetry probe and validation by Monte Carlo in homogeneous phantoms. (A) Beam profile in air using calorimeter. Optical dosimetry measurements validated MC simulated lateral beam profiles in phantoms of: (B) white matter, (C) gray matter and (D) skull bone, i.e., perpendicular to the beam axis. The measurements were normalized along the illumination axis. Cuvette dimensions: 5.3cm x 4.6cm x 3.1cm, thickness = 0.4cm.
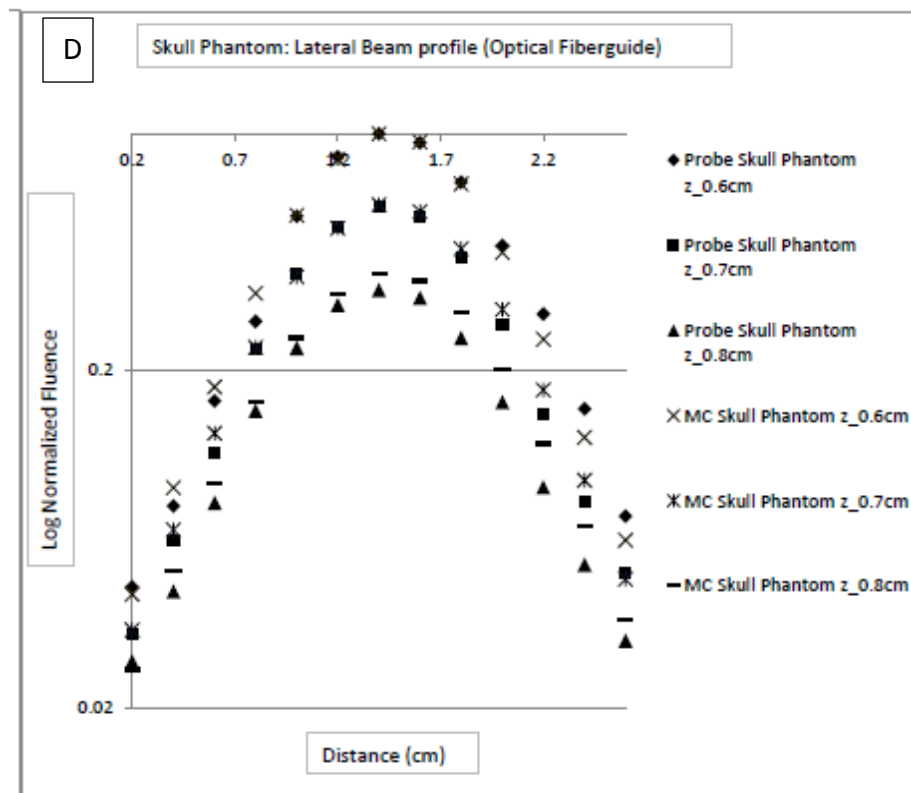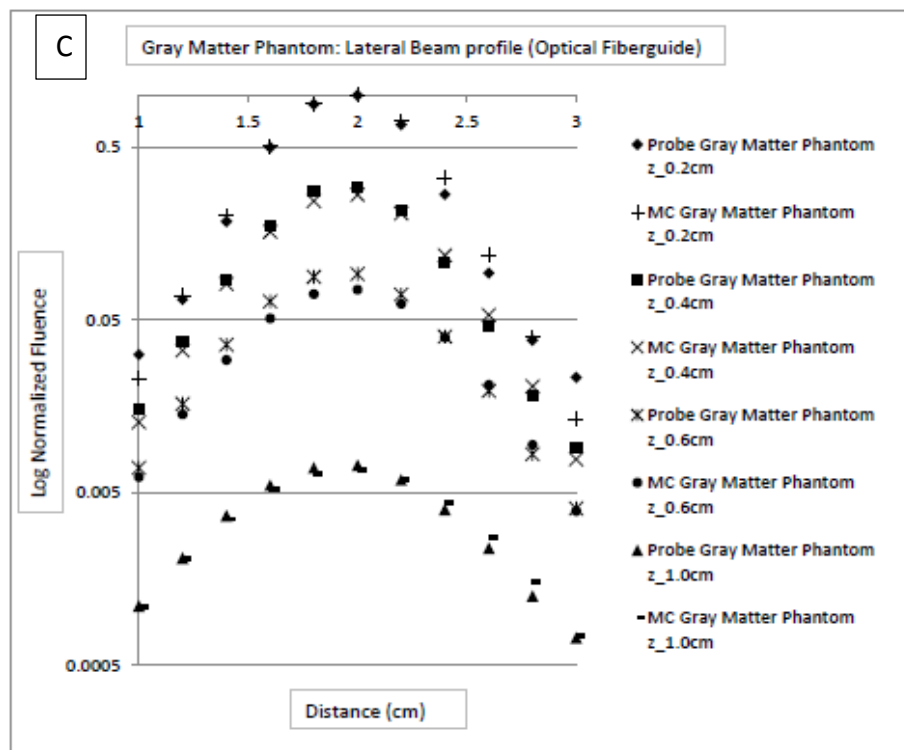
Figure 4.8 Continued

The average relative % error of the Monte Carlo relative to the probe measurements is 11.27% for white matter, 13.25% for gray matter and 11.81% for skull bone along the beam axis for a range of 0.2-2cm within the phantom, while perpendicular to the beam axis, the % relative error is 9.4%, 12.06%, and 8.91% for white matter, gray matter and skull bone phantoms. These systematic errors represent the levels of confidence with which the Monte Carlo matches the probe measurements, see tables 4.3 and 4.4.

Table 4.3 % Mismatch Error in Homogeneous Phantom along beam axis (z)

Phantom	Error% (0.2-1 cm)	Error% (1-2 cm)	Average error%
White Matter	12.13	10.5	11.27
Gray Matter	13.39	30.12	13.25
Skull Bone	11.39	12.28	11.81

Table 4.4 % Mismatch Error in Homogeneous Phantom perpendicular to beam axis (z)

Phantom	Error% z=0.2cm	Error% z=0.6cm	Error% z=1.0cm	Error% z=1.4cm	Average error%
White Matter	10.34	13.34	9.14	4.79	9.4
Phantom	Error% z=0.2cm	Error% z=0.4cm	Error% z=0.6cm	Error% z=1cm	Average error%
Gray Matter	13.45	11.52	14.29	8.97	12.06
Phantom	Error% z=0.6cm	Error% z=0.7cm	Error% z=0.8cm		Average error%
Skull Bone	8.41	5.69	12.64		8.91

An analysis of the fluence profile within the skull phantom showed that the super-Gaussian beam fluence decreases with an effective attenuation coefficient of 4.818cm^{-1}. This factor was used to estimate the effectiveness of therapy for different skull thicknesses. Based on the validated Monte Carlo method, the power transmitted by the fiberguide source for various skull thicknesses are 5.9mW/cm^2 (0.4cm thick), 2.16mW/cm^2 (0.6cm thick), 0.83mW/cm^2 (0.8cm thick), 0.33mW/cm^2 (1cm thick). Thus, the % power transmitted in a 1cm thick adult skull is 1.8%, while a pediatric skull of 0.4cm thickness would allow 33.5% optical power to reach the soft tissue. The thickness

of the skull and its density determines the overall attenuation and hence optical

planning protocols which can be obtain from a CT scan (see chapter 6).

4.3.2   Optical Dosimetry and Monte Carlo Validation in Heterogeneous Brain Phantoms

Fluence profiles measured in the white matter solution in the layered heterogeneous

phantom (1.1 cm skull agar phantom, 1.1 cm gray matter agar phantom, 5.9 cm white

matter liquid phantom in the said order), showed a good degree of match between the

Monte Carlo simulated data and the probe measurements, see figure 4.8. The

exponential decrease in fluence along the beam axis is shown on the right side of figure

4.8 while the lateral beam profiles at different depths above the gray matter agar

surface is shown on the left side of this figure. The lateral fluence profiles have been

normalized to the intensity at a depth of 0.2cm above the gray matter agar surface,

while the fluence profiles along the beam axis were normalized to the fluence at z =

0.1cm above the gray matter agar surface. The average systematic error (relative %

error) between the probe and Monte Carlo fluences is 17.71% along beam axis and

18.04% perpendicular to the beam axis and is shown in tables 4.5 and 4.6. The validation

of optical dosimetry results in the complex layered phantom validate that the beam

spread can be estimated correctly by the Monte Carlo if the optical coefficients of the

phantom are known.
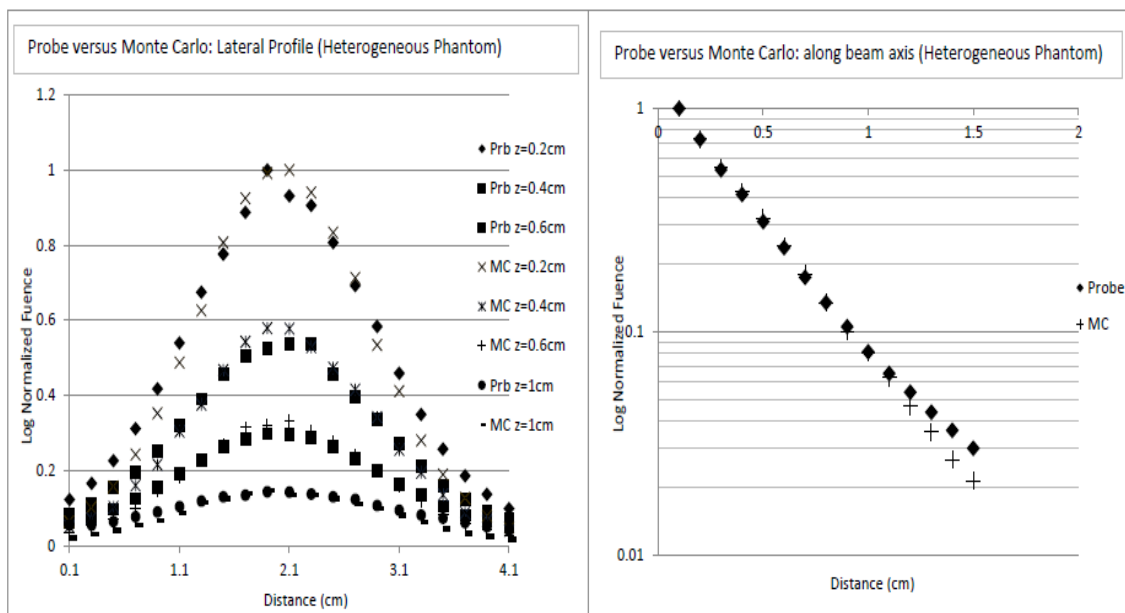
Figure 4.9 Validation of Monte Carlo in a heterogeneous phantom (1.1cm skull agar, 1.1cm gray matter agar and 5.9cm white matter liquid). Lateral profile measurements (in the white matter phantom solution) are shown on the left while axial comparison is on the right. The depth shown by z is the distance from the gray matter agar surface. Cuvette dimensions: 9.4cm x 9.4cm x 10.9cm, thickness = 0.3cm.

Table 4.5 % Mismatch Error in Heterogeneous Phantom along beam axis (z)

Phantom	Error% (0.1-1 cm)	Error% (1-2 cm)	Average error%
White Matter (over Skull and Gray Matter layers)	2.11	33.32	17.71

Table 4.6 % Mismatch Error in Heterogeneous Phantom perpendicular to beam axis (z)

Phantom	Error% z=0.2cm	Error% z=0.4cm	Error% z=0.6cm	Error% z=1cm	Average error%
White Matter (over Skull and Gray Matter layers)	18.52	15.09	15.37	23.17	18.04

4.4   Discussion

We validated the 3D Monte Carlo code using the TiO_2 based dosimetry probe

measurements in phantoms resembling white matter, gray matter and skull bone. When

comparing absolute fluence measurements, the error between MC simulated data and

measured data was less than 25 percent within these homogeneous tissues. The

independent characterization of the probes and the optical phantoms using calorimeter

gold standard and spectrophotometer demonstrated the validity of using the probe as a

gold standard. Studies were performed for two different types of NIR light sources in

different optical phantoms, and the ease of photon quantification to absolute dose (in

mW/mm^2 or J/mm^2) proves the fidelity of the Monte Carlo as a predictive tool to

accurately estimate 3D photon energy distribution in complex media. The measurement

and prediction accuracy can be improved with better instrumentation for probe

localization and better laser beam positioning setups. The boundary conditions of the

phantom play a very important role in the Monte Carlo results and need to be simulated

accurately. This includes the accurate depiction of cuvette/phantom dimensions,

distance from the source and source dimensions.

This study achieves the first step of designing the tools necessary to validate the NIR

photon distribution in three dimensions in optical phantoms. By quantifying the energy

fluence and local deposited dose will allow an accurate depiction of the rate and

quantity of drug release. Critical to these simulations is the accurate determination of

the tissue structure and boundaries, which can be determined using imaging modalities

such as MRI or CT scan to segment various tissue types and obtain an optical property

map. This can now be seamlessly input into the Monte Carlo under various illumination

conditions.

5   SPECIFIC AIM3: EMPIRICAL APPROACH TO PHOTON PROPAGATION

5.1   Introduction

Translating an optical planning tool into the clinic requires simulations to be performed

in time frames that are feasible. Monte Carlo simulations takes a few hours of execution

time to generate statistically significant number of photons for full brain, and this is for a

single laser source. Obtaining an optimal optical treatment plan requires dose

calculations for multiple laser sources and iterations to ensure maximal light delivery to

the target tissues. Hence, even though the CUDA based platform enhances the speed of

the Monte Carlo by 300X over CPU based models [61], it still would need to be

significantly accelerated to be provide treatment plans in a clinical setting. This can be

accomplished by purchasing a cluster of NVIDEA cards (costly). Instead, this motivated

us to design an empirical model approach to estimate photon propagation in complex

heterogeneous tissues, which could have a runtime of less than a minute while

providing a *reasonable* level of accuracy [64].

A number of analytical solutions are made to the radiative transport equation, also

known as the Boltzmann transport equation [82]:

$$\Omega.\nabla\psi(r,\Omega) + \big(\mu_a(r) + \mu_s(r)\big)\psi(r,\Omega) = S(r,\Omega) + \mu_s(r)\int_{4\pi}\psi(r,\Omega')\,p(\Omega,\Omega')d\Omega' \quad (5.1)$$

In the above equation, $S(r, \Omega)$ is source term and describes the power injected into a

solid angle defined by Ω within a unit volume at position $\mathbf{r}$; Ω is the photon propagation

unit vector; $\psi(r, \Omega)$ is the radiance energy (units: $W.cm^{-2}.sr^{-1}$); $\mathbf{r}$ is position vector;

$p(\Omega, \Omega')$ is the phase function and represents the probability of photon scattered from

direction Ω' to Ω.

The fluence, $\Phi(r)$, is obtained by summing the energy radiance, $\psi(r, \Omega)$, over all

directions [82]:

$$\Phi(r) = \int_{4\pi} \psi(r, \Omega) d\Omega . \quad (5.2)$$

Solving the radiative transport equation can be solved using finite difference methods

under certain approximations [82]. One such method is the DANTSYS (diffusion

accelerated neutral particle transport code system) [82].

The diffusion approximation (P1 approximation) is the most commonly used analytical

approximation to the radiation and is used widely to calculate fluence in homogeneous

and heterogeneous tissues and is given by the equation [82, 83]:

$$\frac{1}{c}\frac{\delta\Phi(r,t)}{\delta t} + \mu_a\Phi(r,t) - \nabla.[D\nabla\Phi(r,t)] = S(r,t). \quad (5.3)$$

The diffusion equation can thus be used to derive the optical fluence in homogeneous

and heterogeneous tissues by using diffusion synthetic acceleration method (DANTSYS)

and employs a corrected diffusion equation to accelerate the convergence of transport iterations. The use of the diffusion equation results in under-estimation of fluence in media with a high ratio of absorption to scattering coefficients [82, 84]. The Monte Carlo method thus remains the only method to accurately simulate photon fluence over a wide range of albedos.

In our study, we investigated a voxel-based, nearest neighbor weight based method trained using Monte Carlo simulated data. In retrospect, this approach is similar to the photon convolution method [85], but uses arbitrary weights to determine photon scatter at each location (voxel) in a 3D volume. The absorption of photons in each voxel is determined using the Beer Lambert's law [78] and the optical absorption coefficient. The photon dose distribution is simulated in a 3D voxelated format for easy comparison and 3D optimization with the Monte Carlo and allows seamless integration with medical imaging modalities such CT and MR, used to characterize tissue heterogeneity and object boundaries of the medium. The empirical nature of this software can be easily adapted to different optical properties and voxel sizes by adjusting the scattering weights, while the absorption coefficient remains unchanged. As with the MC code, different beam profiles and upstream optics can be seamlessly integrated to improve its applicability. Realization into CUDA can provide corrective algorithms on the order of a few seconds and real-time applications.

5.2   Materials and Methods

5.2.1   Algorithm Design

The Empirical approach is based on the assumption that the photon fluence in a voxel in

a particular layer is a weighted sum of the fluences of neighboring voxels in the previous

layer [63, 64]. The basic concept and schematic of this algorithm is illustrated in figures

5.1-5.3. The steps of the algorithm can be summarized as follows:

1. Assign the incident photon beam distribution (e.g. super-Gaussian beam) to the first

    layer of voxels. In this case, we assume that the direction of photon propagation is in

    the +z direction.

2. For every voxel in a layer, calculate the directional scatter components. The

    equation 8 represents an example of how the forward scatter component is

    calculated. The coordinates i, j, k denote the x, y and z location of the voxel. The

    arbitrary weights wt1 and wt2 are forward and diagonal weights, which determine

    the percentage of scatter. The sum of all weights is always equal to one (i.e.

    $wt_1+4*wt_2=1$), so that the total fluence entering a voxel is equal to the sum of

    fluence absorbed and exiting the voxel. The equations used to calculate the other

    components can be similarly determined. The sum of all the scatter components in a

    voxel equals the total fluence in that voxel (arbitrary units: photons/unit volume).

3. Calculate absorbed energy (I_{abs}) using Beer Lambert's law for a path length dl = voxel

    length, based on the absorption coefficient (μ_a) of the voxel:

$$I_{abs}(i, j, k) = I(i, j, k)(1 - e^{-\mu_a dl})   (5.4)$$

4. Calculate and accumulate the fluence over all voxels in the current layer and

increment z to proceed to the next layer. Continue propagation till the fluence exits

the volume.

An example of the implementation of this algorithm in 3D matrices using nested "for

loops" is shown in figure 5.3 (A). The purpose of this flowchart is to explain the details of

the algorithm from the perspective of its implementation. Different iterating loops and

several different data structures are possible to implement this algorithm based on the

memory and performance requirements.

We implemented an iterative routine, shown in figure 5.3 (B), in order to ensure that

residual fluences exit the 3D volume. The rationale behind this step is that some side-

scatter and back-scatter components are significantly high in media with high scattering

coefficients (e.g. white matter). While the software is implemented in the form of a

primarily forward propagation direction, it leaves behind residual fluence components

which do not contribute to the total fluence and which do not exit the volume. Thus in

order to ensure that all residual photons leave the volume, we implemented an iterative

routine to propagate photons in the forward (+z) and reverse (-z) directions alternatively.

This was implemented in an iterative fashion. In the first iteration we propagate the

photons in the +z direction while in the next iteration the matrices are flipped (along the

x, y, z planes) such that +z direction now refers to the –z, +x refers to the –y and +x

refers to the –x directions. In other words the matrix is turned upside down. The

empirical code is run again (without any additional input fluence) such that the iteration is mainly in a direction opposite to the first iteration. We again flip the matrix to its original orientation before running the empirical iteration. This is continued until we ensure that most photons have exited the volume and the residual fluences are below a certain threshold. In our study we found that 14 iterations were sufficient to ensure that most photons have exited the volume. It is important to note that the iterative routine mainly ensures a better match with Monte Carlo in the lateral direction (in xy plane) away from the beam axis. The number of iterations has less effect on effective attenuation at the center of the beam where most of the fluence is contributed to by the forward directional fluence vector.
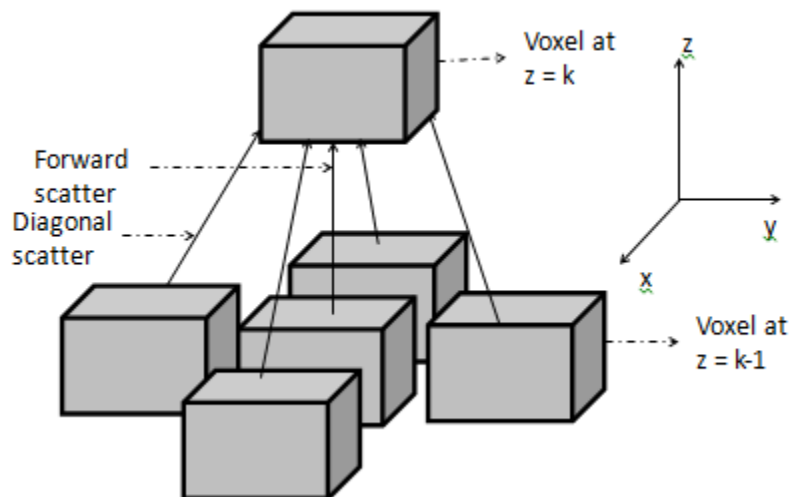
Figure 5.1 The Empirical photon propagation [64]: The photons in a voxel is propagated to neighboring voxels using scatter weights.
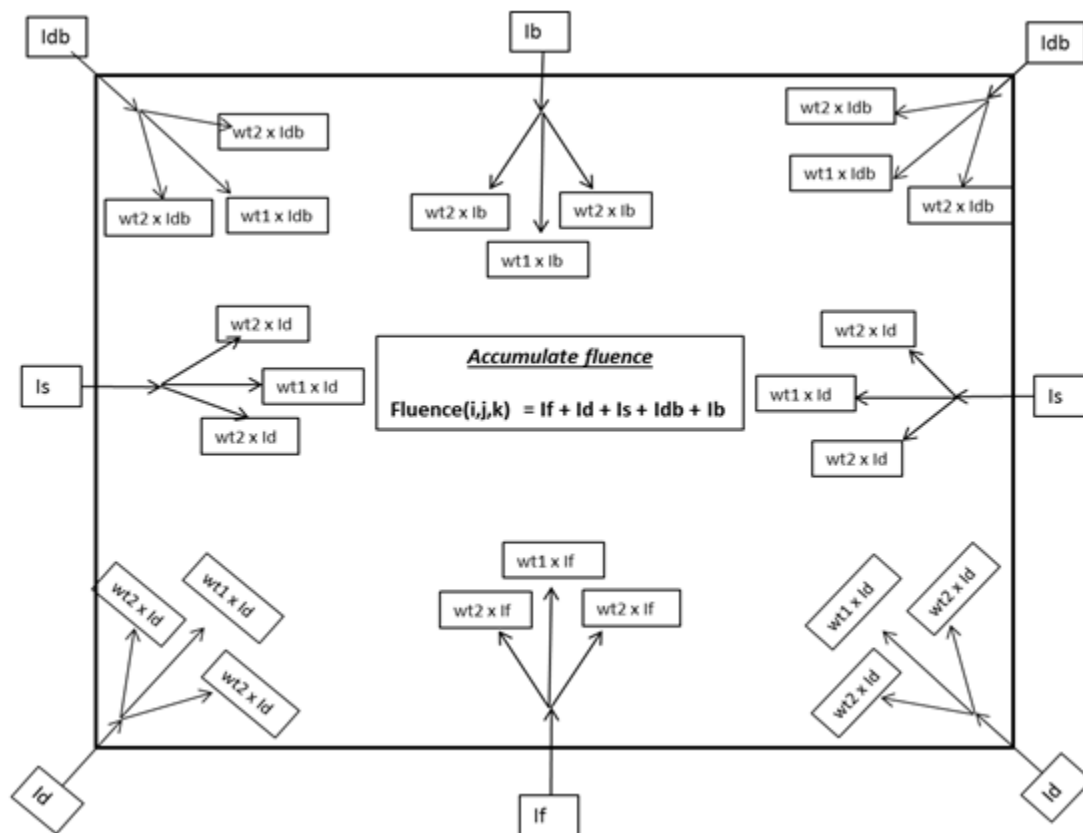
Figure 5.2 Integral or accumulation of fluence in a voxel. [64]. The dorectioonal fluences such as forward (If), diagonal upwards (Id), diagonal downwards (Idb) and side (Is), eneterig a voxel are weighted and summed using forward (wt1) and diagonal weights (wt2). Fluence is redistribution conserved by ensuring that (wt1 + 4 x wt2) = 1.
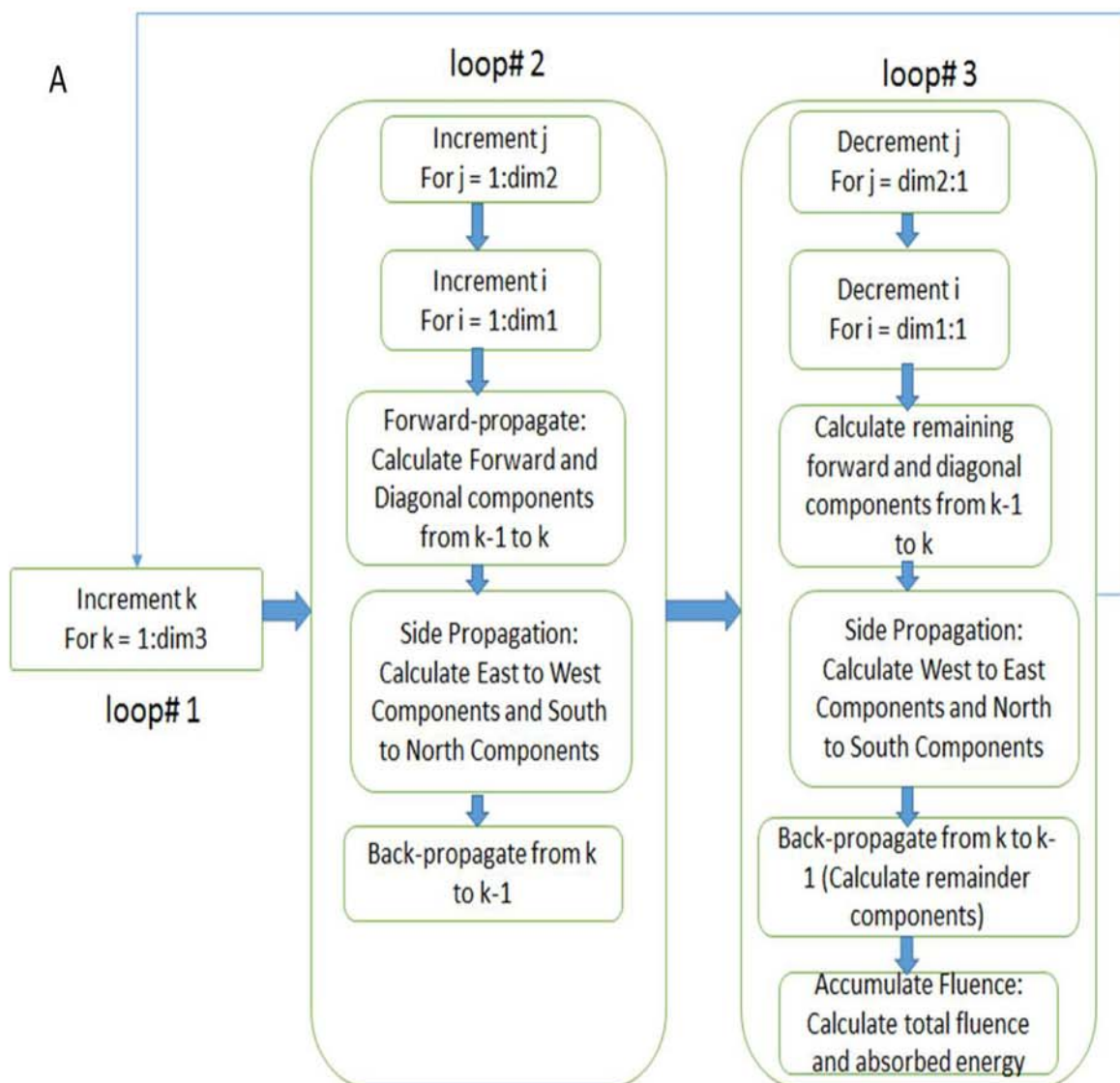
Figure 5.3 A)Implementation of the 3D Empirical algorithm using nested loops. Photons are propagated in the simulation by iterating over a 3D matrix. The matrix dimensions in the x, y, z coordinates are dim1, dim2 and dim3 respectively, while (i, j, k) are (x, y, z) coordinates of a voxel in the volume. B) Iterative routine to run the Empirical algorithm. In each iteration we check if the sum of the residual fluences are below a certain threshold. If the residual fluences are still high, we run the empirical code iteratively to ensure that the residual fluences have exited the volume. In our study we use 14 iterations for the neonatal head simulations, while 1 iteration is sufficient for homogeneous phantoms. The iterative routine is seen to be more effective for highly scattering tissues with a significant amount of back-scatter.
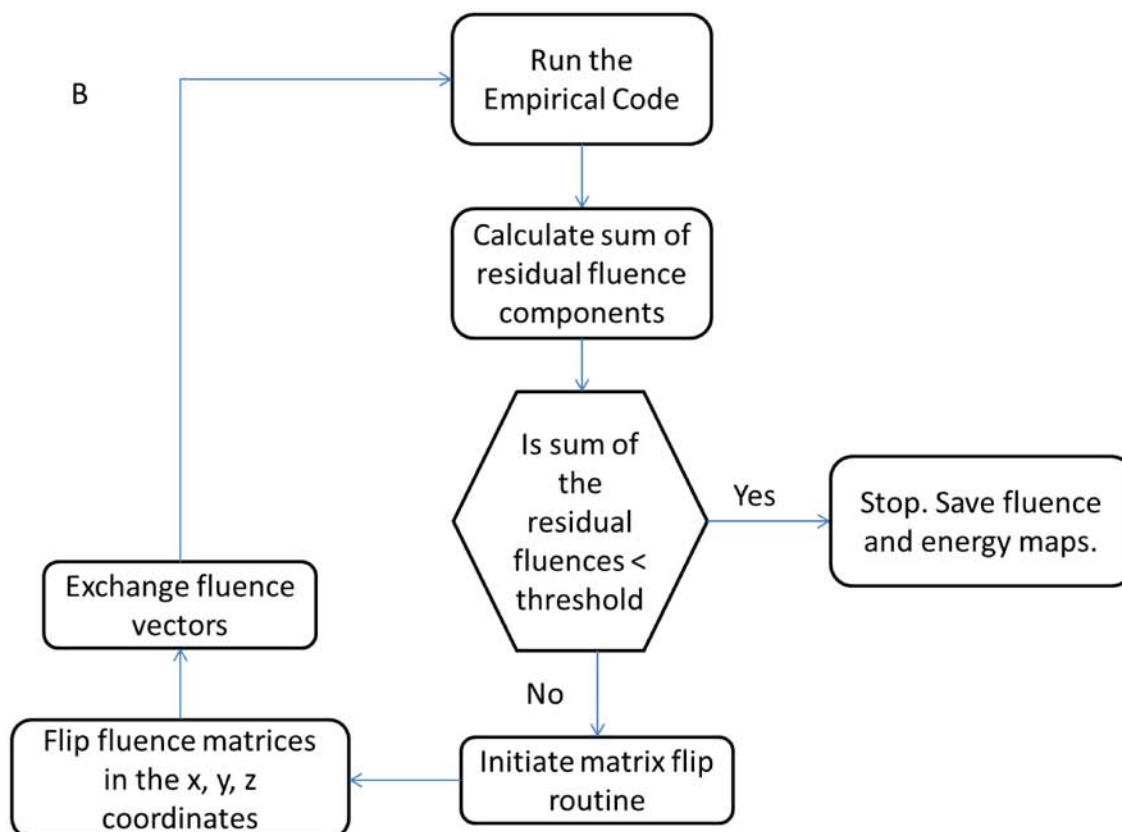
Figure 5.4 Continued

5.2.2 Optimization of the Empirical Algorithm using Monte Carlo

The GPU based Monte Carlo was used to derive the weights, which depended upon the

reduced scattering coefficient of the medium. The weights were obtained by an iterative

optimization procedure that compared the output fluence of the empirical algorithm to

that generated by the Monte Carlo the fluence along the central beam axis. The weights

which show the best possible match defined by the highest R-square coefficient are

selected to calibrate the empirical method. Tables 5.1 and 5.2 show the weights (wt_1

and wt_2) obtained for different tissue types and voxel sizes. The absorption coefficient is

scaled to the voxel size and the photons are absorbed before proceeding to the next

layer.

5.3   Results

5.3.1   Empirical Optimization results

In this section we describe the optimization studies performed on the Empirical

algorithm. Both these studies were performed separately for brain tissues and tissue

phantoms, mainly due to the difference in their optical anisotropy factors, which leads

to subtle changes in fluence distributions. Table 5.1 shows the weights derived for brain

tissue phantoms (composed of India ink and Intralipid), while table 5.2 shows the

weights for real brain tissues. The optical properties of brain tissues are shown in table

4.1 while those of the tissue phantoms are shown in table 4.2. The corresponding

comparison in fluence profiles along the beam axis is shown by figure 5.4 for brain tissue

phantoms and by figure 5.5 for real brain tissues. The difference in the properties mainly

arises from the difference in the anisotropy factor between intralipid and the brain

tissues. Thus while we have achieved a match in the reduced scattering coefficient

between the phantoms and the real tissues, the photon distribution varies to some

extent between tissues and phantoms, as seen by Monte Carlo simulations. Hence we

trained the Empirical algorithm to match the match the Monte Carlo generated fluence

separately for both brain tissues and tissue phantoms. The different resultant weights

derived between phantoms and tissues also validates the purpose.

We also did a comparison of lateral fluence profiles generated by the Monte Carlo and the Empirical and these are shown in figures 5.6 -5.9. While the optimization routine used the match in fluence attenuation along the beam axis as the main criteria, we tried to see if this translates into a match along the lateral direction at different depths (z=2mm, z=5mm, z=10mm, z=15mm) in homogeneous tissues. Our analysis shows that the lateral profiles of the Empirical algorithm closely match those of the Monte Carlo under similar illumination and boundary conditions.

Table 5.1 Weights derived for Brain Tissue Phantoms [63]

Tissue Phantom	Voxel Size (mm)	Wt1	Wt2	R-square
White Matter	0.1	0.949461	0.012635	0. 99999
Gray Matter	0.1	0.87469	0.031328	0. 999969
Skull Bone	0.1	0.914828	0.021293	0. 99979
White Matter	1	0.474876	0.131281	0. 99992
Gray Matter	1	0.062097	0.234476	0.999828
Skull Bone	1	0.245949	0.188513	0. 999871
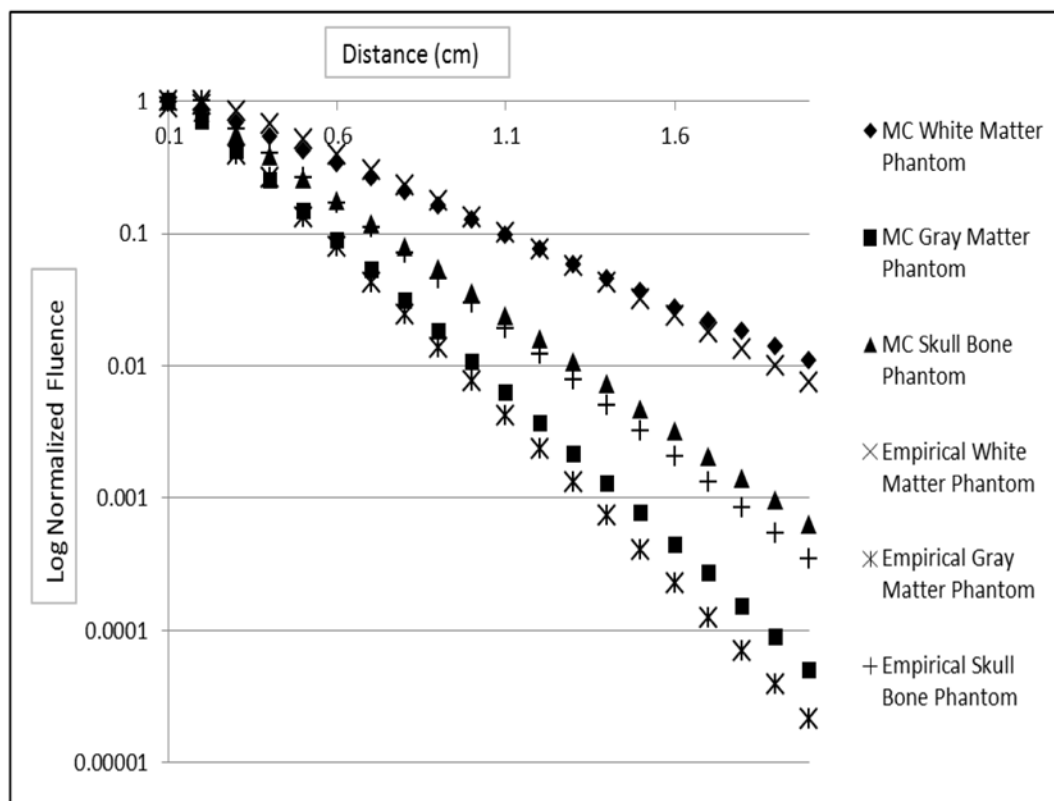
Figure 5.5 Optimization phase for Brain Tissue Phantoms. The optical properties of phantom materials (India ink and Intralipid) from table 4.2, are used by the MC. A flat broad beam (2cm diameter) is simulated using Monte Carlo and the Empirical algorithm is optimized to match the Monte Carlo with the identical illumination conditions [63].

Table 5.2 Weights derived for Brain Tissues

Tissue Phantom	Voxel Size (mm)	Wt1	Wt2	R-square
White Matter	0.1	0.931723	0.017069	0.999985
Gray Matter	0.1	0.904809	0.023798	0.999976
Skull Bone	0.1	0.931898	0.017025	0.999985
Tumor (Astrocytoma)	0.1	0.954234	0.011442	0.999991
White Matter	1	0.292641	0.17684	0.999898
Gray Matter	1	0.115763	0.221059	0.99984
Skull Bone	1	0.306998	0.173251	0.999885
Tumor (Astrocytoma)	1	0.51633	0.120917	0.999896
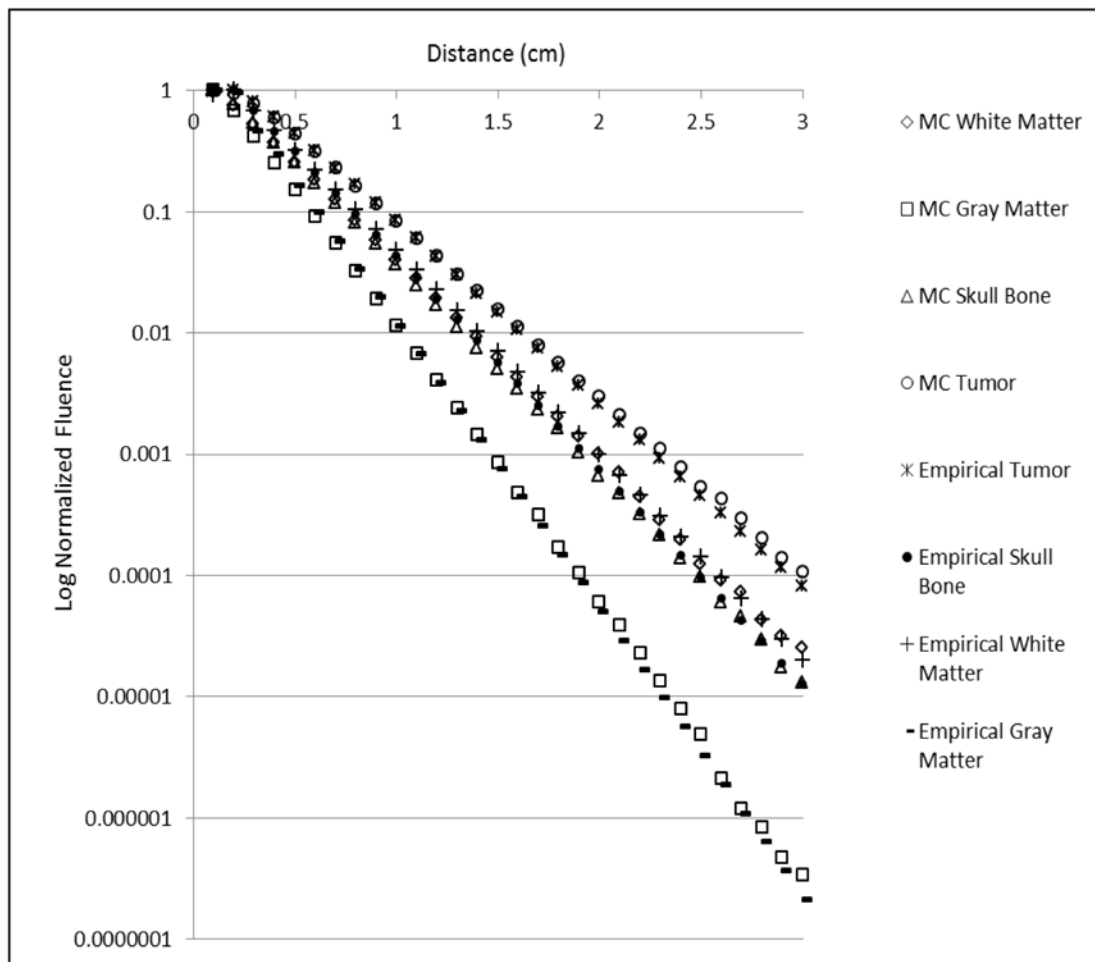
Figure 5.6 Optimization phase for Brain Tissues. The brain tissue properties from table 4.1 are used by the Monte Carlo. A flat broad beam (2cm diameter) is simulated using Monte Carlo and the Empirical algorithm is optimized to match the Monte Carlo with the identical illumination conditions.
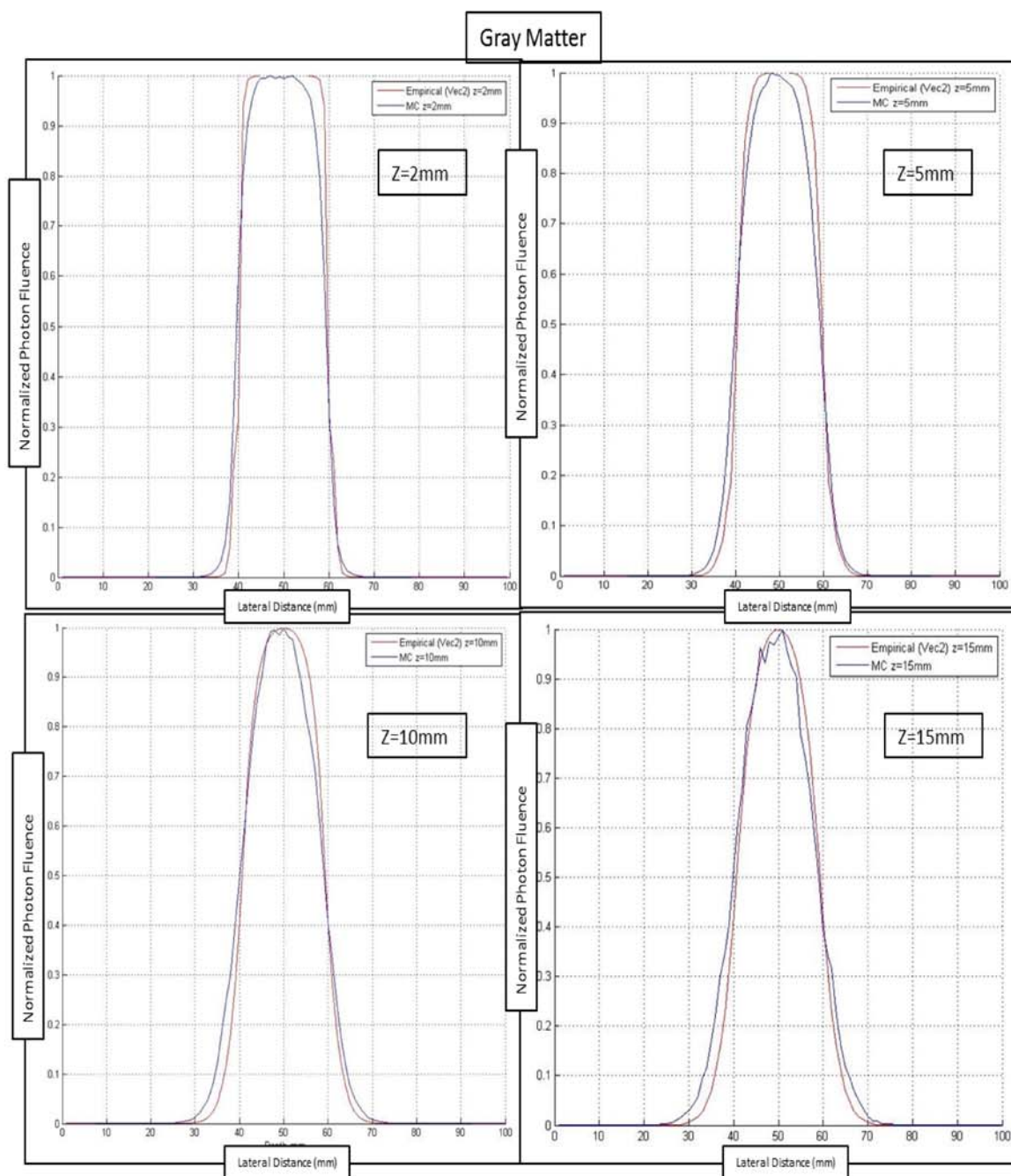
Figure 5.7 Lateral Beam profile comparison between Empirical and Monte Carlo for Gray Matter tissue. A flat broad beam (2cm diameter) is simulated.
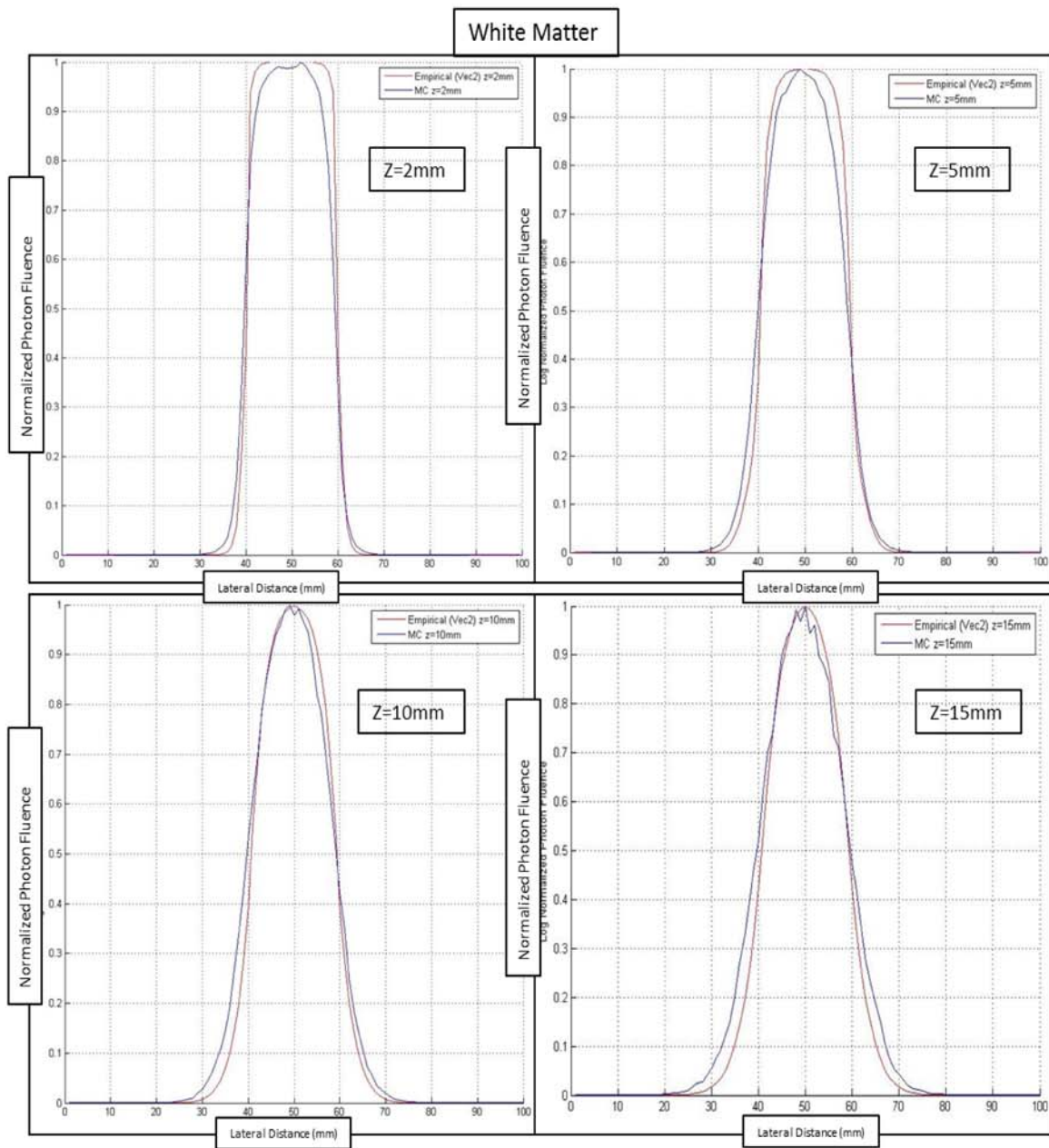
Figure 5.8 Lateral Beam profile comparison between Empirical and Monte Carlo for White Matter tissue. A flat broad beam (2cm diameter) is simulated.
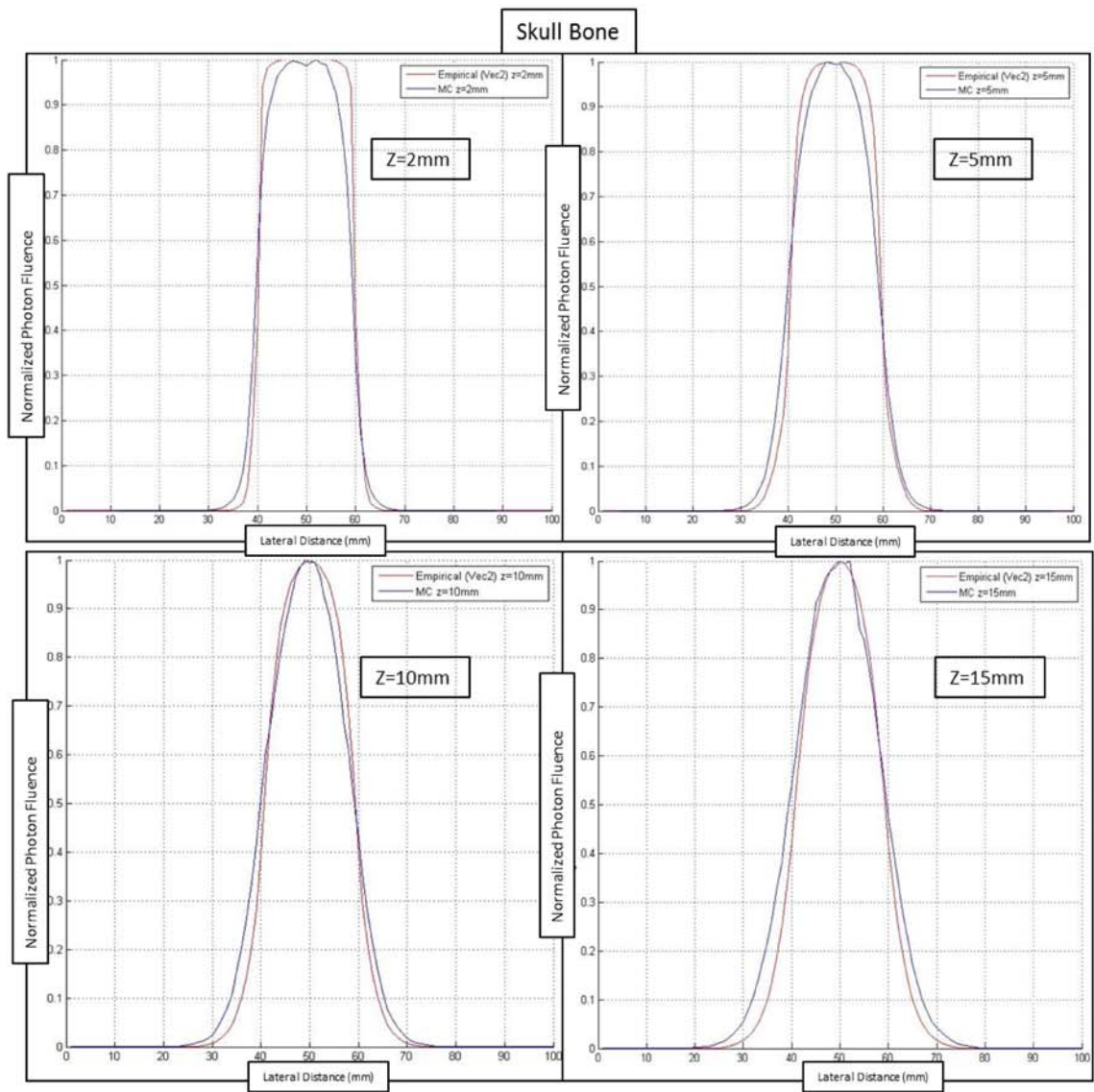
Figure 5.9 Lateral Beam profile comparison between Empirical and Monte Carlo for Skull Bone tissue. A flat broad beam (2cm diameter) is simulated.
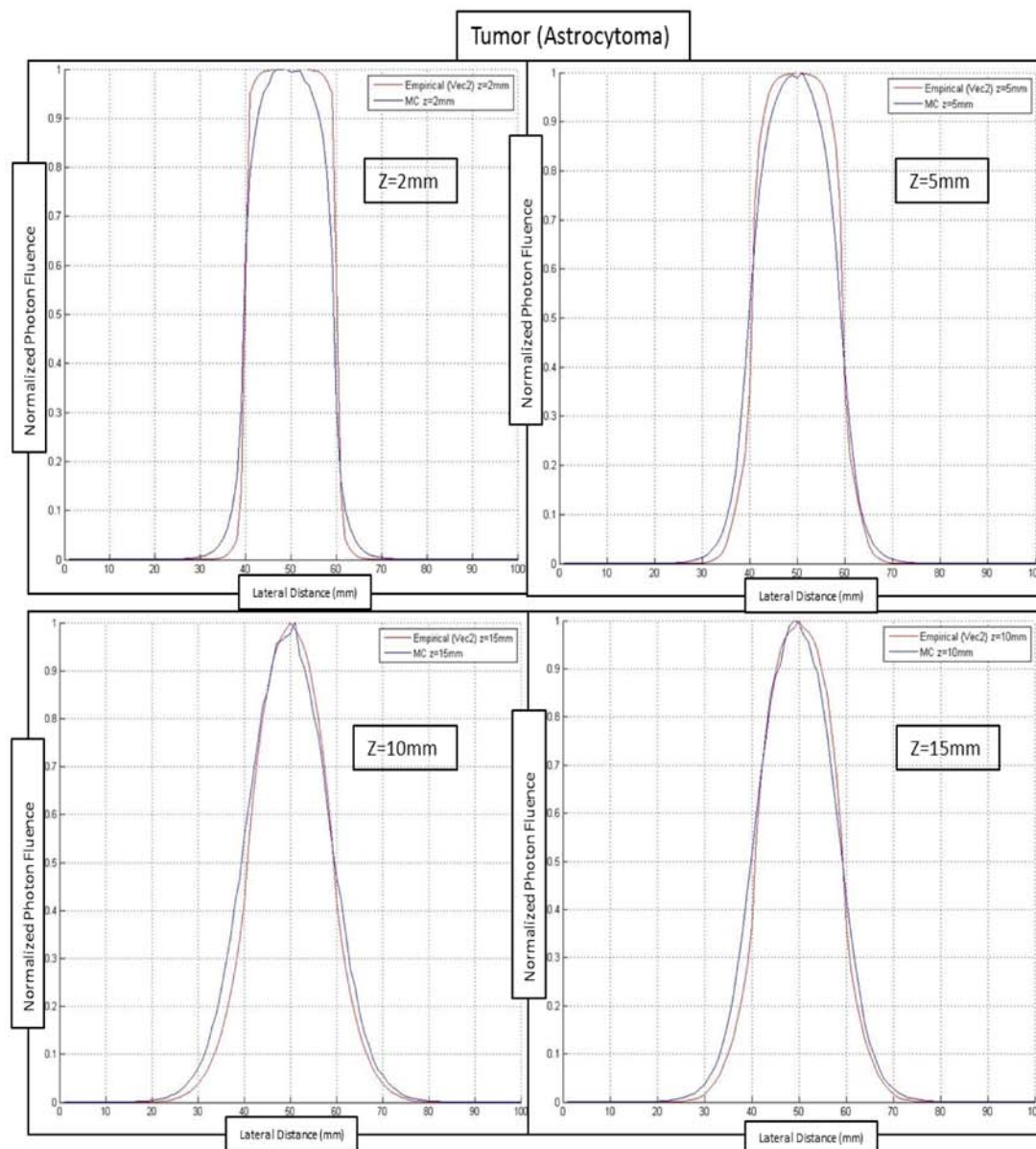
Figure 5.10 Lateral Beam profile comparison between Empirical and Monte Carlo for Astrocytoma Tumor tissue. A flat broad beam (2cm diameter) is simulated.

5.3.2 Empirical Validation using Dosimetry Probe

The Empirical algorithm was compared to Monte Carlo simulate data and probe measurements in homogeneous phantoms with known optical properties to validate the Empirical code for super-Gaussian beam profile.

Figure 5.10 shows the comparison between the Monte Carlo, Empirical and Probe

measurements in brain tissues for broad beam simulations in homogeneous phantoms.

The weights derived for tissue phantoms are different from tissues. For the tissue

phantoms, the weights used are from table 5.1. The beam simulated in a super-Gaussian

beam as described in chapter 4. The super-Gaussian beam can be easily simulated using

the Empirical as it allows us to set the photon distribution at any voxel. The average

relative % error between the Empirical and Probe measurements is 10.2% for White

Matter, 45.2% for Gray Matter and 22.1% for Skull Bone phantoms; while the

comparison between Empirical and MC is 22.6% for White Matter, 35.8% for Gray

Matter and 21.9% for Skull Bone phantoms. The probe measurements validate the

Empirical results and the Monte Carlo in homogeneous phantoms.
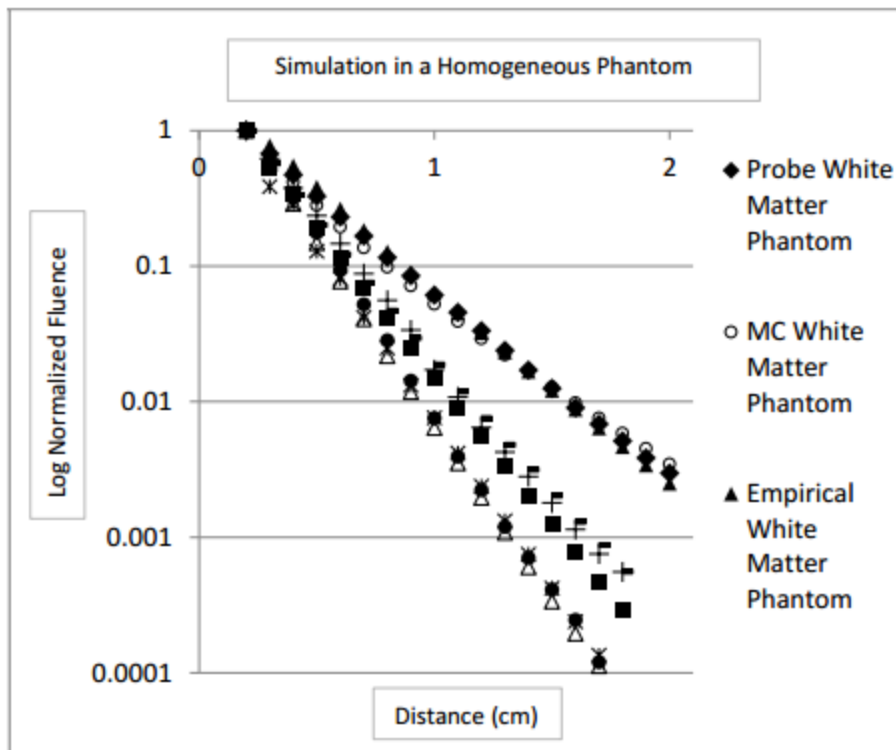
Figure 5.11 Comparison of the Empirical algorithm with Monte Carlo and Probe measured fluence in brain phantoms resembling white matter, gray matter and skull bone. The illumination source used is a super-Gaussian beam, which is emulated by the Monte Carlo and the Empirical algorithm. The empirical approach is a close approximation of the Monte Carlo and the probe over the range of optical properties of brain tissues. [63].

5.3.3 Simulations in Head Phantoms

We simulated head phantoms to compare the Monte Carlo and Empirical fluence and energy distributions. The phantom simulated had the dimensions of a child's head. The simulation studies were done in the presence (figures 5.11 - 5.14) and absence (figures 5.15 – 5.18) of tumor to study how well the Empirical photon distribution matches the Monte Carlo. 2D photon energy maps were also generated and compared. The weights used for the simulations were those of real brain tissues as shown in table 5.2. While the

Monte Carlo only generates the fluence map, the energy map is derived from the

fluence map by multiplying the fluence with the absorption coefficient and the volume

of the voxel.

In the case of the normal head phantom (without tumor) of 100mm diameter, the

boundary conditions and tissue dimensions are shown in figure 5.11. The skull thickness

is 4mm; thickness of gray matter is 10mm, while the center of the head is mainly white

matter with a diameter of 72mm. The phantom is illuminated with a 20mm diameter

uniform beam (800nm wavelength). Figure 5.12 shows the comparison plot of the

energy deposition between the Monte Carlo and the Empirical along the beam axis. The

first point on the plot starts at the point where the light enters the skull tissue (i.e.

depth=0 in the plot of figure 5.12 corresponds to z=6 along the beam axis in figure 5.11).

Similarly, figure 5.13 shows the log normalized fluence plot along the beam axis. Both

the fluence and the energy plots show that the Empirical fluence and energy simulated

closely follow those of the Monte Carlo within a certain error. The energy distribution

maps in 2D are shown in figure 5.14. Note that the Monte Carlo generated map suffers

from extremely low photon fluence at depths larger than 5cm due to low photon

statistics (restrained by the time for head simulations), while the Empirical algorithm

does not suffer from this limitation.

We also studied the performance of the Empirical algorithm in a head phantom in the

presence of a tumor (astrocytoma) of 5mm diameter. The boundary conditions of other

tissues are similar to those of the normal head phantom in the previous case and are

shown in figure 5.15. The tumor presence significantly changes the fluence and energy

distributions as shown in figure 5.16 and figure 5.17 respectively, compared to the

normal head. The fluence perturbation is mainly at the site of the astrocytoma which

shows higher energy absorption as shown in figure 5.16. The difference between the

fluences generated by the Empirical and the Monte Carlo has a certain difference, which

also translates into an error in the energy distributions. However as seen in the plots,

this error is constant and can be easily quantified. The photon energy maps are shown

in figure 5.18.

Figure 5.12 Simulation of a head phantom for comparing the Empirical and Monte Carlo
models in heterogeneous brain tissues.
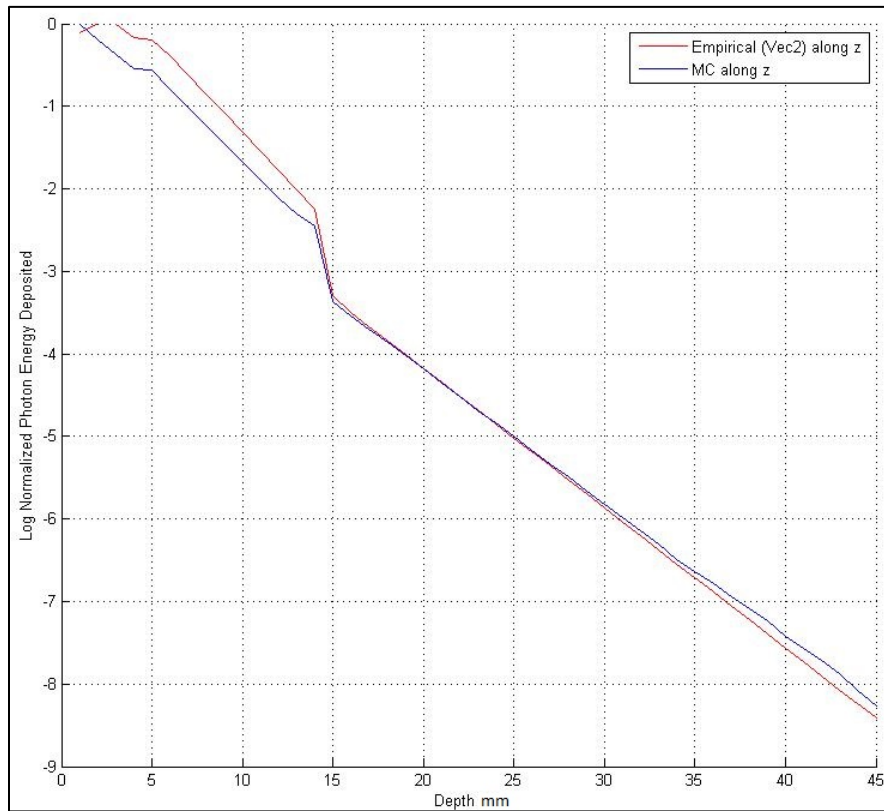
Figure 5.13 Comparison of photon energy distribution between the Empirical algorithm and Monte Carlo in a head phantom, along the beam axis. The illumination source used is a uniform beam of 2cm diameter. The plot is from the point where light enters the skull bone (refer to figure 5.11).
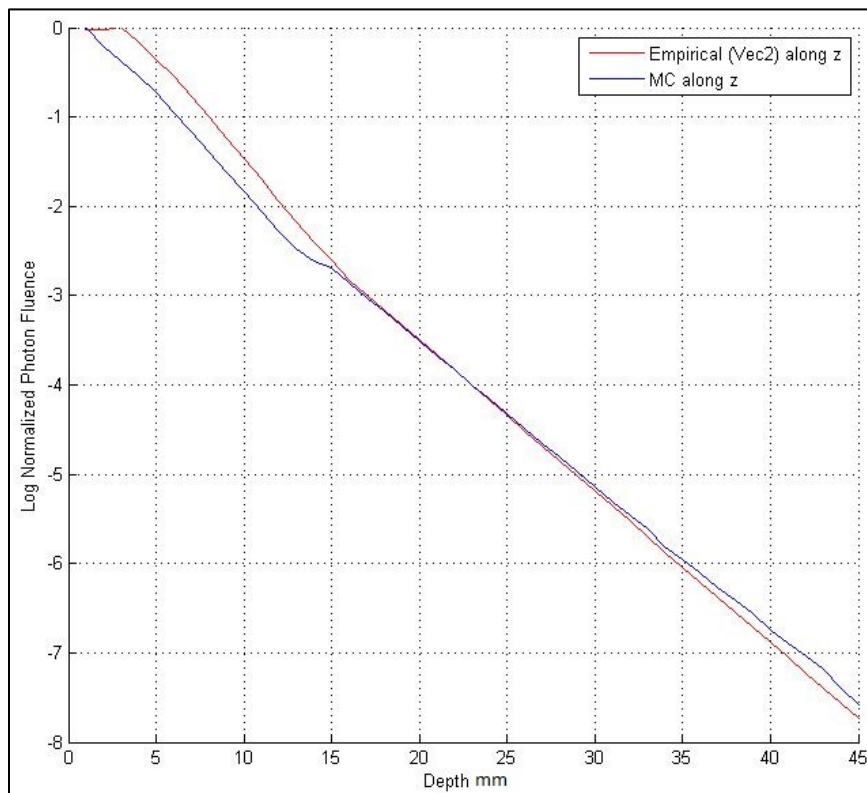
Figure 5.14 Comparison of photon fluence distribution between the Empirical algorithm and Monte Carlo in a head phantom, along the beam axis. The illumination source used is a uniform beam of 2cm diameter. The plot is from the point where light enters the skull bone (refer to figure 5.11).
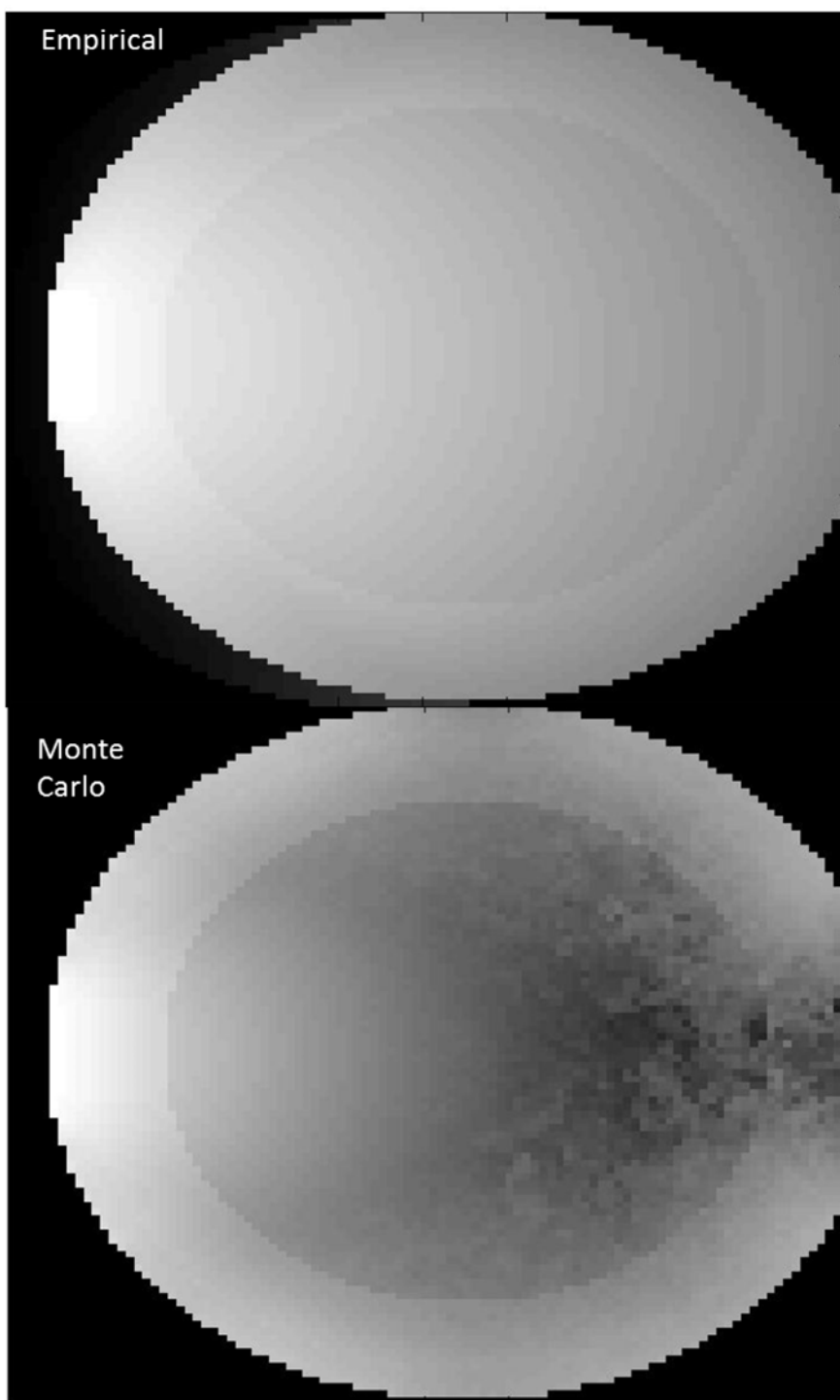
Figure 5.15 Comparison of photon energy distribution images (2D) between the Empirical algorithm and Monte Carlo in a normal head phanton.
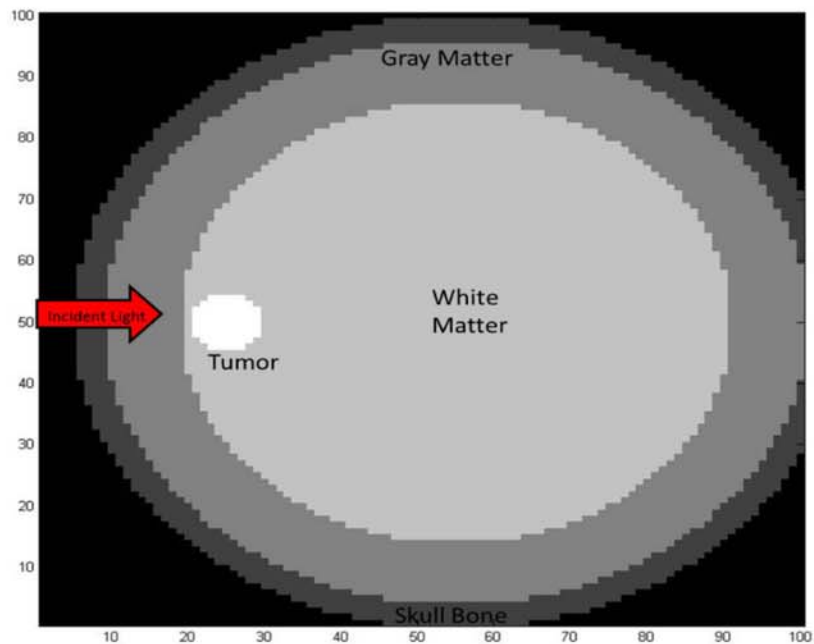
Figure 5.16 Simulation of a head phantom with tumor (astrocytoma) for comparing the Empirical and Monte Carlo models in heterogeneous brain tissues.
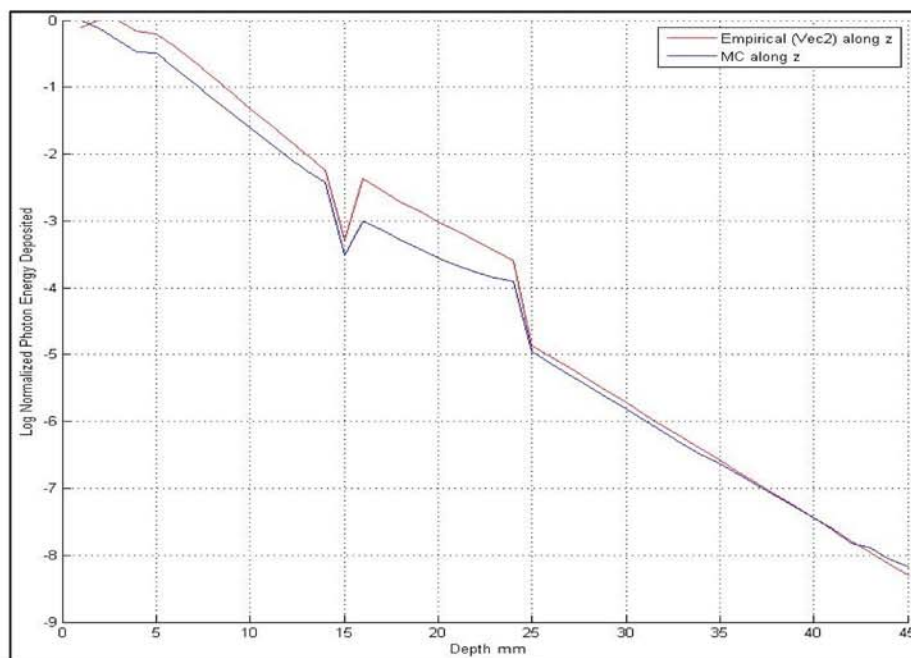
Figure 5.17 Comparison of photon energy distribution between the Empirical algorithm and Monte Carlo in a head phantom with tumor, along the beam axis. The illumination source used is a uniform beam of 2cm diameter. The plot is from the point where light enters the skull bone (refer to figure 5.15).
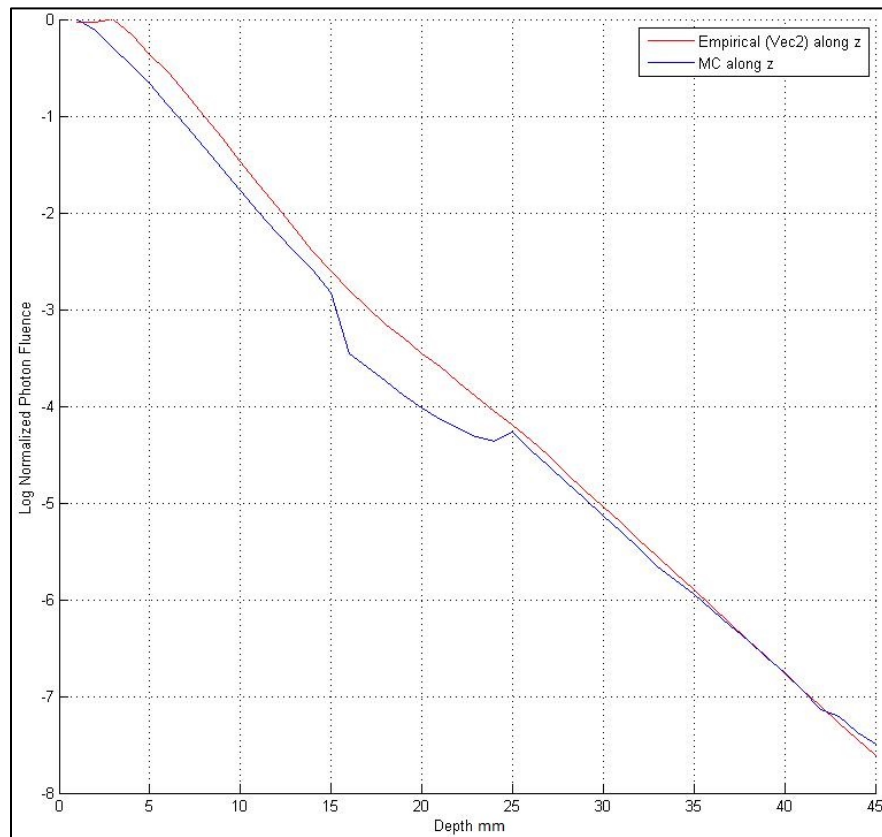
Figure 5.18 Comparison of photon fluence distribution between the Empirical algorithm and Monte Carlo in a head phantom with tumor, along the beam axis. The illumination source used is a uniform beam of 2cm diameter. The plot is from the point where light enters the skull bone (refer to figure 5.15).
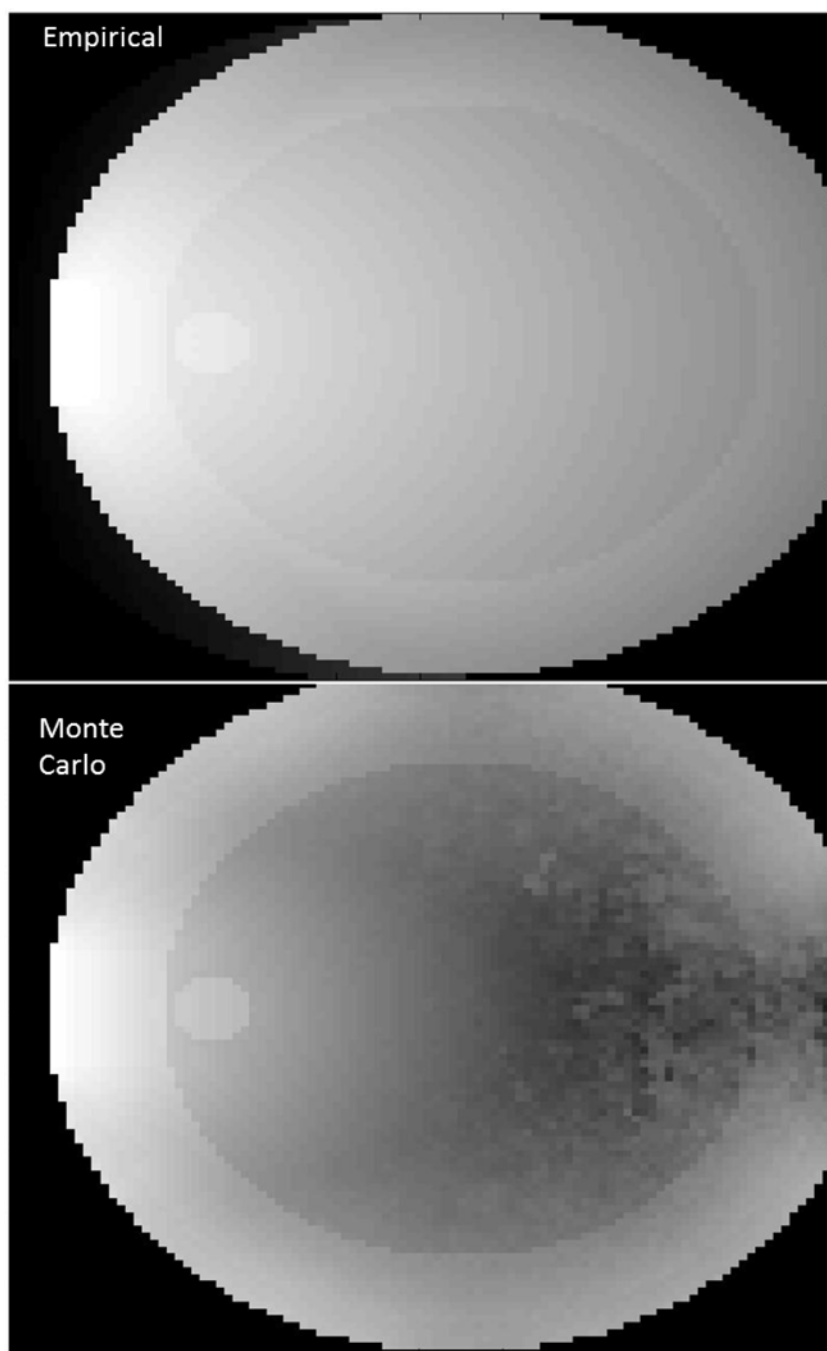
Figure 5.19 Comparison of photon energy distribution images (2D) between the Empirical algorithm and Monte Carlo in a head phanton with tumor (astrocytoma).

5.3.4 Simulating Fluence Buildup

The effect of fluence buildup is seen in Monte Carlo simulations near the photon source. This effect largely depends on the albedo of the optical medium, where larger albedos enhances this buildup effect compared to smaller values and is significant within 1mm from the source in brain tissues. . While the Empirical can closely match the Monte Carlo over diffusion region, the existing derived weights were inadequate to simulate the fluence build up; therefore, a new set of weights were derived. Plots for the best possible match in white matter, gray matter, skull bone, and astrocytoma are shown in figures 5.19-5.22, respectively, and their corresponding weights are listed in table 5.3. While the Empirical model may not exactly match Monte Carlo simulated data for both the diffuse and near-source regions at the same time, it can modified to match the MC based on the region of interest. One must note that the problem of fluence build occurs within the first millimeter or two, thus a smaller voxel size will be required.
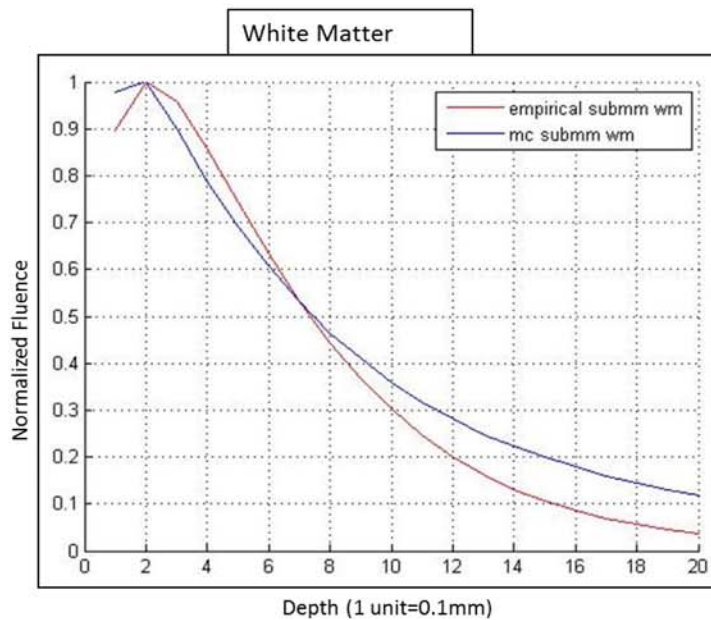
Figure 5.20 Comparison of the buildup fluence buildup between Monte Carlo and Empirical Model for White Matter.
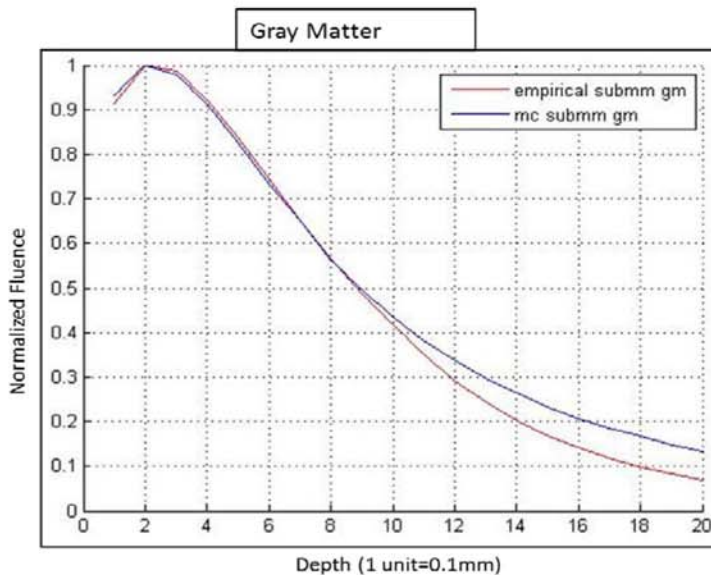
Figure 5.21 Comparison of the buildup fluence buildup between Monte Carlo and Empirical Model for Gray Matter.
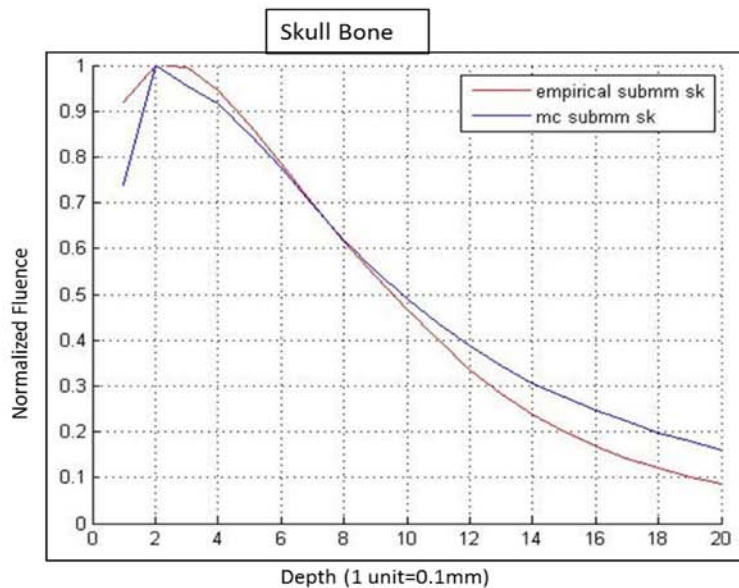
Figure 5.22 Comparison of the buildup fluence buildup between Monte Carlo and Empirical Model for Skull Bone.
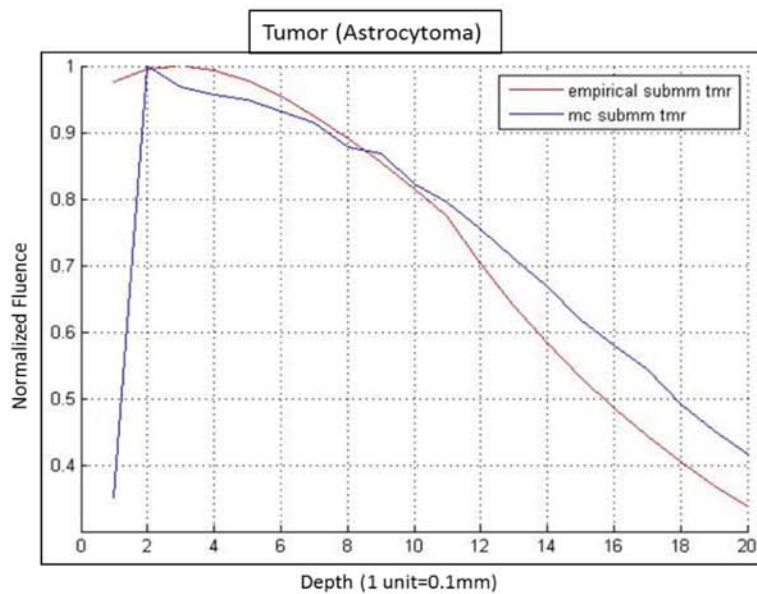
Figure 5.23 Comparison of the buildup fluence buildup between Monte Carlo and Empirical Model for Tumor (Astrocytoma).

Table 5.3 Weights derived to obtain fluence buildup

Tissue Phantom	Voxel Size (mm)	Wt1	Wt2	R-square
White Matter	0.1	0.637486	0.090629	0.995372
Gray Matter	0.1	0.711962	0.07201	0.999807
Skull Bone	0.1	0.735052	0.066237	0.994337
Tumor (Astrocytoma)	0.1	0.89585	0.026037	0.955473

5.4   Discussion

In this specific aim, a reasonable accuracy (R-square of 0.999) was achieved between

the Empirical and the Monte Carlo for homogeneous and heterogeneous brain

phantoms and validated using the optical dosimetry probe. Overall, the empirical model

provides an alternate voxel based approach of estimating photon fluence in 3D

heterogeneous tissues besides the diffusion approximation and Monte Carlo methods.

Even though it was less accurate compared to Monte Carlo simulated data, (up to 36%%

error between probe and empirical), the reduction in computation times (8 hours per

MC simulation versus 4-12 seconds of Empirical simulation), provides a means for

clinical and preclinical applications, in particular for large data sets and iterative-based

optimization routines. Similar to the GPU MC code, it is easily integrated with existing

imaging modalities such as CT and MR due to its voxelated structure. In order to

simulate fine structural boundaries of brain tissues, we need a fine resolution of around

1mm, for which the CT dataset becomes very large. For such large datasets, where the

Monte Carlo cannot be run iteratively (>24 hours execution time), the empirical

algorithm can replace the Monte Carlo for preliminary analysis. More study is required

to investigate the % match due to difference in the optimization routine and the

dependence of weights on the scattering properties of the medium. Further research is

also needed to understand the mismatch at object boundaries, particularly at larger

depths.

6   SPECIFIC AIM4: IMAGE-GUIDED OPTICAL TRANSMISSION STUDIES IN HUMAN SKULL BONES

6.1   Introduction

The skull forms an optical attenuator (absorber and scatterer) in the transmission of near-Infra-red light to the brain. The success of any NIR based imaging or therapeutic technique involving the brain depends on an accurate and precise determination of the optical transmission properties of the skull. The skull bone consists of osteocytes and calcium deposits in various densities and complex geometries based on different anatomical locations in the skull. Previous studies have looked at the optical transmission properties of different tissues [93-99] using collimated laser beams with powers ranging from $10mW/cm^2$ to $25mW/cm^2$ [93, 94]. These studies included NIR transmission through human cadaver skulls [94]. In our study, we used an NIR laser source ($17.64mW/cm^2$) with a complex super-Gaussian broad beam profile and investigated if a relationship between voxel-based HU and optical attenuation exists. Simulated Monte Carlo data was compared to measured beam intensity and distribution implementing the TiO_2-based optical dosimetry probe. This data was used to investigate the relationship between the HU from CT images and the optical attenuation by measuring the transmitted NIR light through human cadaver skulls Critical to these measurements is the ability to quantify low power fluence transmitted through the skull

afforded with the TiO2 optical dosimetry probe compared to the calorimeter used in previous bone transmission studies [91, 92].

To date, studies [80, 100-102] have measured the optical properties of the brain tissues, have mapped the heterogeneity and inter-sample variations. The comparison of the optical properties of skull bone found in these studies [80, 100-102] is shown in table 6.1. It shows a wide variation in the optical properties reported for the human skull bone. A comprehensive work by Bashkatov et al. [100] mapped these variations in optical properties of the skull bone at different wavelengths. Our aim is to further understand this complexity caused by variations in the bone density and bone thickness to map out an accurate fluence map of the Monte Carlo in the brain. The use of Computed Tomography images provides a 3D map of the heterogeneous bone structure and allows us to accurately generate the boundary conditions and density maps using the Monte Carlo.

Table 6.1 Optical properties of skull bone measured at 800nm wavelength in different studies [80, 100-102]. The anisotropy factor (g) is 0.9.

Study By:	Absorption Coefficient (μ_a) (cm^{-1})	Scattering Coefficient (μ_s) (cm^{-1})
Firbank et al.	0.24	18.4
Bashkatov et al.	0.11	19.48
Pifferi et al.	0.07	12.5
Ugryumova et al.	0.25	21

6.2   Materials and Methods

6.2.1   Optical Bone Dosimetry Setup

10 Different skull bone samples [courtesy: Lisa Hilliard (Medical Laboratory Science Program) and Dr. James Walker (Dept. of Basic Medical Sciences)] were used for the optical transmission study. The light source consisted of the optical fiberguide (see chapter 2) connected to a laser source. The NIR output of the fiberguide was measured using a calorimeter to be 19.94mW or (17.64 mW/cm^2) at 800nm wavelength. For transmission studies, the optical fiberguide was placed against the outer surface of the skull bone, such that its aperture was flat against the bone surface, thus providing a normal exposure. The fluence transmitted through the bone was measured using the TiO$_2$ dosimetry probe by placing it against the inner surface of the skull bone, opposite the fiberguide on the other side of the skull, which was ensured by locating the point of maximum fluence. The energy fluence for 5 points or locations per skull was acquired, and at each location the measurement was repeated three times. A total of 10 cadaver skull bones were measured, which gave a total of 50 measurement data points. The setup for these experiments is shown in figures 6.1 and 6.2.
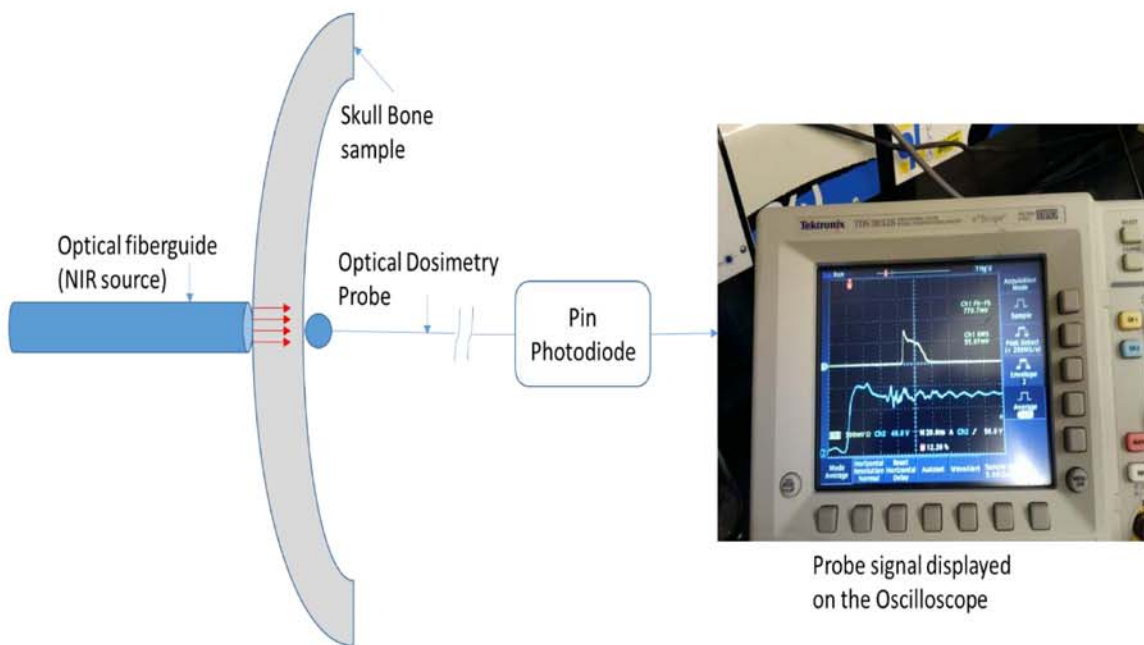
Figure 6.1 Setup to measure the optical transmission of NIR light through the skull bone. The source used is an optical fiberguide connected to a laser. The NIR fluence collected by the probe tip is carried by an optical fiber to a PIN photodiode circuit, whose electrical output is read using an oscilloscope (right).

For the lateral beam profile measurements, each skull was placed in a large Plexiglas cuvette such that the point of illumination (marked previously on the skull surface) was directly in contact with the cuvette bottom. The transparent optical bench helped in alignment of the skull and the source with good precision. The experimental setup is shown in figures 6.2 and 6.3. The lateral profile was first measured in air and in water 0.5cm from the inner skull surface. While measurement in air was for further validation of optical transmission, the measurement in water was for a more realistic scenario, where the refractive index of water is similar to that of water.
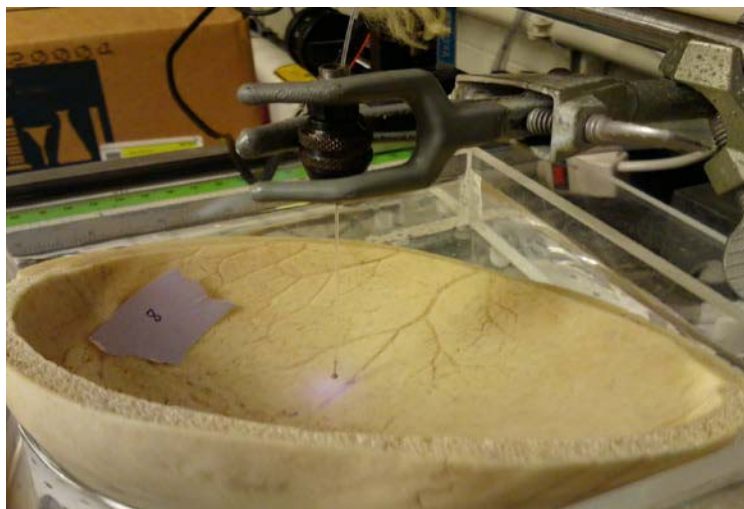
Figure 6.2 Skull bone sample (top portion) used in the experiment. The dosimetry probe is also seen.
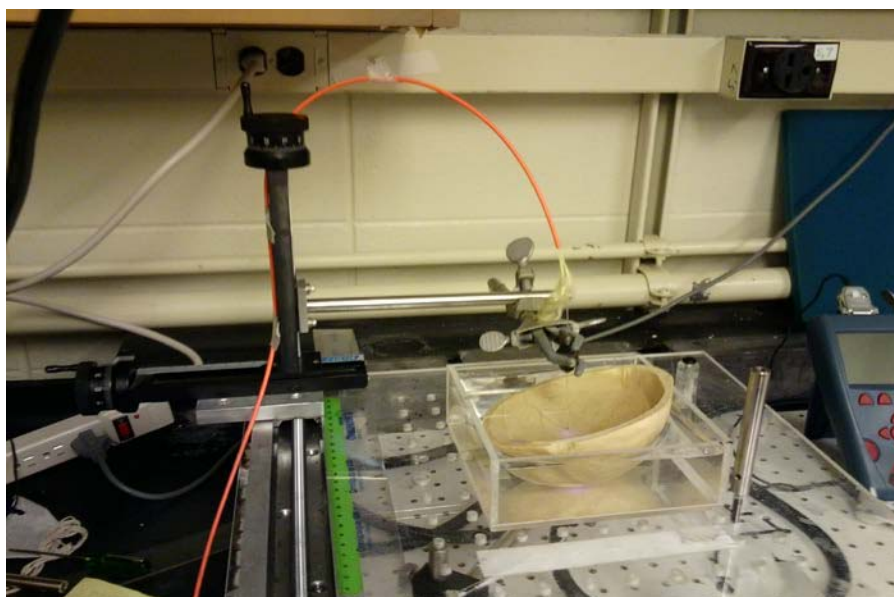
Figure 6.3 Optical dosimetry setup for lateral beam profile measurement in skull sample.
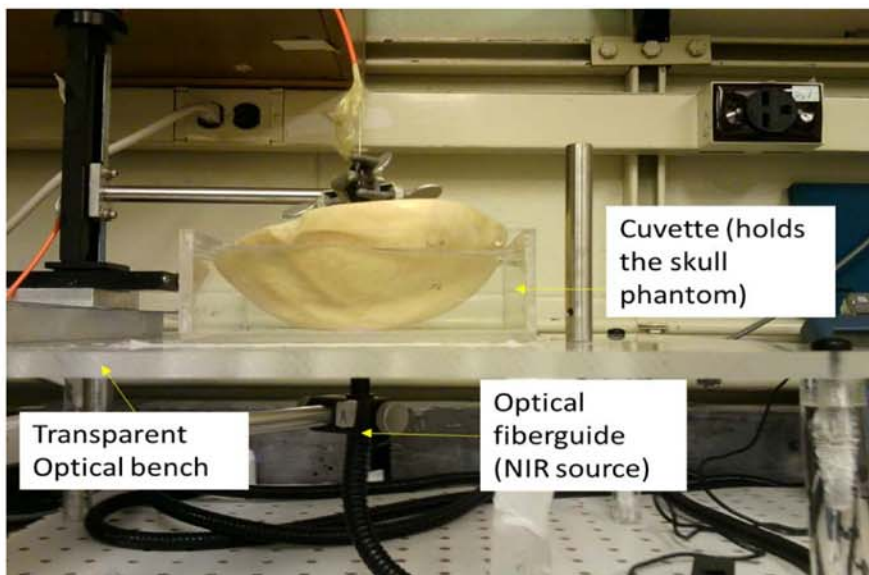
Figure 6.4 Optical dosimetry setup for lateral beam profile measurement in a skull sample. This shows the illuminatin setup using the optical fiberguide source.

6.2.2 Acquisition and Processing of CT Images of the Skull Bone

Computed Tomography (CT) was used to map optical boundaries and density of the bone on a Philips Brilliance CT scanner. The CT images were acquired at 300 mAs and 120 kVp, and reconstructed with a slice thickness of 0.67mm, pixel size (xy plane) of 0.2344mm, and the bone kernel. The points for measurement on each skull phantom were labeled using CT contrast beads and marked with a pencil (see Figure 6.5), which were used to identify the points of illumination.

Figure 6.5 shows the use of CT contrast beads to mark the point of illumination on the skull samples. The CT images were displayed and processed using Matlab based software, which was custom developed to identify the source and detector positions and simulate the bone boundaries on CT images, as shown in figure 6.5. The point of

measurement for optical transmission lies on the inner skull boundary on the line while lateral profile is measured at 0.5 cm from the inner skull surface.

In order to identify the source voxel for illumination, another line was drawn tangential to the skull surface, passing through the intersection point of the bead and the outer skull surface as shown in figure 6.5 (B). The cross product of the illumination vector and the source tangential vector is the other vector which also lies tangential to the skull surface along the z axis [0 0 1]. The source voxels are then identified as those lying on the 3D circle defined by the two tangential vectors. The parametric equation used of a 3D circular disk [103] can be then used to represent the fiberguide source surface as described by the two tangential vectors. Thus one can accurately represent any broad source in the Monte Carlo at any arbitrary angle as used in the experimental setup.
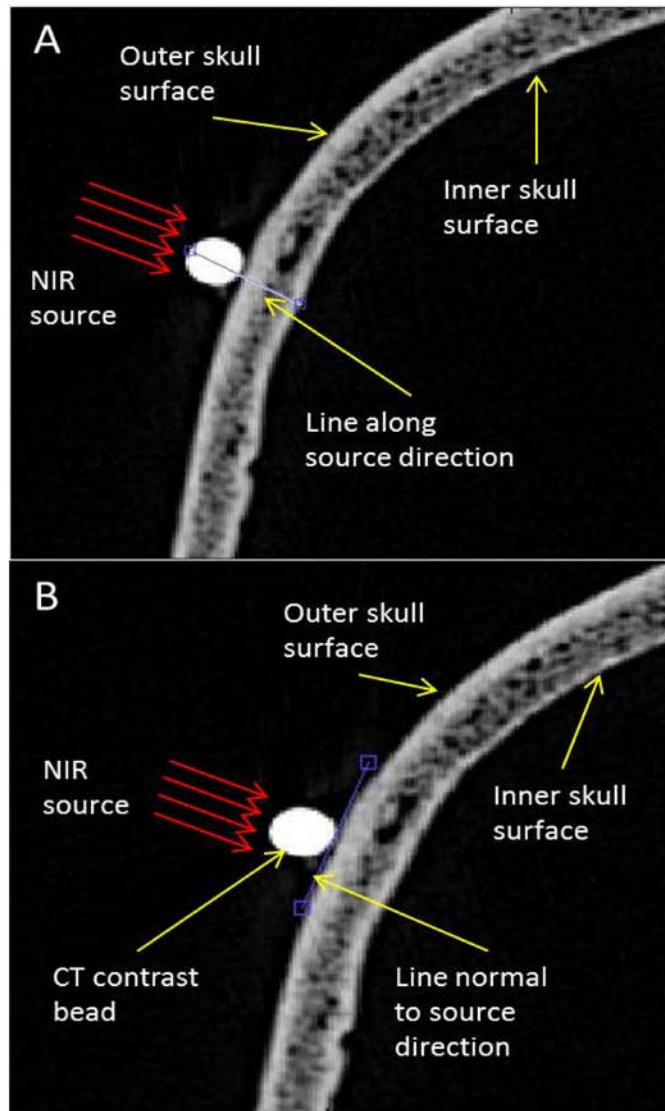
Figure 6.5 The CT image of a skull bone is processed in Matlab to extract the source directional vector (A) and in-plane source vector (B) by drawing lines (blue) on the image and extracting the end points of the lines to calculate the vectors. The third vector is the cross product of these two vectors and is in the plane of the source.

6.3   Results

6.3.1   Optical Transmission Measurements in the Skull

The result for the optical transmission for 10 different phantoms is shown in figures 6.6,

6.7 and 6.8. Note that the phantoms are numbered from 1-4 and 6-11 as phantom 5 was

not used (incomplete CT scan). The optical transmission measurements show a wide

variation in the optical power transmitted, due to variation in skull thickness and

(heterogeneity in) bone densities. In order to map the Monte Carlo fluence to the %

transmission measurements of the probe, we used CT images to determine the optical

path-length through the bone (i.e. skull thickness in the direction of illumination). The

skull thicknesses measured using CT images showed different skull thicknesses both

within and across the skull samples. The measured skull thicknesses from the CT images

are shown in figure 6.9. We also measured the lateral beam profiles in the skull

phantoms in air and water as shown in figure 6.10. The measured probe voltage is seen

to be higher in water compared to air. This is mainly due to the difference in the skull-

medium interface boundary conditions, such as the differences in the refractive indices

of skull bone and water versus skull bone and air.
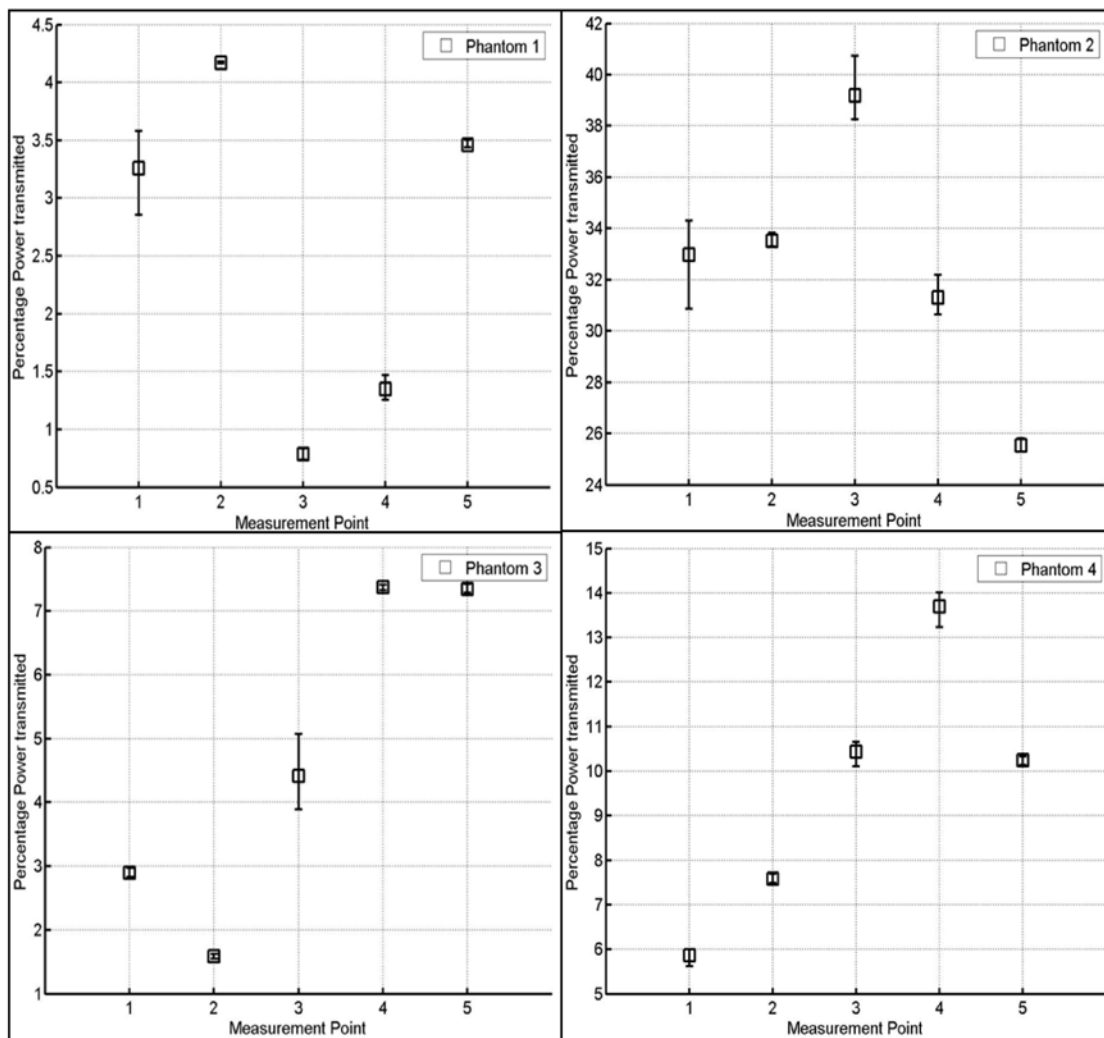
Figure 6.6 Percentage fluence transmitted for phantoms 1-4 measured using the probe calorimeter setup.
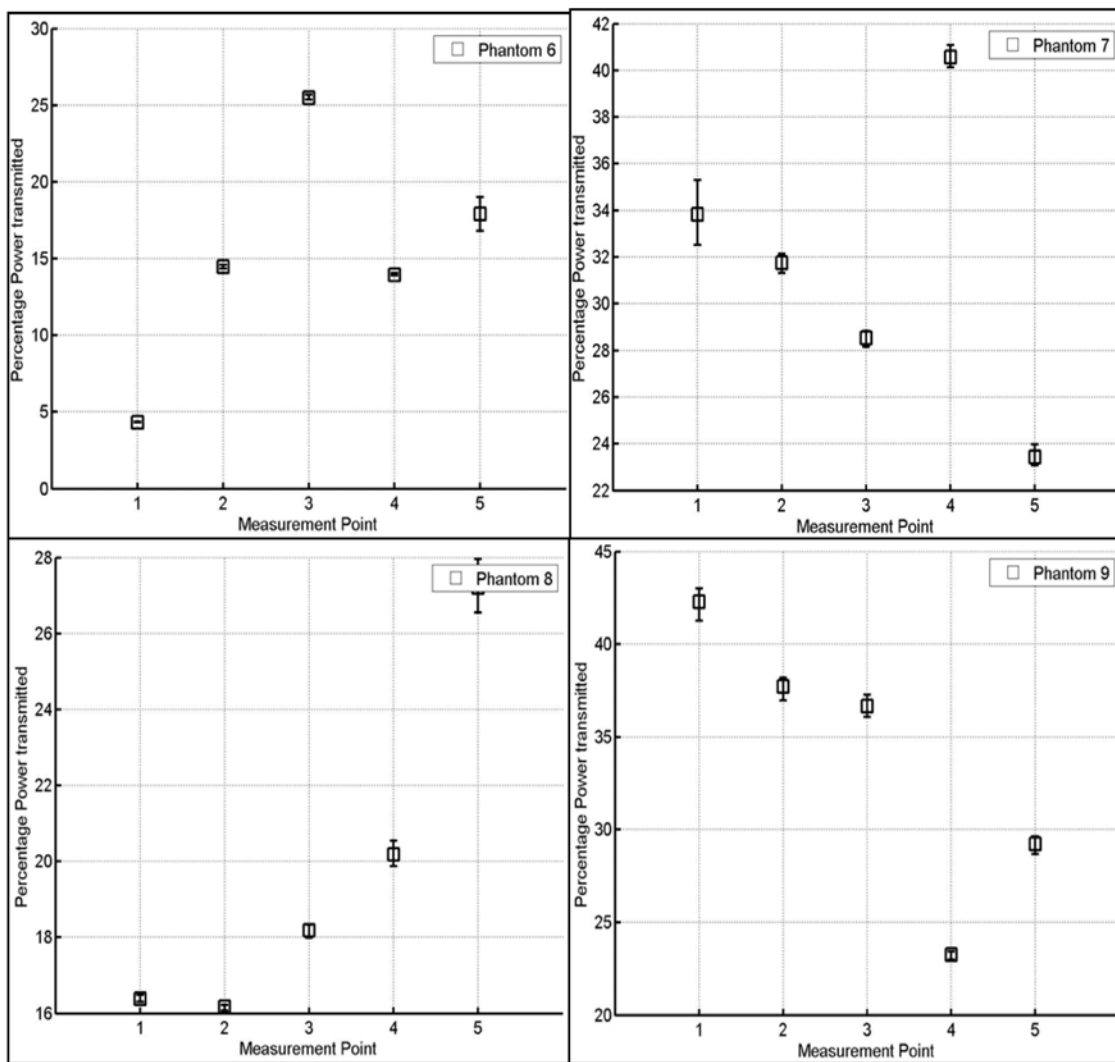
Figure 6.7 Percentage fluence transmitted for phantoms 6-9 measured using the probe calorimeter setup.
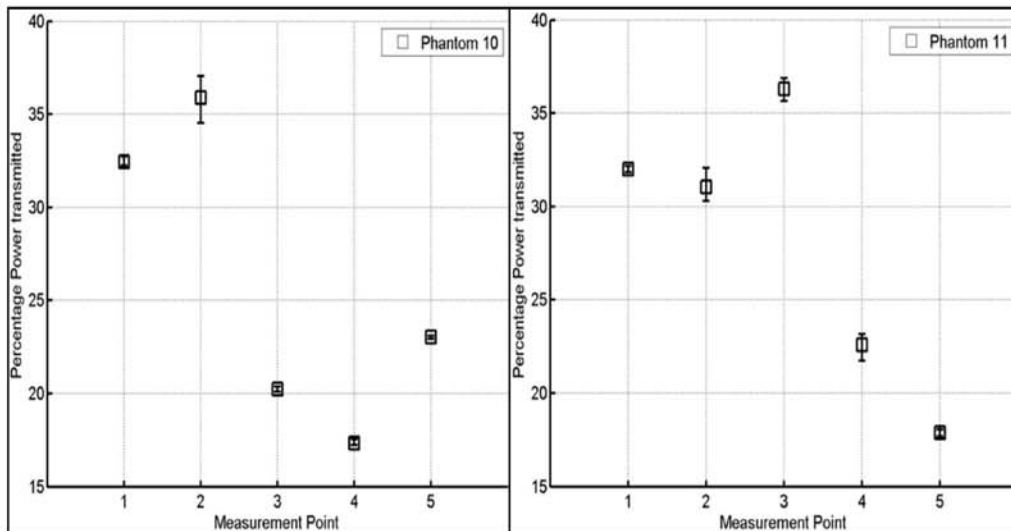
Figure 6.8 Percentage fluence transmitted for phantoms 10-11 measured using the probe calorimeter setup.
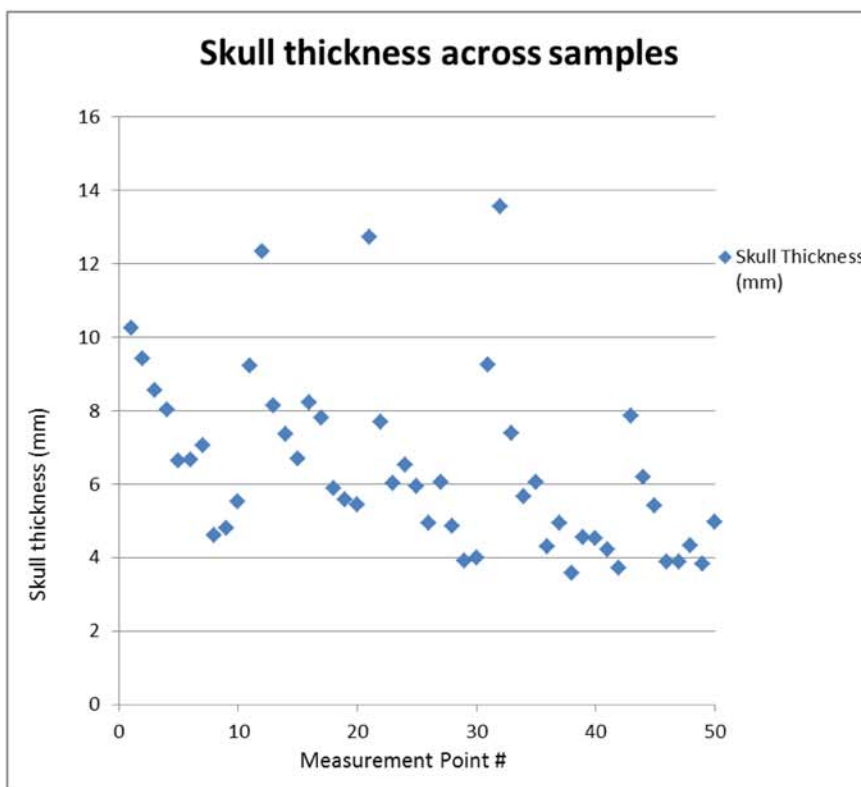
Figure 6.9 Skull thicknesses measured across skull samples using CT image data. Measurement points: Phantom1 (1-5), Phantom2 (6-10), Phantom3 (11-15), Phantom4 (16-20), Phantom5 (21-25), Phantom6 (26-30), Phantom7 (31-35), Phantom8 (36-40), Phantom9 (41-45), Phantom10 (45-50).
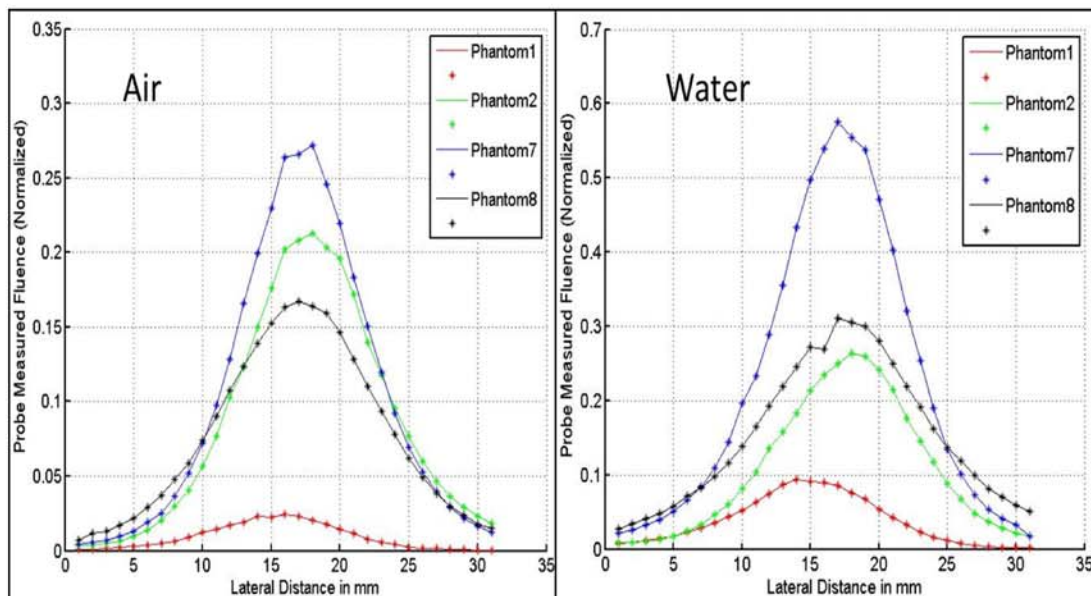
Figure 6.10 Lateral beam profile (fraction transmitted) measured using the dosimetry probe in air and water 0.5mm from the inner skull surface.

6.3.2 Comparison with the Monte Carlo

Based on the three different sets of optical properties of the skull bone shown in table 6.1, three Monte Carlo profiles were obtained with a super-Gaussian beam distribution. The fluence profiles along and perpendicular (lateral profile) are shown in figures 6.11 and 6.12 respectively. The Monte Carlo simulations show that different optical properties of the skull bone will give rise to different transmission characteristics, which could result in different transmission factors and lateral beam profiles. The lateral beam profiles due to different optical properties also show the variations between the three models.
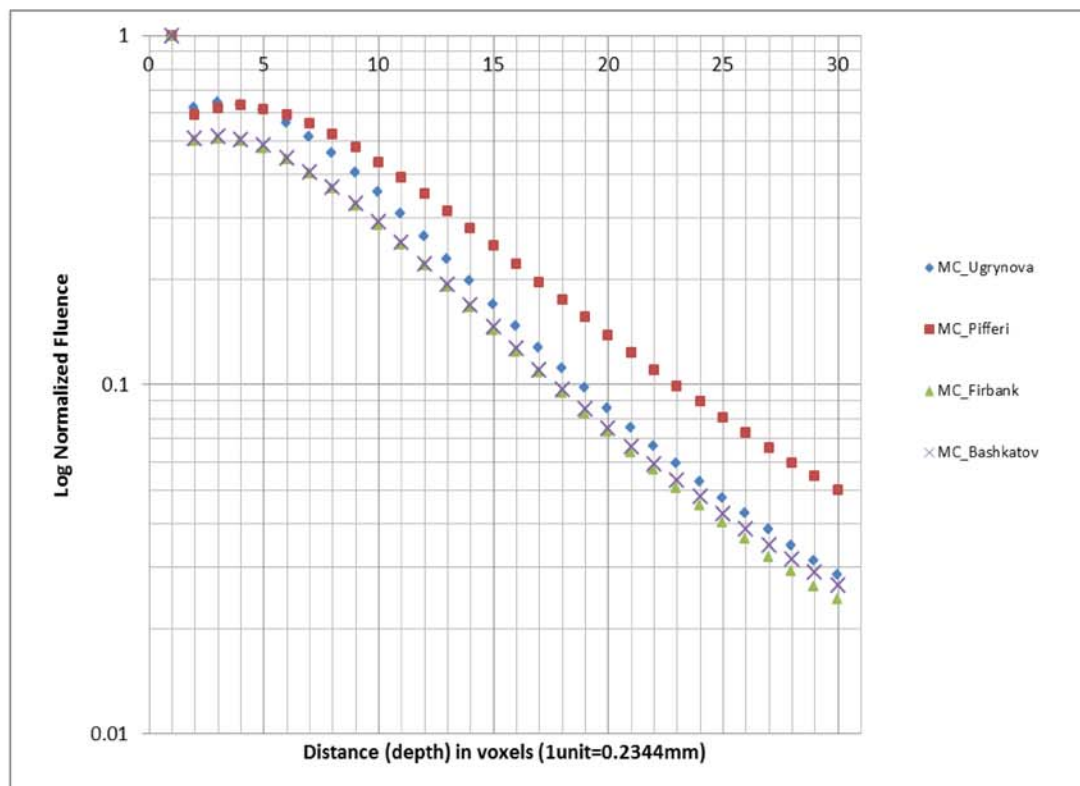
Figure 6.11 MC simulated fluence profiles along beam axis for a homogeneous skull medium generated using Monte Carlo simulations for three sets optical properties of the skull bone (Ugrynova et al, Pifferi et al, Firbank et al, and Bashkatov et al). A broad beam super-Gaussian NIR source (800nm wavelength) was simulated.
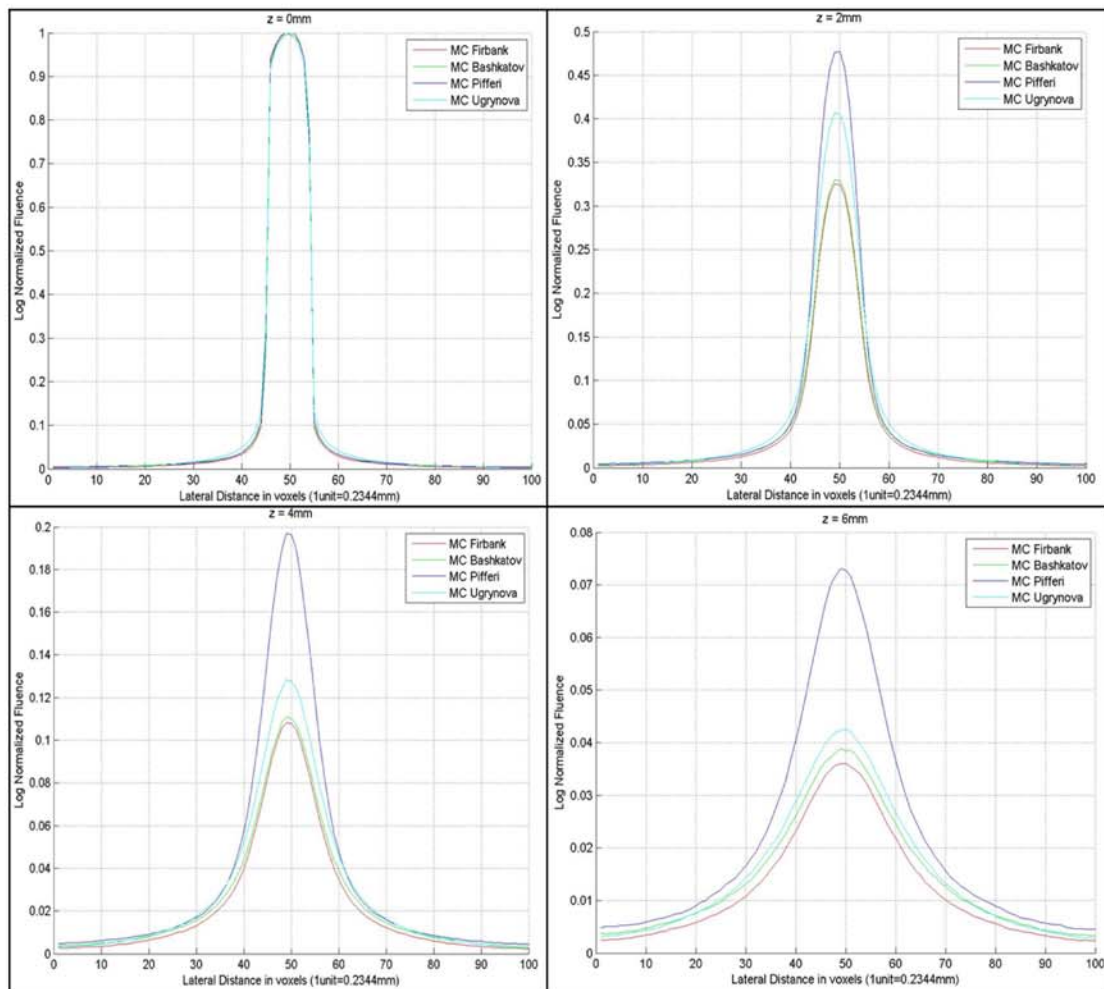
Figure 6.12 MC simulated lateral fluence profiles at different depths (z=0,2,4,6mm) for a homogeneous skull medium generated using Monte Carlo simulations for three sets optical properties of the skull bone (Ugrynova et al, Pifferi et al, Firbank et al, and Bashkatov et al). A broad beam super-Gaussian NIR source (800nm wavelength) was simulated.

The % power transmitted using the probe-calorimeter setup was then compared to the % power transmitted using the Monte Carlo simulations. The simulations in the homogeneous skull phantom were used in the form of a lookup table to derive the MC generated fluence using interpolation. The skull thicknesses measured using CT images were used to look up and interpolate the corresponding normalized fluences in the MC

table. The percentage power transmitted is the normalized fluence on the beam axis at that specific depth multiplied by 100. Figure 6.13 shows the comparison between the transmitted values measured by the probe and those simulated by the Monte Carlo code.
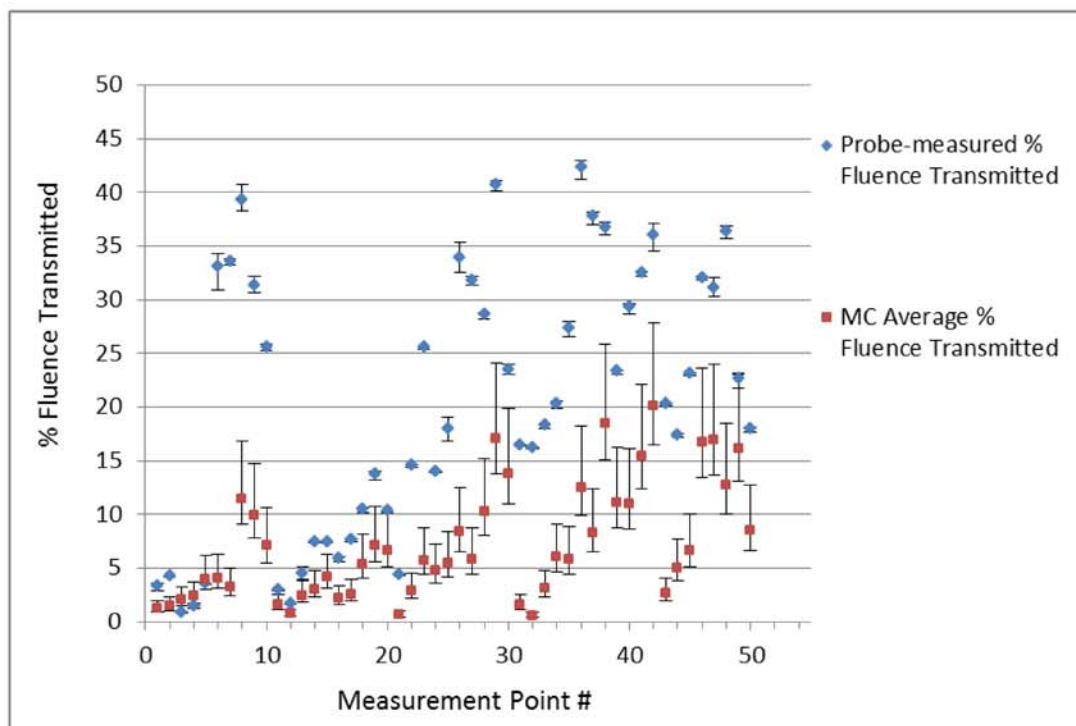
Figure 6.13 Comparison of % transmitted fluence between the calorimeter-probe measurements and the Monte Carlo. The error bars in the probe measurements represent the maximum and minimum intensities in the 3 averages, while the error bars in the Monte Carlo are the minimum and maximum fluences between the 3 optical models (see table 6.1).
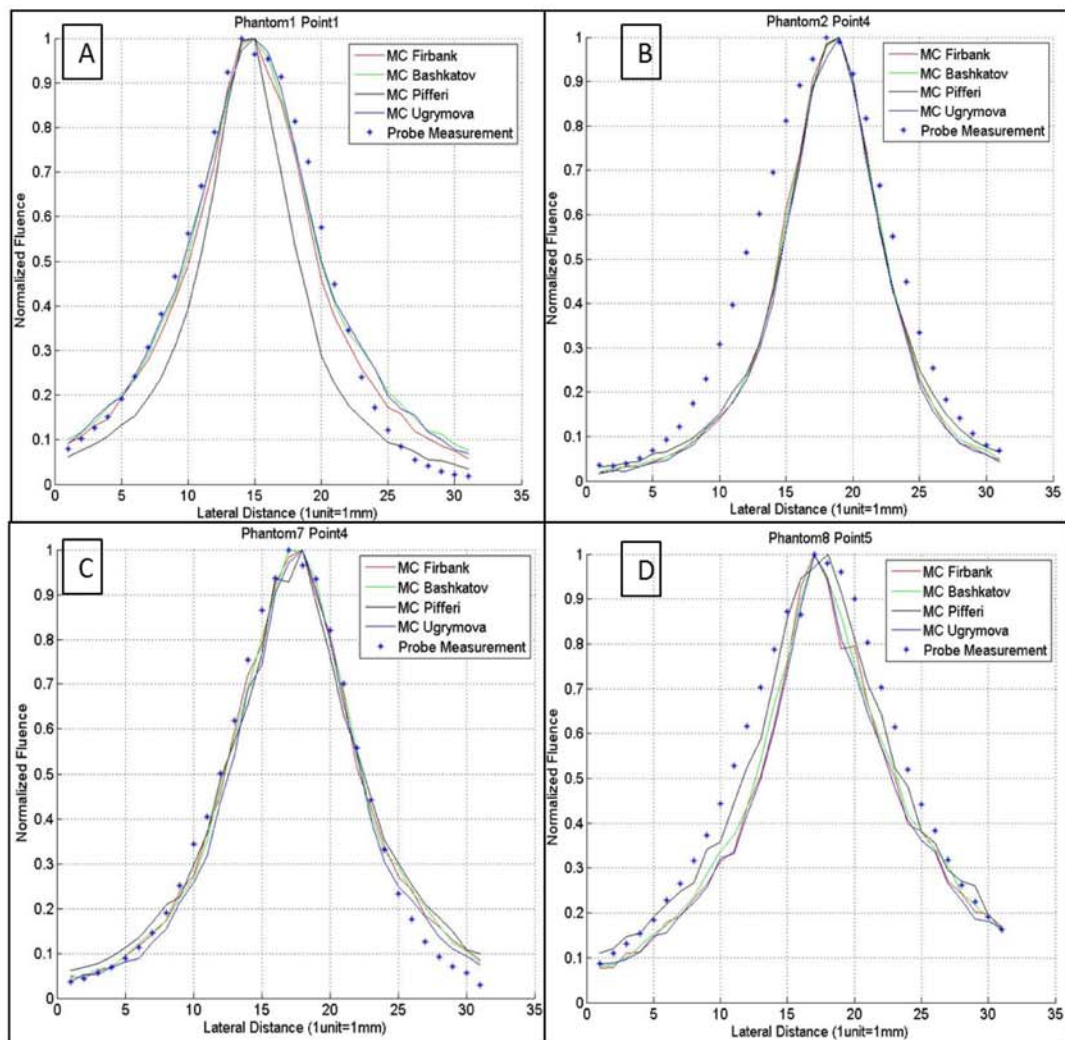
Figure 6.14 Comparison of lateral profiles measured using dosimetry probe with the Monte Carlo in water.
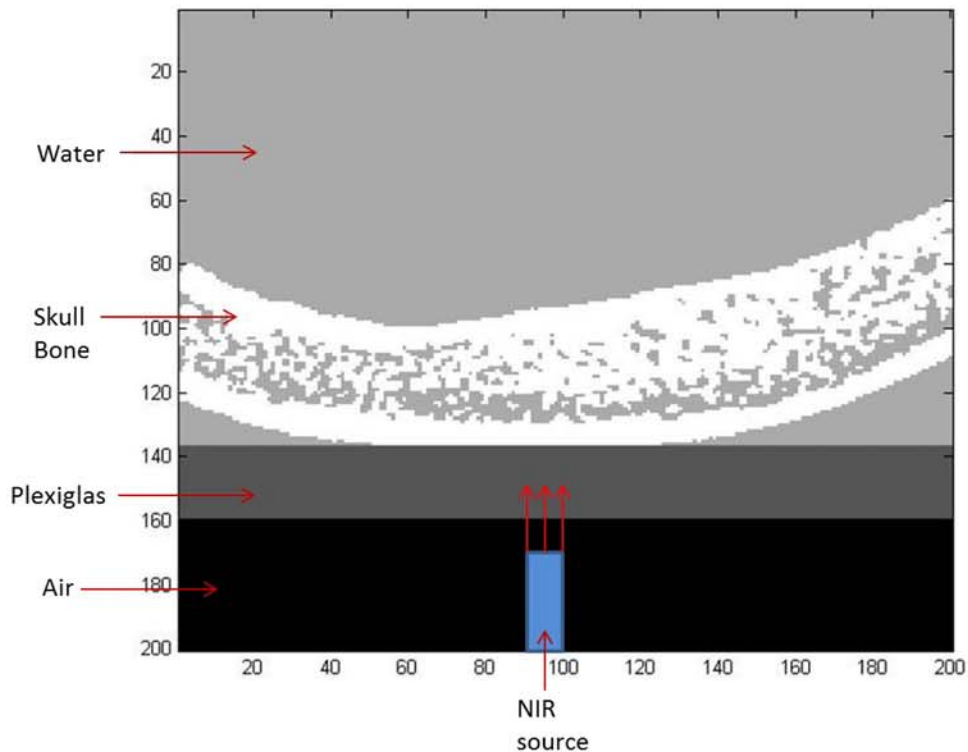
Figure 6.15 Boundary conditions simulated using the CT image-guided Monte Carlo.

Figure 6.13 shows that the Monte Carlo simulations compare closely to some of the probe measurement (example points 1-5 in phantom 1) while underestimating the transmission % for other points. Thus Monte Carlo overestimates the attenuation of fluence in the skull, while probe readings show a higher % power transmitted through the skull. The reason behind this difference is due to the differences in the bone density in the skull samples which were not included in the MC simulations. The MC simulations were done in a homogeneous brain phantom and assumed uniform density.

In order to demonstrate the feasibility of using CT image-guided skull boundaries for Monte Carlo simulation, we used the CT images to map the heterogeneity in distribution of bone voxels along with the geometry of boundaries. Figure 6.14 shows the comparison between the lateral fluence profiles (transmitted through the skull immersed in water) measured using the probe versus the Monte Carlo. The boundary conditions derived from the CT images is shown in figure 6.15. The fluence profiles were normalized to the maximum value measured at a depth of 5mm from the inner surface of the skull bone. The results show a close match between the beam spread simulated by the Monte Carlo and measured by the probe. This demonstrates the accuracy with which the scattering properties of the bone were modelled, along with the CT image enhanced boundary conditions. The CT images of the skull sample also show the changing Hounsfield CT numbers across the bone which is the result of varying density of the bone structure. Thus compared to previous studies, we have used the CT images to account for the different optical path lengths along with boundary conditions. We have however, not accounted for the varying densities of the bone, which results in differences between the probe and the Monte Carlo fluences.

6.4   Discussion

The optical transmission study demonstrates the difficulties encountered in optical bone transmission studies. The Monte Carlo can accurately simulate photon attenuation in the skull only when all the optical properties and boundary conditions are simulated correctly. While the skull bone has been measured and modelled as a relatively

homogeneous medium in optical simulation studies, the use of CT images shows that it is far from homogeneous with wide variations in bone densities at different anatomical regions and across subjects. This presents a complicated scenario to model the optical propagation of photons through the skull.

We demonstrated the accuracy of boundary conditions determined using CT images by comparing the lateral profiles between the Monte Carlo and the dosimetry probe. The close match between the profiles shows the accuracy of our simulations. Our study thus also reduced the error in measuring skull thicknesses using calipers, which so often goes unnoticed in complex tissue structure. For example: an error in correctly measuring the skull thickness by a millimeter can result in errors of up to 40% in magnitude (seen from our MC data in figures 6.11, 6.12), depending on the boundary and illumination conditions. Thus any imaging or therapeutic technique needs to reduce the errors due to mismatch in the boundary conditions by using an anatomical imaging technique (such as CT) which can map different tissue boundaries.

To improve the match between the Monte Carlo and the measured fluence in skull models, we hypothesize that using bone density measurement technique such as quantitative CT can significantly improve the localization of high scattering bone voxels in the skull bone. The mapping of Hounsfield values of CT number can be directly linked to the bone density values by imaging bone density phantoms in the CT scanner. This would provide volumetric images of bone densities which can be converted (scaled) to

the corresponding scattering absorption coefficients. The optical coefficient scaling will

also need to be calibrated by measuring the optical properties of bone samples of

known density.

7   DISCUSSION

7.1   Design and Calibration of Optical Dosimetry Probe

We designed and calibrated an optical dosimetry probe with a linear and isotropic response to input photon fluence. While several designs of the dosimetry probe exist in the medical optics market, the application of a specific dosimetry probe for an application mainly depends on probe sensitivity to the wavelengths of interest. The isotropicity of the dosimetry probes used in past studies is shown in table 7.1. The choice of the titanium dioxide for the probe was made to achieve maximum sensitivity by maximizing scattering near 800nm wavelength through the use of Titanium Dioxide (by Du Pont [71]). We were able to prove that the sensitivity as well as the angular response of the TiO_2 probe is superior to that of the conventional Nylon based probes. The next innovative aspect of our study was the determination of absolute photon fluence from the probe response. By using the linear relationship between the probe and calorimeter responses, along with the experimental derivation of a calibration factor for relating probe response in air to that in water, we were able to derive the mathematical relationship to absolutely quantify photon fluence in tissues for in-vitro or in-vivo studies in the future. This provides a simple technique to quantify probe response experimentally for validation purposes.

Table 7.1 Optical dosimetry probe composition (diameter<2mm) and % isotropicity variation [68, 69].

Study By:	Probe tip material	Isotropicity Variation %
Marijnissen et al	ArniteTM	11%
Marijnissen et al	NylonTM	11%
Van Staveren et al	Helioseal (dental sealant)	20%
Our study	TiO_2 (best probe)	13%
Our study	Nylon^{TM} (best probe)	17%

7.2   Dosimetric Validation of a Monte Carlo based Optical Planning tool

The Monte Carlo based tool for photon dose estimation was successfully optimized and validated, using optical dosimetry probe measurements, to study light dose delivery to brain tissue phantoms. Past studies have compared the dosimetry probe measurements with simpler models (non voxelated) of the Monte Carlo along illumination axis in homogeneous phantoms and tissues for simpler (flat or isotropic) beam profiles (flat beams) [104-106]. The long computation times (several hours to days) associated with the Monte Carlo prevented any rigorous approach for validation across diverse tissues and illuminations. To the best of our knowledge, this is the first study which has sought to rigorously validate a 3D voxelated GPU based Monte Carlo using dosimetry probe measurements both along and perpendicular to the illumination axis, in homogeneous and heterogeneous tissue phantoms with independently derived optical properties, and using a complex super-Gaussian beam profile. We also validated the Monte Carlo in a diffuse beam generated by an integrating sphere, thus proving the flexibility of the Monte Carlo in accurately generating different beam profiles.

A past validation study [106] had compared the angular radiance with different viewing angles using a flat cleaved probe to the Monte Carlo in tissue phantoms. The measured versus Monte Carlo fluence showed a % error variation from 0 to 25% (seen from the figure 6 plot in the publication) along the beam axis, mainly due to mismatch in optical properties. In another study [105], Monte Carlo validation using dosimetry in a dissected Pig Bronchus tissue showed higher % mismatch of around 50% at a 4cm depth, with measurement error amounting to 15% variation. The other significant part of the error was accounted for by the variation in estimation of the tissue optical properties and tissue boundaries. This demonstrates the importance of independent validation of optical properties of the medium along with an accurate simulation of boundary conditions in the Monte Carlo. In this study, the average % error was well within 25% for most of our measurements. The acceleration provided by the GPU platform improves the applicability of the Monte Carlo by reducing the development time associated with iteratively optimizing the accuracy of the boundary and illumination conditions, which was difficult to achieve in the CPU based model.

7.3   An Empirical algorithm for preliminary optical dose planning

The brain is a highly heterogeneous structure and has complex distribution of tissues with varying optical properties. In order to target a metastatic site in the brain we need to be able to optimize the light delivery to that region in the brain, which requires us to analyze multiple light source positions, orientations as well as source illumination profiles; all of which affect the path that photons travel through the brain. Since this

requires iterative techniques, multiple simulations of photon propagation with different illumination conditions require a tool which is faster than the Monte Carlo (run time a few hours). Hence an alternative Empirical model with a run time of a few seconds was designed as a preliminary investigation tool with a reasonable level of accuracy compared to the Monte Carlo in heterogeneous tissues.

The Empirical model is based on the photon convolution algorithm and uses weights to simulate photon scatter from one voxel to another. Its 3D voxel based design helps us to integrate it with the Monte Carlo along with 3D imaging modalities such as CT and MR. The empirical algorithm was iteratively optimized with the Monte Carlo and tested in optical phantoms resembling a child's brain with and without a tumor. We found a reasonable degree of match between the Monte Carlo and the Empirical in both homogeneous and heterogeneous tissues. The lateral profiles in homogeneous phantoms were also compared and were found to match between the two models.

The errors in the Empirical model include boundary conditions which the Empirical in not able to simulate as well as the Monte Carlo. Further research is necessary to investigate and optimize the Empirical algorithm to make it more accurate in complex heterogeneous tissues. Due to its reasonable degree of accuracy, the Empirical algorithm can be used as a preliminary investigation tool to narrow down the optimal illumination conditions while the Monte Carlo can be the Gold standard for the final dose calculation. A comparison of various models used in past studies is shown in table

7.2. The Empirical approach performs favorably with its moderate level of accuracy and

fast execution times with respect to Monte Carlo.

Table 7.2 Methods for photon propagation [61, 107-111]. Estimated simulation times
for a head study.

Method:	Execution time	Advantages	Disadvantages
CPU based Monte Carlo [110]	>24 hours (1-3 days)	Accurate	Long execution times
GPU based Monte Carlo [61]	4-8 hours	Accurate	Moderate execution time
Radiative Transport Equation (RTE) [108]	Few minutes	Accurate	Complex to solve
Diffusion Approximation (DE) [107, 111]	Few seconds	Accurate only at large distances from source, at g<0.6 and at higher albedos ($\mu_s/ \mu_s+ \mu_a$)	Errors at short distances from source, at g>0.6 and at lower albedos ($\mu_s/ \mu_s+ \mu_a$)
Hybrid model (MC + DE) [109]	1-3 hours	Moderate accuracy (1-2 std dev)	Moderate accuracy (1-2 std dev)
Empirical Model [64]	4-12 seconds	Moderate accuracy	Non-analytical technique

7.4   Image guided transmission studies in skull bone phantoms

The NIR transmission study demonstrates the complexities of modelling the optical

properties of the skull bone. Past studies measuring the NIR transmission through skulls

had measured the transmission through cadaver skulls with intact soft tissues [93, 94].

This resulted in larger uncertainties in the optical properties (with the inclusion of soft

tissue). No image based technique was used in these studies to determine the optical pathlength through the samples. In this study we measured NIR transmission through pure skull bone samples without any soft tissue, and demonstrated the use of image guided technique to determine the bone thickness. We also successfully demonstrated the close match between the lateral beam profiles measured in water, which shows the importance of using image guided techniques to map heterogeneity of the skull. While the transmission errors between the Monte Carlo and the probe measurements are significant for some measurement points, this study tries to point at the scope for future investigation into the heterogeneous density distribution of scatterers in the skull bone. There is a need to model the varying optical scattering of the bone based on bone density. Methods such as bone densitometry and quantitative CT can be used to calculate skull bone densities and can potentially improve the accuracy of the Monte Carlo.

8   FUTURE WORK

While this study has looked specifically at building optical dosimetry and photon dose simulation tools with an intention of future application in light induced drug activation in the brain, we are still some distance away from accurately modelling the drug release maps in the brain. This is mainly due to a lack of understanding of the mechanism for drug activation. While in vitro experiments as well as in vivo studies in mice have shown promising results, the energy threshold for drug release is still uncertain. The drug-nanocomplex molecule consists of a therapeutic drug molecule (e.g. lapatinib) which is complexed with a gold plated silica nanoshell [8]. These nano-complexes are incubated in macrophages and monocytes and injected into the blood stream, cross the blood brain barrier, and accumulate in the metastatic lesions in the brain [8, 9]. Thus when irradiated with an NIR source with sufficiently high power, the high absorption cross-section of gold nanocomplexes results in heating of the nanoparticles [86, 87] which can lead to breakage of bonds binding the drug (or any fluorescent molecule) to the nano-complex and subsequent release and activation of the drug [8, 9]. The resulting rise in temperature has been shown to be around 37.4^0C as shown in previous studies [86] for a power of $4W/cm^2$. The heating property of the gold nanoshell nano-complex can be

tuned by changing the size of the silica nano-shell compared to that of the outer gold

plated layer [88], which allows us to optimize the drug molecule with respect to the

wavelength of light delivery. While this shows significant promise in the mechanism of

temperature rise leading to drug release, more research needs to be done to

understand the temperature related dependence of the drug release.

In order to control the rise in temperature in the region surrounding the nanocomplex

molecules, the instantaneous energy provided to a tissue region can be controlled by

adjusting the pulse width of the laser beam. The use of pulsed laser beams has been

shown to improve the instantaneous temperature rise and release in of drug molecules

tethered to nanoparticles, compared to continuous wave lasers [112]. This will allow

more instantaneous power to be coupled to the nano-molecules while reducing the

chances of laser induced adverse tissue heating or denaturing of the drug. The

maximum energy that can be safely coupled to tissues is limited by the maximum

permissible exposure (MPE). MPE values are based on the pulse duration and the tissue

type [113, 114]. For example, if we use a laser beam of 1 ns pulse duration, the MPE to

the skin is 3.17×10^7 W cm^{-2} [113, 114]. Based on our prior Monte Carlo simulations using

a flat 2cm diameter beam, the amount of power coupled to the soft tissue for 1.1cm

and 0.2cm thick adult and neonatal skull is 4.3×10^5 W cm^{-2} and 1.5×10^7 W cm^{-2},

respectively. Thus, a therapeutic drug molecule needs to be designed such that it can be

activated at a threshold less than the maximum permissible power coupled to tissues at

a specific depth. For example, a drug molecule with an energy threshold of 1 Wcm^{-2} can

be released up to a depth of 3.8cm in the white matter of an adult brain (skull thickness

1.1cm, gray matter thickness 2cm), and up to 4.6cm in a neonatal brain (skull thickness

0.2cm, gray matter thickness 0.2cm) for a flat beam of 2cm diameter, 1ns temporal

spread and an input fluence of $3.17x10^7$ W cm^{-2}. This shows that the structure of the

brain and path lengths through the tissue can significantly impact the fluence coupled

and the effectiveness of therapy. However, these results demonstrate the feasibility of

NIR stimulated drug release, in particular for children where 4.6cm is more than half the

diameter of the brain cavity.

Even though reducing the laser pulse width can enhance drug release without

denaturing the drug or heating the tissue, it can also significantly impact the

instantaneous or peak energy fluence within the brain. Multiple scattering in brain

tissues causes the photons to travel with different optical path-lengths, thus

simultaneously increasing the pulse width and decreasing the peak power at greater

depths. Past studies have measured the temporal dispersion of laser beams in scattering

tissues by using time of flight method with a fast optical detector [115, 116], or by using

radio frequency (RF) modulated light source by detecting the phase of transmitted light

[117, 118]. A theoretical basis of calculation of the temporal point spread function is

also provided by Arridge [115] using the temporal point spread function (TPSF), while

the TPSF is the "response function (Green's Function) of the medium to a delta impulse"

[115]. The Monte Carlo used in this study has the ability to simulate photon pulses with

user-defined pulse duration. In our MC simulation studies, we calculated the temporal

dispersion of a 1ns laser beam by measuring the full width at tenth maximum of the laser pulse as it propagated along a circular head phantom (boundary conditions shown in figure 5.11). The plot of temporal pulse width to the depth in the tissue is displayed in figure 8.1. The pulse width is seen to increase by 4-5 times at depths of 3-5cm. This implies a reduction in the fluence per unit time by approximately this same amount. The pulse width was measured by calculating the full width at tenth maximum, a quantity which determines the pulse duration up to 10% of maximum fluence. Therefore, some care must be taken when considering the pulse width in the design of the treatment plan. To date, the Monte Carlo can be used to predict this spread to optimize drug release. Further temporal convolution methods may need to be added to the empirical model.
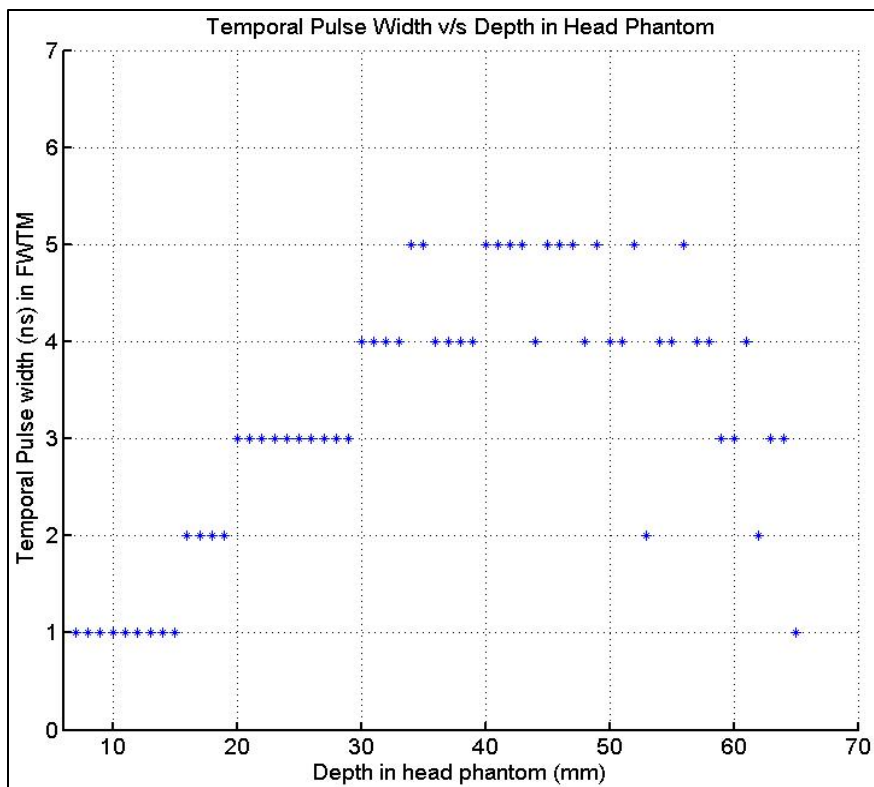
Figure 8.1 MC simulation of temporal pulse width versus depth in a heterogeneous head phantom (see figure 5.11) for an input pulse 1ns wide. The pulse width was measured by calculating the Full Width at Tenth Maximum (FWTM) to analyze the temporal beam spread.

There is a need to quantify the errors due to variability of brain tissue properties, particularly the skull bone between different patients. The skull bone thickness and density varies across different anatomical regions of the brain [89]. The optical properties of the skull bone are also seen to vary across samples [89], which can result in differences between the estimation and delivery of photon fluence to metastatic tissue in the brain. Hence the need for using a medical imaging system such as Computed Tomography (CT) is necessary to segment tissues in the brain, especially the bone-brain interface. In our study the average % error in determining bone thickness

measured using versus a scale was 30%. Thus modelling the skull heterogeneity using CT images has the potential to reduce simulation errors of up to 73% in the fluence coupled to soft tissue in adult brains and up to 20% in neonatal brains with respective skull thicknesses of 1.1cm and 0.2 cm.

While the bone-brain interface is clearly visible using CT images, better soft tissue contrast is necessary to segment different soft tissues such as white matter, gray matter, cerebrospinal fluid and metastatic lesions (if any) in the brain. This is best done using Magnetic Resonance Images (e.g. T2-weighted), which are also used as the standard imaging protocol to segment metastatic lesions in the brain [90]. The MR images however cannot be used to image the bone-brain interface, as bone images of the brain are generally poor. Hence there is a need to super-impose and co-register CT and MR images of patients about to undergo optical therapy. This would provide a significant improvement in brain tissue segmentation over CT-only or MR-only based imaging and segmentation methods. The co-registration software (e.g. Gamma Plan [91, 92]) used needs to be highly accurate to ensure minimal errors in boundary conditions which need to be accurately depicted by the Monte Carlo. Phantom studies to determine image registration accuracy [92] can be done to quantify any errors related to inaccurate tissue boundaries.

LIST OF REFERENCES

LIST OF REFERENCES

1. Niwinska A, Murawska M, Pogoda K (2010), Breast cancer brain metastases: differences in survival depending on biological subtype, RPA RTOG prognostic class and systemic treatment after whole-brain radiotherapy (WBRT). Ann Oncol 21: 942–948.

2. Lin NU, Claus E, Sohl J, Razzak AR, Arnaout A, Winer EP (2008), Sites of distant recurrence and clinical outcomes in patients with metastatic triple-negative breast cancer: high incidence of central nervous system metastases. Cancer 113(10):2638–2645.

3. Amer, M. H., Al-Sarraf, M., Baker, L. H. and Vaitkevicius, V. K. (1978), Malignant melanoma and central nervous system metastases. Incidence, diagnosis, treatment and survival. Cancer, 42: 660–668.

4. Chang E, Wefel JS, Hess KR, et al. (2009), Neurocognition in patients with brain metastases treated with radiosurgery or radiosurgery plus whole-brain irradiation: a randomized controlled trial. Lancet Oncol; 10: 1037–44.

5. Sneed PK, Lamborn KR, Forstner JM, McDermott MW, Chang S, Park E, Gutin PH, Phillips TL, Wara WM, Larson DA (1999), "Radiosurgery for brain metastases: is whole brain radiotherapy necessary?" Int J Radiat Oncol Biol Phys 43(3):549–558.

6. Patchell RA, Regine WF (2003), "The rationale for adjuvant whole brain radiation therapy with radiosurgery in the treatment of single brain metastases." Tech Canc Res Treat 2(2):111–115.

7. Lo SS, Chang EL, Suh JH (2005), Stereotactic radiosurgery with and without whole-brain radiotherapy for newly diagnosed brain metastases. Expert Rev Neurother 5(4):487–495.

8. Choi MR, Stanton-Maxey KJ, Stanley JK, Levin CS, Bardhan R, Akin D, Badve S, Sturgis J, Robinson JP, Bashir R, Halas NJ, Clare SE. "A cellular Trojan Horse for delivery of therapeutic nanoparticles into tumors." Nano Lett 7(12) (2007): 37593765.

9. Mi-Ran Choi, Rizia Bardhan, Katie J. Stanton-Maxey, Sunil Badve, Harikrishna Nakshatri, Keith Stantz, Ning Cao, Naomi J. Halas, Susan E. Clare (2012), Delivery of nanoparticles to brain metastases of breast cancer using a cellular Trojan horse. Cancer Nano 3: 47-54.

10. Kelly, P. M., et al. "Macrophages in human breast disease: a quantitative immunohistochemical study." British journal of cancer 57.2 (1988): 174.

11. McBride, W. H. "Phenotype and functions of intratumoral macrophages." Biochimica et Biophysica Acta (BBA)-Reviews on Cancer 865.1 (1986): 27-41.

12. STEELE, R.J.C., BROWN, M. & EREMIN, 0. (1985). Characterization of macrophages infiltrating human mammary carcinomas. Br. J. Cancer, 51, 135.

13. Lwin, K.Y. Zuccarini, O., SLOANE, J.P. & BEVERLEY, P.C.L. (1985). An immunohistological study of leucocyte localization in benign and malignant breast tissue. Int. J. Cancer, 36, 433.

14. Kelly, P. M., et al. "Monoclonal antibody EBM/11: high cellular specificity for human macrophages." Journal of clinical pathology 41.5 (1988): 510-515.

15. Bliss, E., et al. "Quantitation of macrophages in human-breast cancer using monoclonal-antibody (ebm11) to human macrophages." Journal Of Pathology. Vol. 143. No. 1. Baffins Lane Chichester, W Sussex, England Po19 1ud: John Wiley & Sons Ltd, 1984.

16. Kruger, R. A., et al. "Thermoacoustic optical molecular imaging of small animals,[Mol." (2003): 113-123.

17. Kruger, Robert A., Daniel R. Reinecke, and Gabe A. Kruger. "Thermoacoustic computed tomography–technical considerations." Medical physics 26.9 (1999): 1832-1837.

18. Kruger, Robert A., Pingyu Liu, and C. Robert Appledorn. "Photoacoustic ultrasound (PAUS)—reconstruction tomography." Medical physics 22.10 (1995): 1605-1609.

19. Kruger, Robert A., and Pingyu Liu. "Photoacoustic ultrasound: Pulse production and detection in 0.5% Liposyn." Medical physics 21.7 (1994): 1179-1184.

20. Wang, Lihong V., ed. Photoacoustic imaging and spectroscopy. CRC press, 2009.

21. Jacques, Steven L. "Coupling 3D Monte Carlo light transport in optically heterogeneous tissues to photoacoustic signal generation." Photoacoustics2.4 (2014): 137-142.

22. Cox, Benjamin T., et al. "Two-dimensional quantitative photoacoustic image reconstruction of absorption distributions in scattering media by use of a simple iterative method." Applied Optics 45.8 (2006): 1866-1875.

23. Patrikeev, Igor, et al. "Monte Carlo modeling of optoacoustic signals from human internal jugular veins." Applied optics 46.21 (2007): 4820-4827.

24. Cheong, Yaw Jye, and Keith M. Stantz. "Photon propagation correction in 3D photoacoustic image reconstruction using Monte Carlo simulation." BiOS. International Society for Optics and Photonics, 2010.

25. Yalavarthy, Phaneendra K., et al. "Experimental investigation of perturbation Monte-Carlo based derivative estimation for imaging low-scattering tissue."Optics express 13.3 (2005): 985-997.

26. Kumar, Y. Phaneendra, and Ram M. Vasu. "Reconstruction of optical properties of low-scattering tissue using derivative estimated through perturbation Monte-Carlo method." Journal of biomedical optics 9.5 (2004): 1002-1012.

27. Jobsis, Frans F. "Noninvasive, infrared monitoring of cerebral and myocardial oxygen sufficiency and circulatory parameters." Science 198.4323 (1977): 1264-1267.

28. Elwell, C. E., et al. "Quantification of adult cerebral hemodynamics by near-infrared spectroscopy." Journal of Applied Physiology 77.6 (1994): 2753-2760.

29. Delpy, David T., et al. "Estimation of optical pathlength through tissue from direct time of flight measurement." Physics in medicine and biology 33.12 (1988): 1433.

30. Grinvald, Amiram, et al. "Functional architecture of cortex revealed by optical imaging of intrinsic signals." (1986): 361-364.

31. Haglund, Michael M., George A. Ojemann, and Daryl W. Hochman. "Optical imaging of epileptiform and functional activity in human cerebral cortex."Nature 358.6388 (1992): 668-671.

32. Chance, B., et al. "Comparison of time-resolved and-unresolved measurements of deoxyhemoglobin in brain." Proceedings of the National Academy of Sciences 85.14 (1988): 4971-4975.

33. Hoshi, Y. O. K. O., and M. A. M. O. R. U. Tamura. "Dynamic multichannel near-infrared optical imaging of human brain activity." Journal of Applied Physiology 75.4 (1993): 1842-1846.

34. Kato, Toshinori, et al. "Human visual cortical function during photic stimulation monitoring by means of near-infrared spectroscopy." Journal of Cerebral Blood Flow & Metabolism 13.3 (1993): 516-520.

35. Villringer, Arno, et al. "Near infrared spectroscopy (NIRS): a new tool to study hemodynamic changes during activation of brain function in human adults." Neuroscience letters 154.1 (1993): 101-104.

36. Gratton, Gabriele, et al. "Shades of gray matter: Noninvasive optical images of human brain reponses during visual stimulation." Psychophysiology 32.5 (1995): 505-509.

37. Villringer, Arno, and Britton Chance. "Non-invasive optical spectroscopy and imaging of human brain function." Trends in neurosciences 20.10 (1997): 435-442.

38. Powers, William J. "Hemodynamics and metabolism in ischemic cerebrovascular disease." Neurologic clinics 10.1 (1992): 31-48.

39. Tachibana, Hisao, et al. "Xenon Contrast CT–CBF Scanning of the Brain Differentiates Normal Age-Related Changes from Multi-infarct Dementia and Senile Dementia of Alzheimer Type." Journal of gerontology 39.4 (1984): 415-423.

40. Edwards, A. D., et al. "Measurement of hemoglobin flow and blood flow by near-infrared spectroscopy." Journal of Applied Physiology 75.4 (1993): 1884-1889.

41. Richter, C-P., et al. "Neural stimulation with optical radiation." Laser & photonics reviews 5.1 (2011): 68-80.

42. Chernov, Mykyta, and Anna Wang Roe. "Infrared neural stimulation: a new stimulation tool for central nervous system applications." Neurophotonics 1.1 (2014): 011011-011011.

43. Thompson, Alexander C., et al. "Modeling of light absorption in tissue during infrared neural stimulation." Journal of biomedical optics 17.7 (2012): 0750021-0750026.

44. Polikov, Vadim S., Patrick A. Tresco, and William M. Reichert. "Response of brain tissue to chronically implanted neural electrodes." Journal of neuroscience methods 148.1 (2005): 1-18.

45. Boyden, Edward. "A history of optogenetics: the development of tools for controlling brain circuits with light." (2011).

46. Yizhar, Ofer, et al. "Optogenetics in neural systems." Neuron 71.1 (2011): 9-34.

47. Wells, Jonathon, et al. "Optical stimulation of neural tissue in vivo." Optics letters 30.5 (2005): 504-506.

48. Wells, Jonathon, et al. "Biophysical mechanisms of transient optical stimulation of peripheral nerve." Biophysical journal 93.7 (2007): 2567-2580.

49. Shapiro, Mikhail G., et al. "Infrared light excites cells by changing their electrical capacitance." Nature communications 3 (2012): 736.

50. Chandrasekhar S. Radiative transfer, ed. Chandrasekhar, S. (1960): 20.

51. W. Cheong, S. A. Prahl, and A. Welch, "A review of the optical properties of biological tissues," in IEEE journal of quantum electronics, vol. 26, (1990): 2166–2185.

52. W. M. Star. Comparing the P3-approximation with diffusion theory and with Monte Carlo calculations of light propagation in a slab geometry. in SPIE Proceedings on Dosimetry of Laser Radiation in Medicine and Biology, vol. IS5, (1989): 146- 154.

53. G. Yoon, S. A. Prahl and A. J. Welch. "Accuracies of the Diffusion Approximation and its Similarity Relations for Laser Irradiated Biological Media." in Applied Optics, vol. 28, (1989): 2250-2255.

54. Henyey, Louis G., and Jesse Leonard Greenstein. "Diffuse radiation in the galaxy." The Astrophysical Journal 93 (1941): 70-83.

55. J. H. Joseph, W. J. Wiscombe, and J. A. Weinman, "The DeltaEddington Approximation for Radiative Flux Transfer," J. Atm. Sci. 33, 2452-2459 (1976).

56. M. J. C. Gemert, A. J. Welch, W. M. Star, M. Motamedi, and W. F. Cheong. Tissue optics for a slab geometry in the diffusion approximation, in Lasers Med. Sci., vol. 2, (1987): 295-302.

57. L. Wang, S. L. Jacques, and L. Zheng, "Monte Carlo modeling of light transport in multilayered tissues." Computer Methods and Programs in Biomedicine, vol. 47, (1995): 131-146.

58. D. A. Boas, J. P. Culver, J. J. Stott, and A. K. Dunn. "Three dimensional Monte Carlo code for photon migration through complex heterogeneous media including the adult human head." in Opt. Express, vol. 10, (2002): 159170.

59. J. Cheong, Monte Carlo simulation for light propagation through tissues, Master's Thesis, Department of Biomedical Engineering, Purdue University, 2009.

60. A. Prabhu Verleker, Monte Carlo simulation to study light propagation through biological tissues, Master's Thesis, Department of Biomedical Engineering, Purdue University, 2011.

61. Q. Fang and D. A. Boas, "Monte Carlo simulation of photon migration in 3D turbid media accelerated by graphics processing units," in Opt. Express, vol. 17, pp. 20178-20190, 2009.

62. Verleker, A. P., Fang, Q., Choi, M. R., Clare, S., Stantz, K. M. "An optical therapeutic protocol to treat brain metastasis by mapping NIR activated drug release: A pilot study." 2014 IEEE Nuclear Science Symposium and Medical Imaging Conference (NSS/MIC). IEEE, 2014.

63. Verleker, A. P., Fang, Q., Choi, M. R., Clare, S., Stantz, K. M. "Dosimetric Validation of a Monte Carlo based Optical Planning tool." Draft to be submitted to Applied Optics, 2016.

64. Verleker, A. P., Fang, Q., Choi, M. R., Clare, S., Stantz, K. M. "An empirical approach to estimate near-infra-red photon propagation and optically induced drug release in brain tissues." in SPIE BiOS International Society for Optics and Photonics (2015, March): 93080T-93080T.

65. I. Lux and L. Koblinger, Monte Carlo Particle Transport Methods: Neutron and Photon Calculation, CRC Press, vol. 102, 1991.

66. E. D. Cashwell and C. J. Everett, A Practical Manual on the Monte Carlo Method for Random Walk Problems, New York: Pergamon Press, 1959.

67. M. H. Kalos and P. A. Whitlock, Monte Carlo Methods, John Wiley & Sons, Inc., 1986.

68. Marijnissen, J. P. A., and W. M. Star. "Calibration of isotropic light dosimetry probes based on scattering bulbs in clear media." Physics in medicine and biology 41.7 (1996): 1191.

69. Van Staveren, Marijnissen J P A, Aalders M C G and W. M. Star. "Construction, quality assurance and calibration of spherical isotropic fibre optic light diffusers." Lasers Med Sci, (1995). 10(2): p. 137147.

70. Shaffer M. "Dynamic Contrast Enhanced Photoacoustic Computed Tomography in MDA-MB-231 and BT-474 Xenograft Tumor Models," PhD Thesis, Purdue University (2012), 54-67.

71. DuPont Titanium Technologies, Titanium Dioxide for Coatings. Coatings selection brochure P200067, (2002): Wilmington, DE.

72. Marijnissen, J. P. A., and W. M. Star. "Performance of isotropic light dosimetry probes based on scattering bulbs in turbid media." Physics in medicine and biology 47.12 (2002): 2049.

73. Pogue, Brian W., and Michael S. Patterson. "Review of tissue simulating phantoms for optical spectroscopy, imaging and dosimetry." Journal of biomedical optics 11.4 (2006): 041102-041102.

74. Madsen, Steen J., Michael S. Patterson, and Brian C. Wilson. "The use of India ink as an optical absorber in tissue-simulating phantoms." Physics in medicine and biology 37.4 (1992): 985.

75. Driver, I., et al. "The optical properties of aqueous suspensions of Intralipid, a fat emulsion." Physics in medicine and biology 34.12 (1989): 1927.

76. Van Staveren, Hugo J., et al. "Light scattering in Intralipid-10% in the wavelength range of 400 1100 nm." Applied optics 30.31 (1991): 4507-4514.

77. Flock, Stephen T., et al. "Optical properties of Intralipid: a phantom medium for light propagation studies." Lasers in Surgery and Medicine 12.5 (1992): 510519.

78. https://en.wikipedia.org/w/index.php?title=Beer%E2%80%93Lambert_law&oldid=718072472; last accessed May 11, 2016.

79. Van der Zee, Pieter, Matthias Essenpreis, and David T. Delpy. "Optical properties of brain tissue." OE/LASE'93: Optics, Electro-Optics, and Laser Applications in Science and Engineering. International Society for Optics and Photonics, (1993).

80. M. Firbank, M. Hiraoka, M. Essenpreis, D.T. Delpy. "Measurement of the optical properties of the skull in the wavelength range 650-950 nm," Phys. Med. Biol., 38 (1993):503-510.

81. Irvine, William M., and James B. Pollack. "Infrared optical properties of water and ice spheres." Icarus 8.1 (1968): 324-360.

82. Hielscher, Andreas H., Raymond E. Alcouffe, and Randall L. Barbour. "Comparison of finite-difference transport and diffusion calculations for photon migration in homogeneous and heterogeneous tissues." Physics in medicine and biology 43.5 (1998): 1285.

83. https://en.wikipedia.org/wiki/Radiative_transfer_equation_and_diffusion_theory_for_photon_transport_in_biological_tissue; last accessed May 11, 2016.

84. Flock, S.T.; Patterson, M.S.; Wilson, B.C.; Wyman, D.R., "Monte Carlo modeling of light propagation in highly scattering tissues. I. Model predictions and comparison with diffusion theory," Biomedical Engineering, IEEE Transactions on vol.36, no.12, (1989): 1162, 1168.

85. Wang, Lihong, Steven L. Jacques, and Liqiong Zheng. "CONV—convolution for responses to a finite diameter photon beam incident on multi-layered tissues." Computer methods and programs in biomedicine 54.3 (1997): 141-150.

86. Hirsch, L_R, et al. "Nanoshell-mediated near-infrared thermal therapy of tumors under magnetic resonance guidance." Proceedings of the National Academy of Sciences 100.23 (2003): 13549-13554.

87. O'Neal, D. Patrick, et al. "Photo-thermal tumor ablation in mice using near infrared-absorbing nanoparticles." Cancer letters 209.2 (2004): 171-176.

88. Oldenburg, Steven J., et al. "Infrared extinction properties of gold nanoshells." Applied Physics Letters 75.19 (1999): 2897-2899.

89. Bashkatov, Alexey N., et al. "Optical properties of human cranial bone in the spectral range from 800 to 2000 nm." Saratov Fall Meeting 2005: Optical Technologies in Biophysics and Medicine VII. International Society for Optics and Photonics, 2006.

90. Law, Meng, et al. "High-Grade Gliomas and Solitary Metastases: Differentiation by Using Perfusion and Proton Spectroscopic MR Imaging 1."Radiology 222.3 (2002): 715-721.

91. Marcu, S. M., et al. "GammaPlan®—Leksell Gamma Knife® radiosurgery treatment planning verification method." Medical physics 27.9 (2000): 2146-2149.

92. Watanabe, Yoichi, and Eunyoung Han. "Image registration accuracy of GammaPlan: a phantom study." (2008).

93. Jagdeo, Jared R., et al. "Transcranial red and near infrared light transmission in a cadaveric model." PloS one 7.10 (2012): e47460.

94. Lychagov, Vladislav V., et al. "Experimental study of NIR transmittance of the human skull." Biomedical Optics 2006. International Society for Optics and Photonics, 2006.

95. Stolik, S., et al. "Measurement of the penetration depths of red and near infrared light in human "ex vivo" tissues." Journal of Photochemistry and Photobiology B: Biology 57.2 (2000): 90-93.

96. Tauber, Stefan, et al. "Lightdosimetric quantitative analysis of the human petrous bone: Experimental study for laser irradiation of the cochlea." Lasers in surgery and medicine 28.1 (2001): 18-26.

97. Wedel, H. V., et al. "Soft-laser/ginkgo therapy in chronic tinnitus." (1995): 105-108.

98. Plucin, Jerzy, et al. "Theoretical foundations for noninvasive measurement of variations in the width of the subarachnoid space." Journal of biomedical optics 5.3 (2000): 291-299.

99. Young, A. E., et al. "Behaviour of near-infrared light in the adult human head: implications for clinical near-infrared spectroscopy." British Journal of Anaesthesia 84.1 (2000): 38-42.

100. Bashkatov, Alexey N., et al. "Optical properties of human cranial bone in the spectral range from 800 to 2000 nm." Saratov Fall Meeting 2005: Optical Technologies in Biophysics and Medicine VII. International Society for Optics and Photonics, 2006.

101. Pifferi, Antonio, et al. "Optical biopsy of bone tissue: a step toward the diagnosis of bone pathologies." Journal of biomedical optics 9.3 (2004): 474-480.

102. Ugryumova, Nadya, Stephen John Matcher, and Don P. Attenburrow. "Measurement of bone mineral density via light scattering." Physics in medicine and biology 49.3 (2004): 469.

103. http://demonstrations.wolfram.com/ParametricEquationOfACircleIn3D/; last accessed May 29, 2016.

104. Star, Willem M. "Light dosimetry in vivo." Physics in medicine and biology42.5 (1997): 763.

105. Murrer, L. H. P., J. P. A. Marijnissen, and W. M. Star. "Ex vivo light dosimetry and Monte Carlo simulations for endobronchial photodynamic therapy." Physics in medicine and biology 40.11 (1995): 1807.

106. Barajas, Oscar, et al. "Monte Carlo modelling of angular radiance in tissue phantoms and human prostate: PDT light dosimetry." Physics in medicine and biology 42.9 (1997): 1675.

107. Fang, Qianqian, et al. "Combined optical imaging and mammography of the healthy breast: optical contrast derived from breast structure and compression." IEEE transactions on medical imaging 28.1 (2009): 30-42.

108. Joshi, Amit, et al. "Radiative transport-based frequency-domain fluorescence tomography." Physics in medicine and biology 53.8 (2008): 2069.

109. Wang, Lihong, and Steven L. Jacques. "Hybrid model of Monte Carlo simulation and diffusion theory for light reflectance by turbid media." JOSA A10.8 (1993): 1746-1752.

110. Wang, Lihong, Steven L. Jacques, and Liqiong Zheng. "MCML—Monte Carlo modeling of light transport in multi-layered tissues." Computer methods and programs in biomedicine 47.2 (1995): 131-146.

111. Yoon, Gilwon, Scott A. Prahl, and Ashley J. Welch. "Accuracies of the diffusion approximation and its similarity relations for laser irradiated biological media." Applied Optics 28.12 (1989): 2250-2255.

112. Halas, Naomi, et al. Delivery of Nano-Tethered Therapies to Brain Metastases of Primary Breast Cancer Using a Cellular Trojan Horse. RICE UNIV HOUSTON TX, 2014.

113. Maini, Anil Kumar. Lasers and optoelectronics: fundamentals, devices and applications. John Wiley & Sons, 2013.

114. https://workspace.imperial.ac.uk/physics/Public/physicsdocs/about/safety/files/MPE-tables.pdf last accessed June 14, 2016.

115. Arridge, Simon R., M. Cope, and D. T. Delpy. "The theoretical basis for the determination of optical pathlengths in tissue: temporal and frequency analysis." Physics in medicine and biology 37.7 (1992): 1531.

116. Delpy, David T., et al. "Estimation of optical pathlength through tissue from direct time of flight measurement." Physics in medicine and biology 33.12 (1988): 1433.

117. Chance, Britton, et al. "Phase modulation system for dual wavelength difference spectroscopy of hemoglobin deoxygenation in tissues."OE/LASE'90, 14-19 Jan., Los Angeles, CA. International Society for Optics and Photonics, 1990.

118. Lakowicz, Joseph R., and Klaus Berndt. "Frequency-domain measurements of photon migration in tissues." Chemical physics letters 166.3 (1990): 246-252.

APPENDICES

Appendix A   Validating Scattering Coefficient of Intralipid through Probe

Measurements

In order to validate the scattering properties of the intralipid solution and further

validate the results from the spectrophotometer based studies, we used the dosimetry

probe and Monte Carlo to derive the reduced scattering coefficient of the intralipid

solution. Different concentrations of intralipid were illuminated in Plexiglas cuvette

using the diffuse broad beam from the integrating sphere (connected to the laser

source). The fluence was measured by the dosimetry probe along the beam axis for each

of the solutions. We then used the Monte Carlo to derive the scattering coefficient at

which the probe measurements match the Monte Carlo along the beam axis for the

same illumination and boundary conditions. The absorption coefficient of intralipid was

assumed to be the same as of water and the anisotropy factor of 0.636 was used in the

Monte Carlo. The results are close to those obtained by the spectrophotometer method

and are shown in figure 4.

This form of measurement was an additional validation step to the spectrophotometer

method. This method however needs to be precisely calibrated as additional errors and

offsets may be caused due to mismatch in boundary conditions as well as small

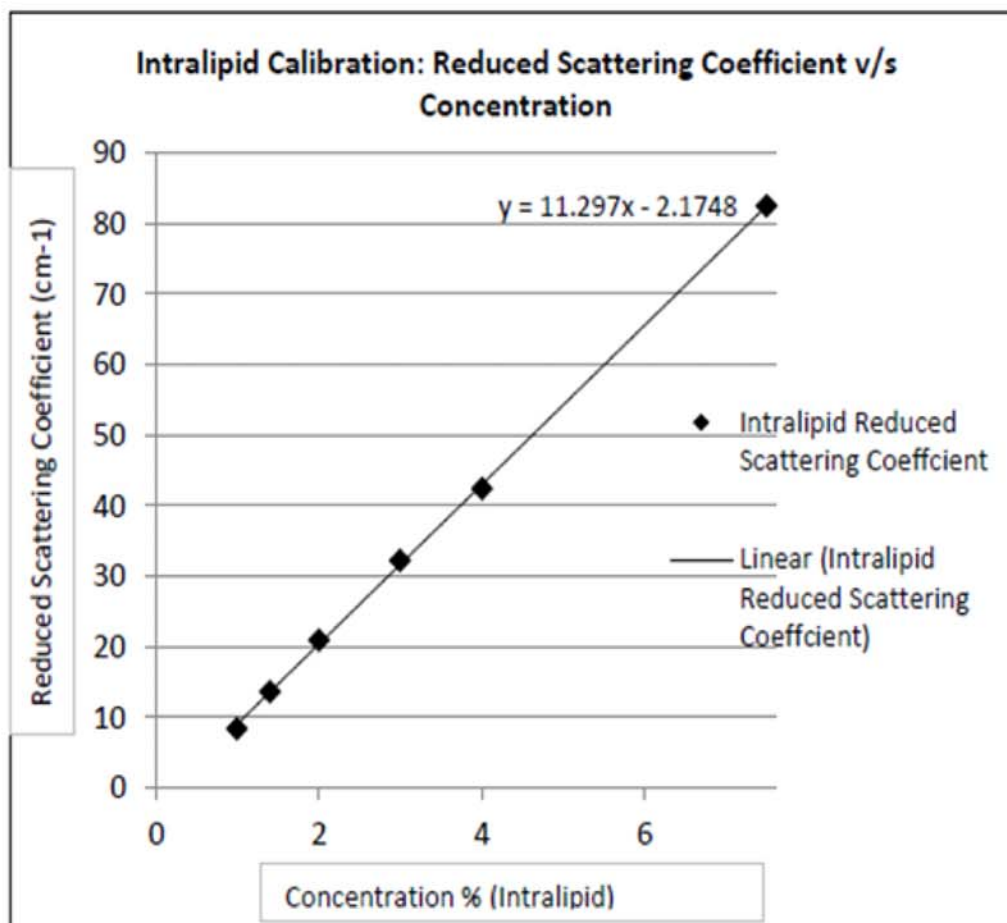differences in illumination profiles between the MC and probe measurements.

Figure 1 The scattering coefficient of intralipid measured using probe measurements in various concentrations of intralipid and correlated with MC simulations.

Appendix B   Optical Dosimetry in a Goat Skull Phantom

We validated the 3D Photon dose profiles in a goat skull phantom (figure 2). A goat skull (dry skull bone) was filled with an intralipid solution to resemble brain tissue. The power transmitted was measured to be 5.2% while MC simulations showed 3.2% transmission. The normalized MC and probe measurements within the phantom show identical profiles both along (figure 3) and perpendicular to the beam axis z (figure 4).
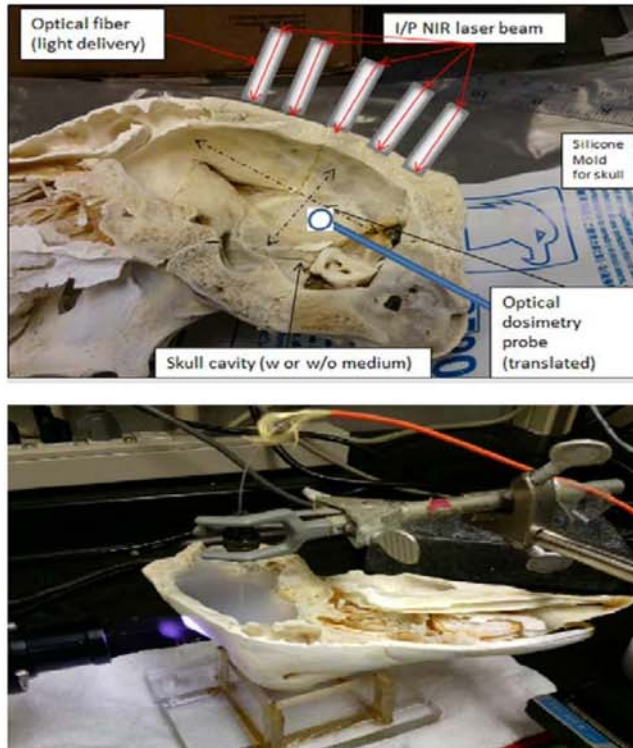

Figure 2 Experiments with a goat skull phantom to measure optical fluence distribution.
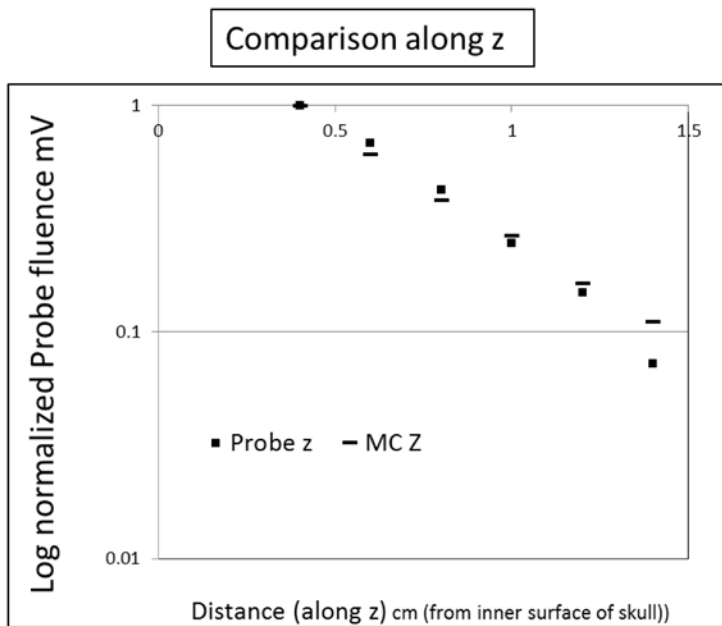
Figure 3 Experiments with a goat skull phantom to measure optical fluence distribution.
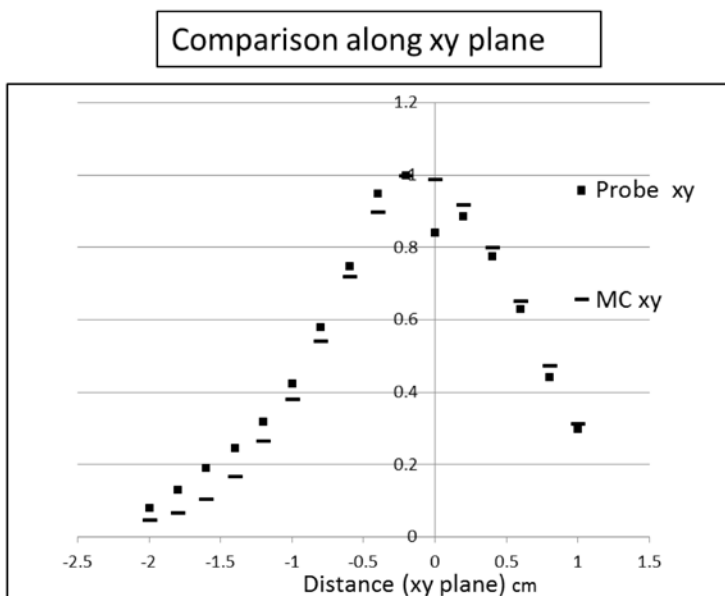

Figure 4 Experiments with a goat skull phantom to measure optical fluence distribution.

VITA

VITA

Akshay N. Prabhu Verleker

Division of Medical Physics and Imaging Sciences

School of Health Sciences

Purdue University

West Lafayette, Indiana 47907

EDUCATION:

2003-2007   Goa University, Goa, India   BE   ECE

2009-2011   IUPUI, Indianapolis, USA   MS   BME

   MS Thesis: Monte Carlo simulation to study propagation of light through biological tissues

2011-2016   Purdue University, West Lafayette, USA   PhD   Imaging Sciences

   PhD Thesis: Optical Dosimetry Tools and Monte Carlo Based Methods for Applications in Image Guided Optical Therapy in the Brain

PROFESSIONAL EXPERIENCE:

July 2007 – April 2009   Software Engineer   Persistent Systems Ltd., India
   Software Engineer at Persistent Systems: Development of software for resource allocation and employee data management

Sep 2009 – July 2016   Research Assistant   Purdue University

May 2011 – Aug 2011   Intern   3M, St Paul, MN
          Summer Intern at 3M: Application of Monte Carlo in predicting the
          photo-activated cure of dental composites

May 2013 – July 2013   PhD Intern   Philips Ultrasound, Bothell, WA
          PhD Intern at Philips Ultrasound: Development of 3D Volume Rendering
          Software for Photo-realistic rendering of fetal ultrasound images

June 2015 – Dec 2015   PhD Intern   GE Healthcare, Waukesha, WI
          PhD Intern at GE Healthcare: Development of Software tools and Physics
          based models for CT Image Quality optimization

RESEARCH PUBLICATIONS AND CONFERENCE PROCEEDINGS:

1. Verleker, A. P., Fang, Q., Choi, M. R., Clare, S., Stantz, K. M. "Dosimetric
   Validation of a Monte Carlo based Optical Planning tool." Draft submitted to
   Applied Optics, 2016.
2. Verleker, A. P., Fang, Q., Choi, M. R., Clare, S., Stantz, K. M. "An empirical
   approach to photon propagation based on Monte Carlo optimizations." Draft to
   be submitted to *Journal of Biomedical Optics*, 2016.
3. A. P. Verleker, Q. Fang, Mi-Ran Choi, S. Clare and K. M. Stantz, An optical
   therapeutic protocol to treat brain metastasis by mapping NIR activated drug
   release: A pilot study, *2014 IEEE Nuclear Science Symposium and Medical
   Imaging Conference (NSS/MIC)*, Seattle, WA, 2014, pp. 1-3. doi:
   10.1109/NSSMIC.2014.7431018
4. Verleker AP, Fang Q, Choi M-R, Clare S, Stantz KM. An empirical approach to
   estimate near-infra-red photon propagation and optically induced drug release
   in brain tissues. *Proc SPIE BiOS* 9308-29: 1-8, 2015 (doi: 10.1117/12.2079991)
5. Roth A, Krutulis M, Verleker A and Stantz K. Verification of Photoacoustic
   Computed Tomography Perfusion Imaging Using DCE-CT", *Med. Phys.* **41**,
   449 (2014); http://dx.doi.org/10.1118/1.4889245.
6. A Prabhu Verlker, Q Fang, MR Choi, S Clare and KM Stantz, A therapeutic
   protocol for treatment of brain metastasis through optically stimulated drug
   release (Poster Presentation; Certificate of Excellence), *OIGP Spring Reception*,
   2014.

AWARDS AND HONORS:

1. Compton Travel Award, Purdue University (2015)
2. NPSS Paul Phelps Continuing Education Grant, IEEE Medical Imaging Conference
   (NSS/MIC) (2014)

3. Center for Cancer Research Travel Award, Purdue University Center for Cancer Research (2014)
4. Certificate of Excellence in Interdisciplinary Research, OIGP Spring reception, Purdue University (2014)
5. Purdue Research Foundation (PRF) Grant, (PI: Dr. Keith Stantz), Purdue University (2014)
6. Ross Fellowship, Purdue University (2011)